Ultrasonic Lamb Wave Energy Transmission System for Aircraft Structural Health Monitoring Applications

Aleksander Kural

A thesis submitted to
Cardiff University
for the degree of
Doctor of Philosophy

June 2013

Summary

In this project an investigation of a wireless power transmission method utilising ultrasonic Lamb waves travelling along plates was performed. To the author's knowledge, this is the first time such a system was investigated. The primary application for this method is the supply of power to wireless structural health monitoring (SHM) sensor nodes located in remote areas of the aircraft structure. A vibration generator is placed in a location where electricity supply is readily available. Ultrasonic waves generated by this device travel through the aircraft structure to a receiver in a remote wireless sensor node. The receiver converts the mechanical vibration of the ultrasonic waves back to electricity, which is used to power the sensor node.

An experimental setup comprising a 1000 × 821 × 1.5 mm aluminium plate was designed to model an aircraft skin panel. Pairs of piezoelectric transducers were positioned along the longer edges of the plate.

The electric impedance characteristics of three transducer types were measured. A circuit simulation MATLAB code was written. An input and output power measurement system was developed. The MFC M8528-P1 transducer type was identified as providing the best performance. The use of inductors to compensate for the capacitive characteristics of transducers was shown to provide up to 170-fold power throughput increase.

The propagation of Lamb waves in the experimental plate was mapped using a scanning laser vibrometer and simulated using LISA finite difference method software.

An optimised laboratory system transmitted 17 mW of power across a distance of 54 cm while being driven by a 20 V, 224 kHz signal. This figure can be easily increased by using a higher drive voltage. This shows that the system is capable of supplying sufficient power to wireless SHM sensor nodes, which currently have a maximum power requirement of approximately 200 mW.

Declaration

This work has not previously been accepted in substance for any degree and is not concurrently submitted in candidature for any degree.

Signed _____ (candidate) Date _____

Statement 1

This thesis is being submitted in partial fulfilment of the requirements for the degree of PhD.

Signed _____ (candidate) Date _____

Statement 2

This thesis is the result of my own independent work / investigation, except where otherwise stated. Other sources are acknowledged by explicit references.

Signed _____ (candidate) Date _____

Statement 3

I hereby give consent for my thesis, if accepted, to be available for photocopying and for inter-library loan, and for the title and summary to be made available to outside organisations.

Signed _____ (candidate) Date _____

Acknowledgements

I would like to thank:

Dr. Christophe Paget of Airbus for sponsorship, supervision and providing the initial concept of the investigated system;

The team at Cardiff University School of Engineering, in particular: Professor Karen Holford, Dr. Carol Featherston and Dr. Rhys Pullin for organising the project with Airbus, arranging the funding; and for supervision, uninterrupted availability and support throughout the project; Dr. Jonathan Lees and Dr. Jack Naylon for immensely valuable advice regarding the electrical engineering aspects of the project; Dr Mark Eaton and Dr Matthew Pearson for help and advice regarding all aspects of my work on ultrasonics and the ins and outs of being a PhD student; Professor Adrian Porch for comments and advice during annual project review meetings; Paul Farrugia, Richard Rogers, Denley Slade, Len Czekaj, Des Sanford, Stephen Mead, Malcolm Seaborne for help and advice regarding laboratory work as well as for the building of samples and experimental equipment;

Dr. Peter Charlton and Mr. Kelvin Lake of Swansea Metropolitan University for agreeing to lend the laser vibrometer to Cardiff and later to use it at Swansea, as well as for assistance and advice;

Professor Wiesław Staszewski and Dr. Paweł Paćko of AGH University, Kraków, for arranging and conducting LISA software training, providing ongoing advice regarding the use of the software and allowing me to use AGH computers to perform simulations in the final stages of the project.

My friends from Cardiff, I am happy to have met you and grateful for your support during the three years away from home.

Mum and Dad, you taught me to enjoy and appreciate science, curiosity and free thinking, and loved and supported me through all the years of life and education. Without you completing this thesis would not have been possible.

List of publications

The work presented in this thesis also resulted in the following publications:

Journal publication:

Kural, A., Pullin, R., Holford, K.M., Lees, J., Naylon, J., Paget, C. and Featherston, C.A. 2013. Design and characterization of an ultrasonic lamb-wave power delivery system. *Ultrasonics, Ferroelectrics and Frequency Control, IEEE Transactions on* 60(6)

Conference publications:

Kural, A., Pullin, R., Featherston, C.A., Paget, C. and Holford, K.M. 2011. Wireless power transmission using ultrasonic guided waves. *Journal of Physics: Conference Series* 305, p. 012088.

Pullin, R., Eaton, M.J., Pearson, M.R., Featherston, C.A., Lees, J., Naylon, J., Kural, A, Simpson, D.J. and Holford, K.M. 2012. On the Development of a Damage Detection System using Macro-fibre Composite Sensors. *Journal of Physics: Conference Series* 382, p. 012049.

Kural, A., Pullin, R., Featherston, C.A., Lees, J., Naylon, J., Paget, C. and Holford, K.M. 2012. Wireless power transmission using ultrasonic guided waves - Electric circuit measurement and simulation. *Key Engineering Materials* 518, pp. 445–454.

Contents

Chapter 1. Introduction

1.1. Aim

The aim of this research is to investigate a wireless power transmission method utilising ultrasonic waves travelling along plates. The primary application for this method is the supply of power to wireless structural health monitoring (SHM) sensor nodes located in remote areas of an aircraft structure. The method can also be used in other applications in which a wireless power supply is desirable and a plate structure through which the ultrasonic waves can propagate exists. A vibration generator is placed in a location where electricity supply is readily available. Ultrasonic waves generated by this device travel through the aircraft structure to a receiver in a remote wireless sensor node. The receiver converts the mechanical vibration of the ultrasonic waves back to electricity, which is used to power the sensor node.

1.2. Motivation

The lack of suitable energy sources is currently a major obstacle in the development of aircraft SHM distributed sensor networks. Wired power supply is typically ruled out due to penalties associated with the weight increase, the added complexity of assembly and the need to perforate sealed enclosures in order to route cables. Currently available batteries are also precluded due to regulatory and safety concerns as well as the fact that they are unlikely to last the entire life span of the aircraft and will therefore require replacement. Such a replacement activity can be especially costly in the case of SHM sensors located in difficult to access internal areas of the structure.

Energy harvesting devices utilising vibration or thermal gradients occurring in the structure are considered to hold the most promise. The uninterrupted availability of sufficient amounts of energy to be harvested by such devices is, however, a source of concern. In particular, it is unlikely that any energy can be harvested while the aircraft is parked with its engines not operating.

The ultrasonic power delivery system is aimed to address the aforementioned shortcomings. It is expected to bridge the distance remaining between existing cabling and the SHM sensors without the need to install additional wires. Transmission units are to be placed near and draw electricity from power supply

lines already installed on the aircraft and send energy through the structure to receiving units adjacent to sensor nodes.

1.3. Further particulars

The following particulars follow the initial problem statement:

- The maximum power requirement of an acoustic emission damage detection SHM sensor node is currently 200 mW, although it is likely to decrease as sensor development progresses. (Other types of sensors, such as humidity or temperature, have lower power requirements.) The investigated energy transmission system is intended to deliver comparable amounts of power.
- Since aircraft structures are largely built of thin plates, the system is to use a type of ultrasonic waves specific to plates – the so-called guided plate waves or Lamb waves.
- The work is to be focussed on the power transmission through plates made of aluminium.
- The investigated transmission distance must be comparable to the size of aircraft structural elements, that is at least several tens of centimetres.
- Cardiff University School of Engineering Structural Performance Laboratory, to which the author is affiliated, has a substantial experience in the ultrasound-based structural damage detection. The author is expected to draw from this experience. In particular, he is expected to investigate the potential of using in the power transmission application the type of piezoelectric ultrasound transducers already developed for the damage detection application.

1.4. Objectives

The work presented in this dissertation was expected to achieve the following:

- Assessment of the amount of power that can be transmitted using the investigated method.
- Assessment of the distance across which the energy transmission can be realised
- Design, building and testing of a laboratory model of an energy transmission system demonstrating the investigated ultrasonic method.
- Identification of the commercially available transducer types which perform the best as transmitters and receivers of ultrasonic waves in the intended application .

- Identification of the engineering characteristics and challenges associated with the investigated ultrasonic energy transmission method.

1.5. Novelty

Methods of supplying power to embedded electronic devices using ultrasonic acoustic waves have been investigated by several research groups in the past decade (see Chapter 2.). All these systems, however, used bulk ultrasonic waves to transmit through walls from several millimetres to 15 cm thick. In this thesis a significantly different, novel design using ultrasonic Lamb waves (guided plate waves) to transmit energy along a plate and utilising MFC and Quick Pack piezoelectric patch transducers is described. Due to the low attenuation of Lamb waves and the high performance of the chosen transducer types transmission distances of approximately 50 cm with efficiency up to 64 % were demonstrated and a capability of the method to achieve longer transmission distances was indicated.

1.6. Thesis outline

This thesis is organised as follows:

Chapter 2 contains a literature review providing context for the research reported in this thesis. In Section 2.1 the currently used methods of aircraft inspection are introduced, followed by an explanation of the need for the development of SHM systems and an overview of recently investigated designs of such systems. This is followed by an overview of the power supply requirements and solutions for sensor packages used in SHM systems, indicating the case for the development of an ultrasonic energy transmission system. In Section 2.2 previous research on ultrasonic energy transmission is reported.

In Chapter 3 the characteristics of ultrasonic Lamb waves are described. The focus is on those characteristics which are important in the design of the energy transmission system. Wavelengths and mode shapes in the frequency range concerned as well as the wave generation and reception using of several types of transducers are described.

In Chapter 4 the design of the experimental setup used in the project is described. The assumptions and simplifications adopted in order to model a fragment of the intended operating environment – an aircraft structure – in the laboratory are

explained. The geometry as well as the design of the associated electric circuits is described. The choice of the investigated ranges of operational parameters, such as the frequency and voltage, is explained. Finally, a block diagram of the laboratory setup is presented and the experimental as well as computer simulation tasks carried out in relation to particular setup components are listed.

In Chapter 5 the three transducer types investigated during the project are introduced. The details of the mechanical and the electrical designs are described and the important differences between these are explained. The measurement of the transducers' electric impedance characteristics is described and its results are presented. The computer simulation tool written to predict the performance of the system's electric circuit as well the measurement system designed to experimentally measure this performance are described. Finally, the energy transmission simulation and experimental results are presented. The performance figures achieved by the three transducer types and the performance improvements achieved with the use of inductive compensation are discussed.

In Chapter 6 the behaviour of the ultrasonic Lamb wave signal in the power transmission system is described. The information presented is based on measurements carried out using a scanning laser vibrometer. The emission characteristics of the transmit transducers, the propagation of the ultrasonic signal in the aluminium plate and the operation of the receive transducers are discussed. The chapter builds on the knowledge of the electrical performance of the system presented in the preceding section. The electrical characteristics of the transmission and reception circuits are related to the corresponding characteristics of the ultrasonic signal propagating between the transducers. In this way, a complete picture of the ultrasonic power transmission is built.

In Chapter 7 modifications of the Quick Pack transducer location and orientation as well as of the plate geometry are investigated. The modifications are based on the findings in regard to the Lamb wave generation and propagations described in Chapter 6. The energy transmission performance and the laser vibrometer scans of Lamb wave propagation patterns are presented and discussed. The significant influence of small changes in the plate geometry is also reported.

In Chapter 8 the simulation of the transmission transducer operation and of the Lamb wave propagation in the experimental plate using the finite difference software package LISA is described. The simulation results are compared with previously

obtained laser vibrometer experimental measurements. The results indicate that the adopted simulation method achieves a good match with experimental results when short pulses of ultrasonic signal are investigated. In the continuous operation characteristic for the energy transmission application the simulation results are less accurate due to an inherent limitation of the mathematical method employed by the software.

In Chapter 9 the results of the project are summarised and discussed. Directions for further work are also presented.

Chapter 2. Literature review

2.1. Aircraft maintenance and structural health monitoring

2.1.1. Introduction

The aim of this section is to explain the context in which the ultrasonic energy transmission system described in this thesis is designed to operate. Concepts and methods used in aircraft maintenance are first described. Subsequently, non-destructive testing (NDT) methods used in workshop- (hangar-) based maintenance activities are introduced. This is followed by an explanation of the case for the use of structural health monitoring (SHM) systems permanently built into aircraft and by an overview of currently researched SHM technologies. A particular emphasis is placed on ultrasonic NDT and SHM methods, since the science and technology employed by these methods is applicable to the ultrasonic energy transmission system investigated in this thesis. Finally the power requirements of SHM sensors and the currently investigated energy sources are described.

2.1.2. Aircraft maintenance overview

As in the case of any type of structure, airframes deteriorate over time. Causes of this deterioration are accidental events of loading above the designed static strength limit (such as impacts, hard landings and, rarely, extremely strong gusts encountered during flight) as well as long-term processes: corrosion and fatigue (Goranson 2007). The latter two processes are also intensified by the fact that some airframes are kept in service for significantly longer periods than they were designed to (this is particularly common in the case of military aircraft). In order to ensure safety, aircraft are designed to be operated with a certain level of damage present in the structure (Goranson 2007).

The philosophies of managing short-term accidental damage and long-term deterioration are different. Accidental damage events are usually easily spotted by the aircraft or maintenance crew and can be immediately reported, assessed and, if possible, repaired. If such an event occurs on the ground, there is no need for the aircraft to remain in a flyable condition until a repair is carried out. However, in the case of events occurring during flight (including the take-off run), it is paramount that the aircraft remains able to continue flying with the damage present until it can

be brought back to the ground. Throughout the history of aviation an enormous amount of ingenuity has been put into the development of design solutions which allow aircraft to continue flying after receiving a considerable amount of damage (Wahnhill 2002). Two design methodologies are used in order to achieve this. The *fail-safe design* uses redundant systems as well as redundant load paths in the structure (Goranson 2007). If a part of the structure is damaged, the load it used to carry can be carried by an adjacent structural element. The major drawback of such a design is that it requires redundant elements, which increases the weight of the structure and negatively affects the economy of the aircraft operation. In the late 1970s the more general concept of *damage tolerance* was introduced. Damage tolerance stresses the ability of the structure as a whole to withstand the flight-related loads in the presence of damage and rests not only on redundancy, but also on the existence of other strength margins in the structure. The idea of designing durable, damage-resistant structures is old and seems very obvious. Damage tolerance differs from it by the fact that it uses large amounts of statistically processed historical data in order to allow the designer to make informed compromises between the conflicting needs of increasing the damage resistance and reducing the airframe weight (Goranson 2007). The fail-safe and damage tolerance design philosophies have proven to be very successful in preventing fatal accidents in the face of sometimes very heavy damage. The 2010, safe landing of a Qantas Airways Airbus A38,0 after an uncontained inboard engine failure destroyed multiple systems and structural elements in the wing, is only one, highly publicised example of this success (Kinsley-Jones 2012).

The management of long-term deterioration effects (fatigue and corrosion) also rests on the fail-safe and damage tolerance philosophies. The condition of the aircraft with respect to these damage mechanisms is maintained through regularly performed checks. The so-called “A-checks” last up to 24 hours and are typically performed every two months. The more thorough “B-“, “C-“ and “D-checks” last up to several weeks and are typically performed every six months to five years (Pfeiffer 2007). For the duration of these inspections the aircraft is taken out of service, which translates into a significant cost on the part of the operator. Thus, aircraft manufacturers strive to increase the required intervals between these maintenance checks. Since fatigue and corrosion are processes which progress continuously, the aircraft structure is expected to develop a certain level of undetected damage during the intervals

between inspections. Its safety in the presence of such undetected damage is maintained through careful fail-safe and damage-tolerant design of the aircraft structure.

In the case of the fatigue cracking, the balance between safety and maintenance economy rests on the knowledge of the following factors; the maximum allowable crack length, the crack growth speed, the crack detection threshold and the detection probability (Goranson 2007). The maximum allowable crack length is the length at which the structure can still be safely operated. Safe operation means not only a non-occurrence of a catastrophic failure, but also of events such as a fuel leakage or excessive air leakage from the pressurised fuselage. The estimation of the allowable crack length is further complicated by the occurrence of the multiple-site damage. A typical example of such damage is a situation in which otherwise safely short cracks propagate simultaneously from multiple adjacent fasteners (rivets) and, at some point, join, to immediately create a long crack causing structural failure. Crack growth speeds are determined with the use of theoretical and experimental fracture mechanics methods as well as through the analysis of large amounts data collected from in-service aircraft.

Crack detection thresholds and detection probabilities are used to define the effectiveness of inspection methods. Detection thresholds are typically defined as the minimum length at which a crack can be detected by the chosen inspection method. The probability of detection is composed of three independent probabilities: the probability of detection of a crack when the area containing this crack is inspected, the probability that the area containing the crack will be inspected during a maintenance check, and the probability that the aircraft containing damage will be inspected as part of an inspection programme. The first of these probabilities is a characteristic of the chosen inspection method. The latter two are a function of the inspection programme planning. For the purpose of this introductory text it is sufficient to mention that all the aforementioned probabilities are estimated based on vast amounts of historical data and that the currently used inspection programmes are a result of many decades of data collection and analysis. The ultimate goal of such an inspection programme development is to ensure that all cracks are detected before they reach their maximum allowable lengths while minimising the frequency, duration and cost of the inspections.

Of the two long-term deterioration effects, corrosion is less common. A significant improvement in the effectiveness of protective surface coatings has taken place since the 1970s, resulting in a decrease of corrosion occurrences. Many operators cover areas in which corrosion is likely to occur as part of their existing inspection schedules. In addition, aircraft manufacturers issue further recommendations regarding areas which are known as being susceptible to corrosion and which should be inspected (Goranson 2007).

The inspection programmes in place in the aviation industry have proved to be extremely successful. According to the Boeing "Statistical Summary of Commercial Jet Airplane Accidents" reports (Boeing 2000, 2006, 2011) in the period between 1991 and 2000 there were six commercial jet accidents caused by a system or component failure out of 391 total (1.5%); five in the 1997-2006 period (1.3% of the total); and one in the 2002-2011 period (0.2% total). On the other hand, even those cases of structural or mechanical problems which do not lead to a disaster can receive substantial press coverage. A recent example of such a case is the unexpected aftermath of the aforementioned 2010 Qantas A380 accident (Toh 2010). The damage caused by parts of the disintegrated engine prompted a thorough inspection of the wing structure. In addition to the damage caused by the engine malfunction, multiple fatigue cracks in the wing ribs were discovered. This led to further inspections on other aircraft of the same type, revealing a widespread occurrence of similar cracks. The cracking was eventually attributed to accelerated fatigue caused by an incorrect rib material choice. Although Airbus stated that the cracks posed no safety risk and would have been discovered later during scheduled inspections, the event created much negative publicity for the manufacturer (Toh 2012). In addition, the 2010 accident highlighted another risk factor whose significance is increasing in recent aircraft design. As computer-aided design and stress simulation tools are becoming more sophisticated, engineers using them trust the simulated results more and are inclined to accept less conservative estimates. It is believed that this in turn produces designs which are more sensitive to design and manufacturing errors.

2.1.3. NDT methods used in workshop inspections of aircraft

Three non-destructive testing (NDT) techniques are primarily used during maintenance inspections of aircraft structures. All three allow inspection of small areas of the structure at any given time. Thus, in order to inspect larger fragments of

the structure, scanning is required. This scanning, even on large aircraft, is carried out by the inspection worker who gradually moves (together with his/her inspection equipment, if applicable) over the designated inspection region. As inspection requires much attention to detail, such work is time- and labour-intensive. Thus, the labour cost forms a significant portion of the overall inspection cost (Cawley 2001).

Despite the continuing development of machine-based techniques, visual inspection by human eye remains the most widespread technique (Goranson 2007). This is due to the fact that it offers a sufficiently low detection threshold and a sufficiently high detection probability while not requiring an investment in specialist equipment. In addition, a relatively large area can be seen and inspected by a single operator. In some cases, the surface crack detection can be aided by the use of a dye penetrant, which colours the cracks and makes them more visible. It should be noted that visual inspection is able to detect only defects which extend to the surface of the inspected part. Thus, it is most suitable for the detection of fatigue cracking and corrosion in metallic structural parts.

Eddy current testing is a highly popular NDT method used on metallic aircraft structure parts. The detector contains a coil conducting an alternating current. The resulting alternating magnetic field induces eddy currents near the surface of the tested part. Cracks in the part modify the flow paths of the eddy currents. These changes can than be detected and visualised by the testing equipment. While offering a higher sensitivity in the detection of small cracks than the visual inspection, the eddy current detector covers only a small area and requires an operator to move it over the inspection area. Thus, eddy current testing is more commonly used for detailed inspection of smaller, pre-selected areas (Goranson 2007).

Ultrasonic testing is suitable for both metallic and composite structures. The operating principle is the same as in ultrasound scanners used in medicine. A hand-held device, coupled to the tested part by gel or water, emits bulk ultrasonic waves into the tested structure. The signal is reflected by internal features of the structure and subsequently received by the device, processed and presented on a display. Features of the structure, including defects, can be identified on the displayed image. Again, the instantaneous inspection area is small and testing of larger areas requires the operator to move the detector by hand.

In addition to these popular methods, several other NDT techniques exist. Thermography uses infrared lamps to heat the inspected component, which is

subsequently photographed using an infrared camera. Areas of the surface under which defects are present may show as having a different temperature to their surroundings (Avdelidis 2003). Shearography is a photographic method in which two images of the object surface are taken. Before the second image is made, the object is deformed e.g. by applying mechanical stress or heat (thermal shearography). Superimposing the two images reveals areas in which deformation has occurred. Areas with defects may deform differently to their surroundings allowing defect detection (Hung 1982).

Other, less common NDT techniques include TV holography, audible sound-based imaging and alternating current field measurement (ACFM) (Cawley 2001). TV holography is also referred to as electronic speckle pattern interferometry (Lokberg 1988). In this method images created by two laser beams, one reflected from a measured object's surface and one direct, are superimposed onto each other in order to produce interference pattern. The resulting pattern is used to calculate the deformation of the measured surface. In NDT application, heat or sound are applied to the sample in order to generate deformation. Locations of damage are inferred from the deformation shape, similarly to shearography. Low-frequency acoustic methods comprise the coin tap test (in which the tested structure is tapped by the operator with the use of a coin; changes in sound heard by the operator indicate damaged areas), the mechanical impedance analysis (in which a vibrating crystal is pressed against the tested structure; depending of the condition, and thus stiffness, of the structure the vibration of the crystal is changed to a varying degree), the membrane resonance method (in which the structure is vibrated; changes in the vibration response indicate damage), and imaging methods analogous to ultrasonics, but using sound friequencies in the audible range (Cawley 1990). ACFM uses alternating magnetic field to induce alternating current in the tested metallic element. Unlike the eddy current method, it is used for thick specimens (Dover 1991).

Since the low speed of handheld scanning is a major obstacle to the widespread use of eddy-current and ultrasonic testing, one could expect that robotic scanning would have replaced the hand-held method. This has indeed been the case in the post-manufacture inspection of newly made parts. Gantry-mounted ultrasonic scanners are especially popular. Surprisingly, robotic scanners for the inspection of in-service aircraft have not yet gained widespread use and most inspections are performed using hand-held NDT devices. Several companies and institutions are

working on the development of robotic inspection systems for in-service aircraft. A system under development by a partnership of Triton Systems Inc., BAE Systems and General Electric Inspection Technologies is to utilise a crawler robot, carrying a variety of NDT scanners in the inspection of the aircraft (Bogue 2010). Another crawler robot design uses an array of suction cups to travel on the aircraft surface while performing NDT inspection (Shang 2007). Devices using more conventional multiple-degree-of-freedom robotic arms are considered to be more suitable for the inspection of smaller objects, particularly during manufacturing (Mineo 2012).

2.1.4. Structural health monitoring in aircraft

The previously listed shortcomings of periodic non-destructive inspection methods define the case for the development of aircraft structural health monitoring (SHM) systems. Such systems comprise multiple sensors permanently built into the aircraft structure and are able to automatically inspect this structure either in real time or at significantly reduced intervals. The sensors are connected by a data collection network also comprising data processing and storage units (Speckmann 2007). The use of a reliable SHM system could provide the following benefits (Pfeiffer 2007):

- As the structure's condition (including the growth of fatigue cracks or corrosion) would be continuously monitored, the intervals between periodic off-line inspections and repairs could be adjusted according to the actual aircraft condition. Ideally these intervals could be increased, thus reducing the cost of the maintenance programme.
- As the SHM sensors would be built into the structure, they would be able to monitor the condition of areas which are difficult to access and therefore designed for less-frequent inspection. This could allow the detection of unforeseen damage, such as the fatigue cracking of the ribs in the Airbus A380 case described above. This would increase the safety of aircraft operation.
- Finally, the availability of large sets of automatically collected inspection data could be used to improve future aircraft designs.

SHM has attracted growing interest from the engineering community since the end of the 1990s. Research into the underlying science as well as the development of prototype systems has been carried out by multiple academic institutions, firms and consortia. In the UK, aircraft structural monitoring research is carried out by

universities including Cardiff (ultrasonics, energy harvesting), Cranfield (fibre optic sensors, energy harvesting), Imperial College London (ultrasonics, signal processing), Bristol (ultrasonics), Sheffield (ultrasonics, signal processing), Southampton (energy harvesting) and Strathclyde (ultrasonics); institutions including TWI, National Physical Laboratory, the MOD and businesses including BAE Systems, Airbus, Physical Acoustics and a host of smaller companies. A number of industry-academia projects have been funded by the Technology Strategy Board. WITNESSS (WIreless Technologies for Novel Enhancement of Systems and Structures Serviceability), operating between 2009 and 2011, focussed on the development of wireless communication between sensors, a key component of planned SHM networks (WITNESSS n.d.). SHEMS (Lightweight Structural HEalth Monitoring System), including, among others, Cardiff University, operated between 2009 and 2012 and developed science and prototype devices for an SHM system using a wireless network of ultrasonic structural damage sensors (www.shemsproject.co.uk). Similar levels of interest can be observed worldwide. Despite these efforts, to the author's knowledge, SHM systems have not yet become standard on any aircraft type, although development systems have been tested in flight (Microstrain 2013, Speckmann 2007).

Such a state of affairs can be attributed to the fact that a usable SHM system must comprise several subsystems, each presenting its own set of design challenges:

- Damage detection sensors. Challenges: increasing the distance from which damage can be detected, achieving a high probability of detection while avoiding false alarms, reducing sensitivity to environmental factors distorting the readings, achieving the ability to work with various structural configurations, etc.
- Data collection network. Challenge: avoiding using wired connections due to incurred mass increase, difficulty of routing cables to a high number of sensors distributed over large areas of the aircraft. Hence: the need to develop secure wireless data transmission methods which will work through the aircraft structure and will not interfere with avionics systems.
- Power supply. Challenge: avoiding using wired connections for reasons described above. Hence: develop local power sources which will be integrated with individual sensors.

In the development of damage detection sensors, two methods receive the most attention. Optical fibres with Bragg gratings allow the measurement of structural

deformation over large distances (of the order of metres) and are particularly applicable to composites. The fibres can be embedded in the composite part during its manufacture and do not affect the strength of the part due to their small diameter of approximately 0.25 mm, which is comparable to the diameter of typical carbon fibre yarn (0.1 – 0.6 mm) (Hexcel 2013). The system can then be interrogated with light pulses. Axial strain or bending of the fibre changes the characteristics of the light pulse reflected from gratings made on the fibre wall, allowing the measurement of deformation. It has been demonstrated that such fibre optic sensors are capable of detecting deformation associated both with normal usage of the structure as well as with damage (Kahandawa 2012).

The second damage detection method considered for SHM is the use of ultrasound. These methods also provided the basic technology from which the ultrasonic power transmission system described in this thesis was developed. For these reasons the ultrasonic SHM methods will be described in a greater detail in the next section.

2.1.5. Ultrasonic SHM methods

In the ultrasonic SHM application two approaches are used – an active and a passive one. The active approach, often referred to as acousto-ultrasonics, is similar in principle to ultrasonic inspection methods used in production and maintenance (Finlayson 2001). The SHM system actively emits an ultrasonic signal which is used to interrogate the structure. After passing through or being reflected from structural features and flaws, the signal is the received by the system and analysed. A typical active SHM system consists of a set of transducers distributed over the region which is to be monitored. Multiple transducers can be used to emit and receive ultrasonic signals. The use of a limited number of fixed transducers to localise damage in a large area poses significant challenges in the development of signal processing methods. Signal processing and sensor position optimisation to maximise the probability of flaw detection while limiting the required number of sensors are currently one of the most prominent research directions in the field of ultrasonic SHM.

Active ultrasonic SHM systems differ from handheld or gantry-mounted ultrasonic inspection scanners used for aircraft component inspection in the type of ultrasonic waves they use. Inspection scanners image through the thickness of the

plate forming a part of the aircraft structure. The scanner sends the ultrasonic signal in a direction approximately perpendicular to the surface and subsequently receives the signal reflected from flaws or the opposite surface of the plate. It is then moved along the plate surface in order to scan a larger area. This method requires the use of the so-called bulk acoustic waves (Krautkramer 1983). This is because the wave propagating through the thickness of the material is not bound, or guided by any surfaces parallel to the direction of propagation (Figure 2.1 (a)).

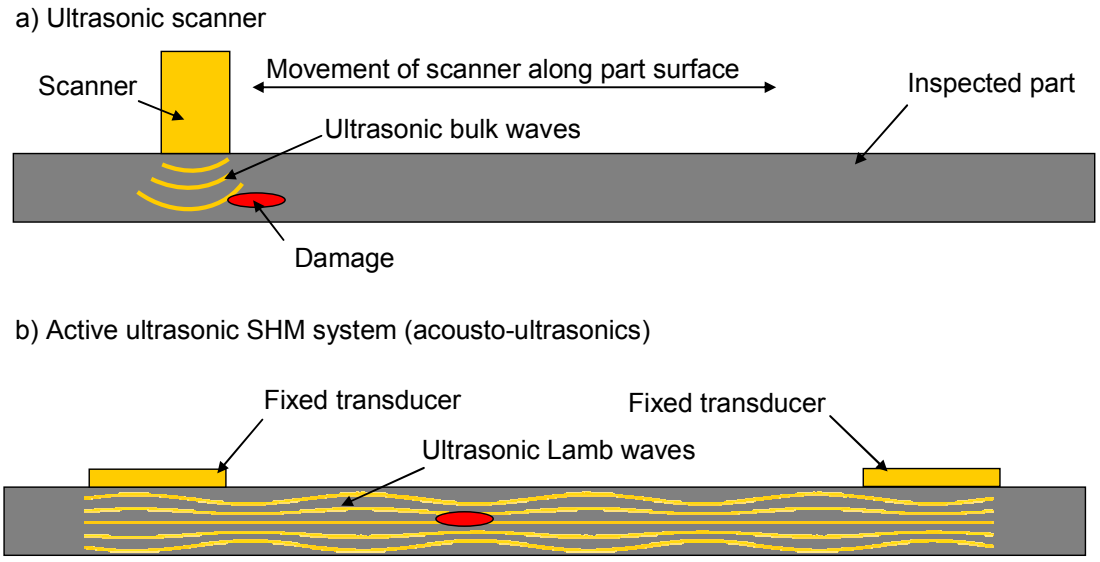

Figure 2.1. Illustration of principles of operation of a) workshop inspection ultrasonic scanner using bulk acoustic waves b) active (acousto-ultrasonic) structural health monitoring (SHM) system installed on a plate and using acoustic guided plate waves (Lamb waves). Reflections or changes of signal due to interaction with damage not shown for clarity.

There are two types of bulk waves. Longitudinal bulk waves consist of variations of density and pressure propagating through the medium (Figure 2.2 (a)). (Longitudinal waves are commonly known to transmit audible sound in air, liquids and solids.) Shear bulk waves consist of shear deformations travelling through the medium (Figure 2.2 (b)). The velocity of bulk waves (the speed of sound) depends on the material properties of the medium in which they propagate, but does not depend on the shape or dimensions of the part (Krautkramer 1983).

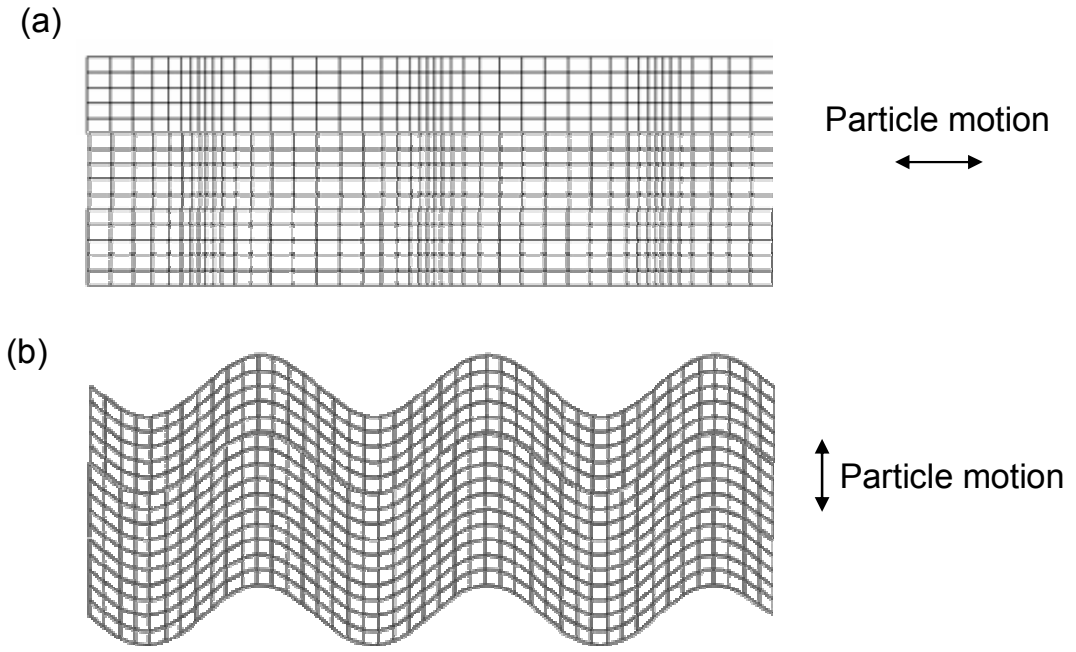

Figure 2.2. Illustration of bulk acoustic waves: (a) longitudinal, (b) shear. Image source: Hoskins (2012).

In an SHM system the transducers are fixed to the structure. Therefore scanning by means of transducer movement cannot be realised. Instead, a number of transducers distributed over an area can then receive signals reflected or altered by damage present in the material. Processing of the signals received by several transducers allows location of the damage by triangulation (Finlayson 2001). In some designs the transducers are capable of steering the signal beam in desired directions within the plane of the plate, acting in a way similar to radar (Giurgiutiu 2004). In aviation structure monitoring applications, since such structures are typically built of plates, SHM systems use the so-called ultrasonic Lamb waves (also referred to as ultrasonic (or acoustic) guided plate waves). Lamb waves propagate along thin plates bound by the plate surfaces (Figure 2.1. (b)). Since Lamb waves are used in the ultrasonic power transmission system described in this work, their characteristics are presented in greater detail in Chapter 3.

The passive ultrasonic SHM method is referred to as acoustic emission (AE). The acoustic emission phenomenon entails a rapid release of mechanical energy within the material. Such a release of energy occurs during the advancement of a fatigue crack. The energy then propagates through the material in the form of acoustic waves. An AE SHM system detects these signals with the use of transducers and processes the acquired waveforms in order to locate the sources (Finlayson 2001). In

plate structures these signals travel in the form of Lamb waves (Figure 2.3) (Eaton 2012). The advantage of this method comes from the fact that the signals are generated at damage locations. While in an active SHM system the data processing system must recognise the signal variations corresponding to damage in a flood of direct and/or reflected ultrasound that have been actively injected into the tested material. In a passive system the only source of signals of interest is the damage. Still, environmental noise, signal reflections and the coexistence of several Lamb wave modes may obscure the damage-related signals, but the identification task is simplified in comparison to the active system. A disadvantage of AE is that signals are generated only at moments of crack growth, therefore the SHM system must be constantly switched on and listening in order to be able to locate the damage. The structure must also be subjected to operating loads in order to cause fatigue damage to occur, which predestines the AE method for used on structures under operation or testing. At the same time, the same characteristic allows the velocity of the crack propagation to be judged by monitoring the frequency at which the signals are generated, which is highly advantageous. Another difficulty, in comparison to active systems, is that signals generated by crack growth have limited amplitude and therefore can be more easily obscured by noise. Nevertheless, AE has proved to be a valuable SHM method and has been chosen for use in various SHM systems. An example of this is the SHeMS system under development by Cardiff University and partners.

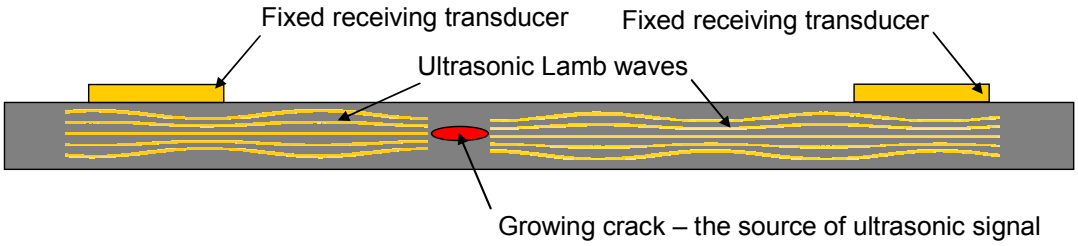

Figure 2.3. Illustration of the principle of the acoustic emission (passive ultrasonic) SHM method as applied to a plate structure.

2.1.6. Power sources for wireless SHM sensors

Several power sources are considered for the distributed sensors used in SHM systems. A wired power supply is the most conservative choice. It is a mature technology and offers reliability, practically unlimited power throughput (within the

small electronics requirements range) and a possibility to transmit data as well. Unfortunately, in the case of an SHM system, the typical disadvantages of wires become prohibitive. Since SHM systems are to be composed of a large number of sensors distributed over large areas of the aircraft structure, the mass increase and the difficulty of routing associated with the required amount of cabling is unacceptable.

Non-rechargeable batteries are the second mature technology considered for SHM. However, since SHM sensors are to be placed in areas of the aircraft which are difficult to access or not accessible, it must be assumed that it will be impossible to replace those batteries during the lifetime of the aircraft. Thus, the size of batteries needed to supply power to the sensors during their 20 – 30-year planned lifetime (or even longer, especially in the case of military aircraft) would be prohibitive. In addition, current regulations do not allow placing batteries inside the aircraft structure, in particular inside of integral wing fuel tanks (Paget 2011).

As a way to overcome the disadvantages described above, energy harvesting methods are considered as a power source for SHM systems (Greaves 2008). Energy harvesting is the generic name given to several methods aiming to collect energy from ambient sources available locally in the surroundings of the device requiring power. In this sense, solar cells are the most common form of energy harvesting devices. Since SHM sensors are to be placed inside the aircraft structure without access to sunlight this energy source cannot be used.

Energy harvesting from structural vibration is currently considered to have considerable potential as the power source for SHM sensors. In this method the vibration of the aircraft structure due to engine operation and aerodynamic loads is used to drive an electricity generator. These devices typically use a proof mass suspended on a spring or cantilever which vibrates at its resonance frequency driven by the structural vibration. Maximum efficiency is achieved when the driving vibration has the same frequency as the device's resonance frequency. This makes the practical application significantly more difficult as structural vibrations are often broadband or have frequencies which change over time (Roundy 2002). The vibration to electricity conversion in such devices is realised using either the electromagnetic or the piezoelectric principle. Several models of vibration energy harvesters are available commercially (Table 2.1). A performance comparison is difficult as each manufacturer quotes power output measured at different source vibration amplitude (acceleration) and each device is also designed for a different

resonance frequency. The relation between the power output and the device mass is, in general, not favourable (see Table 2.1). Another disadvantage associated with vibration energy harvesting devices is that they can only supply power when the aircraft structure is vibrating, i.e. either on the ground with the engines operating or in flight.

Table 2.1. Examples of commercially available vibration energy harvesting devices

Device maker / name (Reference)	**Type**	**Device mass [g]**	**Power output [mW]**	**Maximum acceleration of vibration at which the specified power output is achieved [m/s^2]**
Advanced Cerametrics Harvestor (Advanced Cerametrics n.d.)	Piezo	several grammes	0.2	30
Mide Volture (Mide n.d.)	Piezo	85	0.7	10
Ferro Solutions (Ferro Solutions n.d.)	Electro-magnetic	430	5.2	1
Perpetuum VMG (Perpetuum n.d.)	Electro-magnetic	650	10	no data

The second energy harvesting method considered for aviation SHM use is thermal energy harvesting. This method draws energy from the temperature differential between the interior (for example fuel in the fuel tank) and the exterior of the aircraft skin. During a typical flight this temperature differential varies within the range of approximately ± 15 °C. The material typically used to build thermoelectric cells in such devices is bismuth telluride. At this temperature differential a bismuth telluride device can generate approximately 0.34 mW/mm^2 (Arnold 2012). A thermoelectric cell with the same footprint as the Mide Volture vibration harvester (92 mm x 45 mm = 4140 mm^2) can thus produce 1.4 W of power at a 15 °C temperature differential, which is 2000 times more than the 0.7 mW quoted for the Mide harvester. Regardless of the differences between the test conditions at which these values were specified, this example illustrates the potential of the thermoelectric method to perform in an aviation application. Unfortunately large

temperature gradients exist only during the climb, the initial phase of the cruise and the descent of the aircraft, although work has been done to extend the duration over which this gradient exists (Samson 2011). Thus, a thermoelectric harvester is not able to supply power continuously. In this respect the thermal method is similar to the vibration harvesting method.

The level and variability of the power output over time are the major shortcomings of the vibration and thermal energy harvesting methods. This makes the use of some sort of energy storage unavoidable, which in turn may not be acceptable due to the aforementioned safety and regulatory issues (Paget 2011).

The fact that no currently available wireless power supply method is sufficient to power an SHM sensor node suggests the design of the power supply system as combining several different sources and an energy storage unit. The expectation with such a system is that the various sources will provide electricity during different phases of flight and thus complement each other. So far, however, few reports of practical applications of energy harvesting-powered sensor units have been published. Working examples are large devices used on heavily vibrating industrial motors, rail vehicles and helicopter gearboxes (Perpetuum n.d.).

2.2. Previous work on ultrasonic energy transmission

2.2.1. Introduction

The use of the ultrasonic Lamb waves to transmit energy through an aircraft structure, as described in this thesis, is novel. The use of various types of acoustic waves to transmit energy in other applications, however, is not a new concept. More specifically, the "electric to acoustic to electric" energy conversion path has been used in many types of devices. In this section previous work on the ultrasonic energy transmission is summarised.

2.2.2. Piezoelectric transformers and other bulk acoustic wave (BAW) devices

One of the the earliest applications of continuous acoustic energy transmission is the piezoelectric transformer. The first design was proposed by Rosen in the 1950s (Rosen 1958). A typical piezoelectric transformer consists of two stacked piezoelectric transducers. The transducers are electrically insulated from each other, but remain bonded mechanically in order to allow the transfer of strain and stress. When operated, vibration generated in the primary transducer by the supplied AC

electric signal propagates to the secondary transducer which converts it back to AC electricity.

In the Rosen transformer (Figure 2.4) the input voltage V_{in} generates an electric field between the input electrodes. The magnitude of this electric field is equal to:

$$E_{in} = \frac{V_{in}}{h} \quad (1)$$

where h is the thickness of the piezoelectric bar from which the transformer is built. As the piezoelectric material in the input section is poled along its thickness, this field causes a deformation of the input transducer due to the reverse piezoelectric effect. The deformation occurs both in the thickness direction, via the d_{33} piezoelectric constant, and in the length (dimension l_{in}) direction via the d_{31} piezoelectric constant. (The d_{31}/d_{33} ratio is close, but not equal to the material's Poisson's ratio. E.g., for PZT materials d_{31}/d_{33} is in the range 0.37 – 0.4, while the Poisson's ratio is 0.35 (Sinocera 2013)).

In order to operate efficiently the transformer must be driven at a frequency which is near the longitudinal mechanical resonance frequency of the piezoelectric bar. Under such condition the bar begins to oscillate (expand and contract) along its length. Thus, the oscillating lengthwise strain is transferred to the output section of the transformer.

As the output section is poled along its length, the lengthwise strain generates an electric field between the output electrodes due to the direct piezoelectric effect. In turn, this field causes a voltage to appear between the electrodes. This voltage is equal to:

$$V_{out} = E_{out} \cdot l_{out} \quad (2)$$

where E_{out} is the electric field generated in the output section and l_{out} is the length of this section.

The derivation of the relation between E_{in} and E_{out} and, subsequently, the transformer ratio is not straightforward as it must describe both the elastic and the electrical oscillation within the transformer. A dissertation by Lin (1997) contains a

step-by-step derivation of formulas describing the piezoelectric transformer characteristics with the use of equivalent electrical circuit models.

Without a detailed derivation it can be incurred, however, from the comparison of Equations (1) and (2) that the transformer ratio is proportional to the ratio of the length and the thickness of transformer:

$$\frac{V_{out}}{V_{in}} \propto \frac{l_{out}}{h} \qquad (3)$$

This conclusion is also mentioned in literature (Lin 2001).

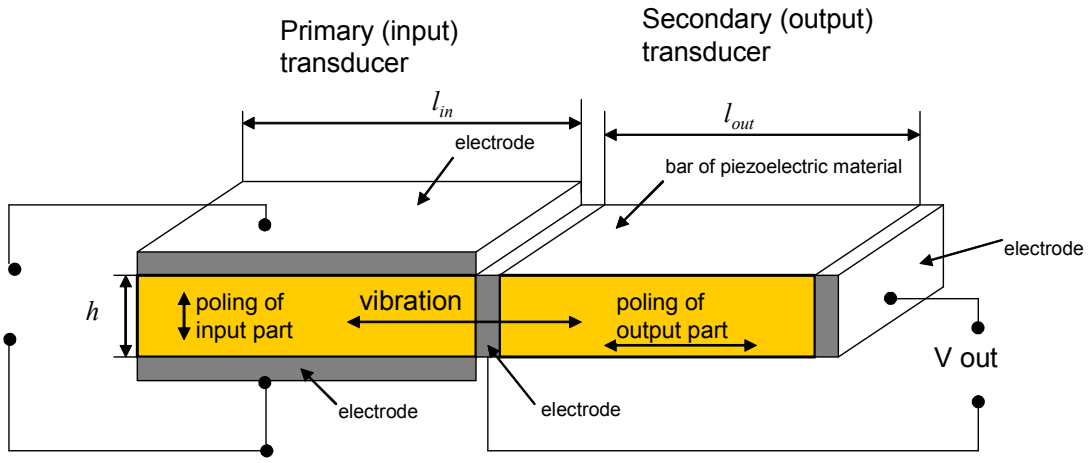

Figure 2.4. Rosen piezoelectric transformer.

Other configurations of piezoelectric transformers were proposed by the original inventor Rosen (1958) and, subsequently, by others (Lin 2001). Piezoelectric transformers are widely used, particularly as high-gain transformers and electronic ballasts in fluorescent light bulbs. The advantages of piezoelectric transformers, in comparison to traditional electromagnetic coil devices, include small size, easy to realise high gains and easy integration with small printed circuit boards. Their area of application is currently limited to low power devices, as in larger power applications their efficiency is lower than that of inductive transformers and the cost is higher (Lin 1997). The frequencies at which piezoelectric transformers operate vary with application, typically in the kHz and the MHz range (Lin 1997, Lin 2001).

Since the piezoelectric elements in the transformer have narrow resonance frequency ranges, the piezoelectric transformer also acts as a band-pass filter, working efficiently only around its resonant frequency. When frequency filtering is

the primary function of the device, it is referred to as a bulk acoustic wave (BAW) filter. Another type of a BAW device is the delay line. In some electronics applications it is necessary to delay a radio frequency (RF) signal by a set interval. The propagation velocity of bulk acoustic waves is several orders of magnitude lower than the propagation velocity of electromagnetic waves. Thus, a sufficient signal delay can be achieved by passing an acoustic signal through a block of material only a few centimetres long. Achieving a similar delay using an electromagnetic waveguide would require a device many metres or kilometres long (Weigel 2002). BAW devices are also commonly used as oscillators for time and frequency reference. This application, however, does not entail energy transmission through a substrate between a pair of transmission and reception transducers.

2.2.3. Surface acoustic wave (SAW) devices

The surface acoustic wave (SAW) is also referred to as the Rayleigh wave (Weigel 2002). It was first described by Lord Rayleigh in the 1885 (Raleigh 1885). Figure 2.5 illustrates the deformation of a medium through which a SAW is propagating. The wave is guided along the surface of the medium. The amplitude of the deformation is the largest at the surface and decreases rapidly with depth. Particles in the medium undergo a circular motion during the passage of the wave. The velocity of the wave is independent of the frequency and of the shape of the object through which it propagates, but depends on the material properties (e.g. the Rayleigh wave velocity in steel is approximately 2900 m/s) (Viktorov 1967).

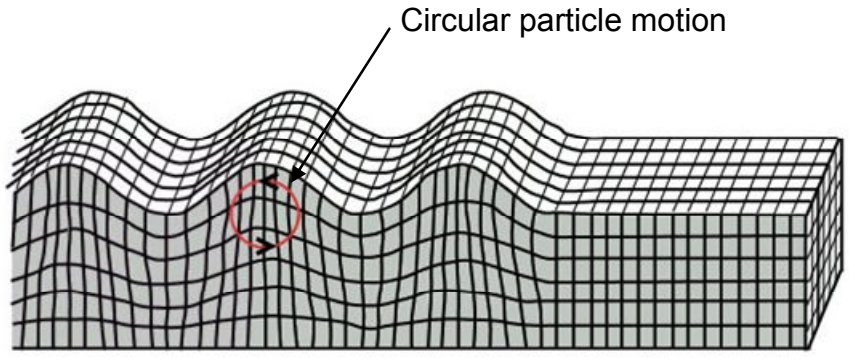

Figure 2.5. Rayleigh wave (surface acoustic wave, SAW). Image source: USGS (n.d.).

In the 1960s the potential of using SAWs in electronic devices was discovered (Weigel 2002). In comparison to BAWs, SAWs offer the advantage of being accessible for transduction over a large surface area of the object through which they

propagate. They can, therefore, be manipulated more precisely than bulk waves. The generation and reception of SAWs is performed with the use of interdigitated (interleaved) electrodes generating an electric field interacting with the piezoelectric substrate material, as shown in Figure 2.6. The spacing and overlap between the electrodes can be designed in order to determine the characteristics of the generated surface acoustic wave. The interdigitated electrode pattern is easily realisable using lithography techniques common in electronic component manufacture. This contributes to the popularity of SAW devices in electronics applications (Weigel 2002).

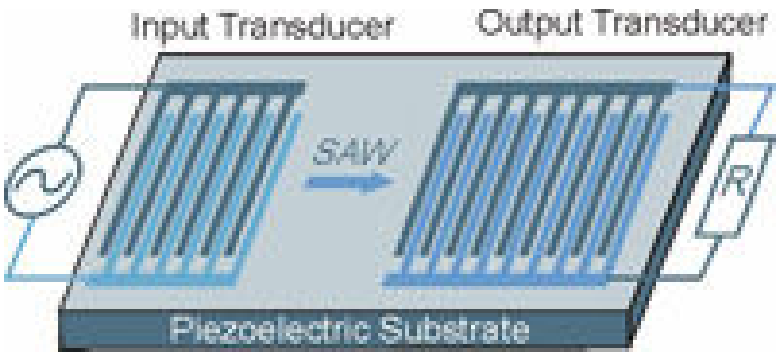

Figure 2.6. Schematic view of a typical SAW (surface acoustic wave) device. Interdigitated electrode transducers are visible. The input electrode set (left) is driven by AC voltage and generates SAWs on the surface of the substrate. These in turn generate voltage in the output electrode set. Image source: EVG (n.d.).

Filters are the most common type of SAW devices. The electrode design as well as the dimensions of the substrate can be adjusted to achieve the desired resonance characteristics. SAW filters are widely used in mobile radio devices (including mobile phones) and televisions. They typically operate in the range between 30 MHz and 3 GHz (Weigel 2002). Other applications of SAW devices include delay lines, transformers, oscillators and sensors.

2.2.4. Through-thickness transmission in mechanical engineering applications

While using the ultrasonic vibration as the means of energy transmission, BAW and SAW devices do not aim to transport energy over large distances in a structure. Reports of research into longer-distance ultrasonic energy transmission designs were

first published recently. They include applications in mechanical and medical engineering fields. This work is summarised below.

In the mechanical engineering field several academic and industrial research groups have investigated ultrasonic energy and data transmission through the thickness of walls in various types of enclosures (Kluge 2008, Neasham 2010). The application areas have included power delivery and data exchange with sensors located inside hydraulic pressure accumulators, chemical storage vessels, and behind the walls of ships and spacecraft. In all these applications the main motivation of the research was the desire to avoid the perforation of the wall usually needed in order to route an electrical feed-through. Traditional feed-throughs carry the risk of leakage and decrease the effectiveness of thermal and electrical insulation (Bao 2008). An ultrasonic feed-through allows the transmission of power and data through the wall material and preserves the integrity of the enclosure. Through-thickness energy transmission systems use ultrasonic bulk waves as the transmission medium. Table 2.2 contains a summary of the through-thickness ultrasonic power transmission research results published to date.

Table 2.2. Overview of mechanical engineering through-thickness ultrasonic energy transmission research

Group	Reference	Transducer type	Medium	Dist-ance [mm]	Frequen-cy [kHz]	Trans-mitted power	Effi-ciency [%]	Drive voltage [Vpp]
Renssealer Polytechnic, UC San Diego, Lockheed Martin	Shoudy 2007	Piezo crystal ∅ 25.4 mm	Steel	57 to 152	1087	250 mW	n/d	40
	Lawry 2010	Piezo crystal ∅ 57 mm	Steel	9.5	946.5	81 W	55	n/d
NASA JPL	Bao 2008	Piezo crystal ∅50 ×~20mm	Titanium	5	24.5	1 kW	88	1800
EADS Innovation Works Munich	Ngo 2008, Kluge 2008	Piezo crystal ~∅ 8 mm	Alumi-nium	7	3000	30 mW	80	20
Defence Science and Technology Organization, Australia	Moss 2010	Piezo crystal ∅10 ×0.5 mm	Alumi-nium	1.6	4200	n/d	34	n/d
Newcastle University Extreme Engineering group	Graham 2011, Neasham 2010	Electro-magnetic	Steel	80	1000			

Shoudy *et al.* (2007) of Renssealer Polytechnic, UC San Diego and Lockheed Martin describe a system for power and data transmission through a steel wall 57 mm to 152 mm-thick. The intended application is to deliver power and exchange data with sensors placed inside pressure vessels. The system uses 25.4 mm-diameter round piezoelectric transducers. The transducers have the design resonance frequency of 1 MHz. The authors also designed and built dedicated electronic circuits for the system components meant to be placed outside and inside the enclosure. The circuits performed the tasks of drive AC voltage generation, received AC voltage rectification and storage as well as bi-directional data transmission. The

system transmitted approximately 270 mW of continuous power through a 57 mm wall while being driven with a 40 Vpp signal. The authors discovered that the power throughput is highly sensitive to the operating frequency. The 270 mW maximum is achieved at 1.087 MHz. When the frequency is changed to 1.021 MHz the power throughput decreases to approximately 20 mW. The correct matching of the reception circuit resistance to the resistance of the piezoelectric transducer is also discussed. The system is also able to transmit data with the speed of 55 kbps. Results for the 152 mm-thick wall are not presented in detail.

Lawry *et al.* (2010), also of Renssealer Polytechnic, describe in detail the theory of matching the acoustic and electrical impedances of the transmission and reception circuits. They present experimental results for various wall thicknesses. For optimally matched set-ups efficiencies between 5 and 37 % were achieved in transmission through a 57 mm-thick wall, depending on the transducer configuration and the wall sample shape. In a 9 mm-thick wall, efficiencies between 37 and 55 % were achieved and a maximum of 81 W of power was transmitted. The drive voltage amplitude was not reported.

Bao *et al.* (2008) of the NASA Jet Propulsion Laboratory describe a system transmitting 1 kW of power across a 5 mm-thick titanium wall with 88 % efficiency. The unusually large power throughput is achieved by using relatively large piezoelectric transducers (50 mm diameter, 20 mm thick) and a 1800 Vpp drive voltage. The operating frequency was 24.5 kHz. The drive circuit was built from a function generator with two amplifiers and the reception circuit comprises only a set of light bulbs. No consideration was given to the matching of the transducers and the circuits. While not focussing on most design challenges associated with ultrasonic power transmission systems, the reported experiment illustrates how the power throughput can be increased enormously by simply increasing the drive voltage to over 1000 V. It should be noted that this principle is applicable also to the Lamb wave system described in this thesis. The authors also comment on the challenge of measuring the AC power delivered to the transmission piezoelectric transducer. The transducer's highly capacitive characteristics result in a nearly-90° voltage-current shift in the drive circuit, which makes the power determination very sensitive to small inaccuracies in the voltage-current shift measurement. The same problem was encountered by the author of this thesis and took a considerable time to overcome.

Publications from Kluge (2008) and Ngo (2008), of EADS Innovation Works Munich and co-operating universities, present designs of power- and data-transmitting systems aimed at use with sensors located in pressure vessels. The design of the transmission and reception electronic circuits is described by the authors. The piezoelectric transducers used are approximately 8 mm in diameter. The transmission is performed through a 7 mm-thick aluminium wall. The achieved power transmission is 30 mW with 80 % efficiency and the data transmission rate is 1 kbps at the carrier frequency of 3 MHz.

Moss (2010) of the Australian Defence Science and Technology Organization describes a detachable ultrasonic feed-through. The two units of the device (transmission and reception) are equipped with magnets which clamp the units over a non-magnetic aluminium wall. In the experiment described, the wall is 1.6 mm thick and the reported transmission efficiency was 34%. One can expect that the low transmission efficiency may be caused by the ineffective coupling between the piezoelectric transducers and the material surface occurring in a detachable system.

Neasham (2010) and Graham (2011) of Newcastle University describe a prototype system aimed at transmitting energy and data through the steel walls of ships. The device used electromagnetic transducers (coils) to generate and receive ultrasonic waves in an 80 mm-thick wall. The authors emphasise that, in comparison to piezoelectric transducers, the operation of electromagnetic coils did not depend on the quality of the surface-to-surface coupling between the transducer and the wall. This is important in the intended marine application, where wall surfaces are often covered with paint or are corroded. The power transmission efficiency quoted by the authors is relatively low (6 %) and the data transmission speed was 2 kbps.

2.2.5. Through-thickness transmission in medical engineering applications

Ultrasonic energy transmission has also been considered in the medical application of supplying power to implanted devices. In such devices battery life is currently a problem. Batteries typically need replacement every few years and this requires an operation in order to access the implant. A method of supplying power wirelessly to the implant would thus spare the patient the need to periodically undergo surgery. Denisov (2010) used simulation to compare the efficiencies of inductive (i.e. electromagnetic, using coils and an oscillating electromagnetic field as the transmission medium) and ultrasonic energy transfer methods in medical

applications. According to his results, at a transmission distance of 10 mm the inductive method is more efficient than the electromagnetic method (81 % vs. 39 %). At a distance of 100 mm, however, the inductive method becomes significantly less efficient than the ultrasonic method (0.013 % vs. 0.2 %).

Table 2.3 contains a summary of medical ultrasonic power delivery designs reviewed by the author. Larson *et al.* (2011) describes an electric nerve stimulator powered by ultrasound. The device is 2 mm in diameter and 16 mm long. It contains a ∅1.13 mm piezoelectric transducer, a rectifying diode and a capacitor. The transmission unit uses a transducer 26 mm in diameter. The reported power throughput is 2 μW across the distance of 120 mm in muscle tissue. The authors mention that achieving a correct alignment between the reception transducer and the direction of the ultrasound beam is a major factor affecting the efficiency of transmission. In their design the problem is minimised by using a transducer whose size is less than half of the ultrasound wavelength.

Maleki *et al.* (2011) of Purdue University describe an 8 mm-long implantable oxygen generator. The device used a 1×1×5 mm reception piezoelectric transducer. The system transmitted 0.3 mW across a distance of 30 mm in muscle tissue.

Table 2.3. Overview of medical engineering through-thickness ultrasonic energy transmission research

Group	Reference	Transducer type	Medium	Dist-ance [mm]	Frequen-cy [kHz]	Trans-mitted power [mW]	Effi-ciency [%]	Drive voltage [Vpp]
Arizona State University	Larson 2011	Piezo crystal Tx ∅ 26 mm Rx ∅1.13 mm	Muscle	120	1000	0.002	n/d	n/d
Purdue University	Maleki 2011	Piezo crystal Rx:1×1×5mm	Muscle	30	2300	0.3	n/d	50

2.3. Summary

In this chapter the previously published work on aircraft maintenance and structural health monitoring was presented, thus explaining the context in which the project described in this thesis is placed. Subsequently the previous work on ultrasonic energy transmission in various engineering applications was discussed. This gave an overview of performance figures achieved so far.

The following chapter explains why guided plate waves, instead of bulk acoustic waves, are best suited for the use in a long-distance energy transmission application, such as the one described in this thesis. Characteristics of the guided plate waves important for the investigated application are also presented in detail.

Chapter 3. Characteristics of Lamb waves

3.1. Introduction

In this chapter the case for the use of ultrasonic Lamb waves as the energy transmission medium is explained. Characteristics of Lamb waves which are important to the operation of the energy transmission system are described. Wavelengths and mode shapes in the frequency range concerned as well as the wave generation and reception with the use of several types of transducers are described.

3.2. Lamb waves as an energy transmission medium

While the amounts of transmitted power and efficiencies of ultrasonic energy transmission systems reported in literature are sufficient for use with an aircraft SHM system, the transmission distances, not exceeding 15 centimetres, are not. This suggests the need to use a different energy transmission principle than those investigated previously. Such a principle is available. The fact that the aircraft structure is built from thin plates allows the use of acoustic guided plate waves – the so-called Lamb waves – as the energy transmission medium instead of the previously investigated bulk acoustic waves.

Lamb waves were first described by Horace Lamb in 1917 (Lamb 1917). They are acoustic (elastic) waves which propagate in plates considered thin, i.e. those whose thickness is smaller than the waves' wavelength. Wave propagation is bound and guided by the plate surfaces. This results in a significantly reduced attenuation, allowing the wave to propagate over large distances, of the order of many metres. This makes them particularly suitable for the ultrasonic energy transmission application. In the following sections the characteristics of Lamb waves important for this application are described in detail.

The commercial software package 'Disperse' was used to calculate the Lamb wave characteristics for the plate material, thickness and the frequency range relevant to the designed system. In-depth information about Lamb wave theory can be found in standard books such as Viktorov (1967) or Krautkramer (1983). The calculation method employed by Disperse is described, among others, by Dalton (2000). More information about the software can be found on the product website (Disperse 2013).

3.3. Mode shapes

In their behaviour, Lamb waves differ significantly from bulk and surface acoustic waves. The motion of individual material particles in a plate through which a Lamb wave is passing follows elliptical paths. This is different than in the case of bulk waves, where particles oscillate along straight line sections.

Multiple Lamb wave modes can concurrently propagate through the same plate. The number of coexisting modes as well as their characteristics depends on the plate material and the frequency × plate thickness product. At the minimum, below a certain frequency × plate thickness value, two modes exist: one asymmetrical and one symmetrical. These are denoted A_0 and S_0. With the increase of the frequency × plate thickness product further modes appear. These are denoted A_1, A_2, S_1, S_2, etc. The plate deformation shapes associated with asymmetrical and symmetrical modes are illustrated in Figure 3.1.

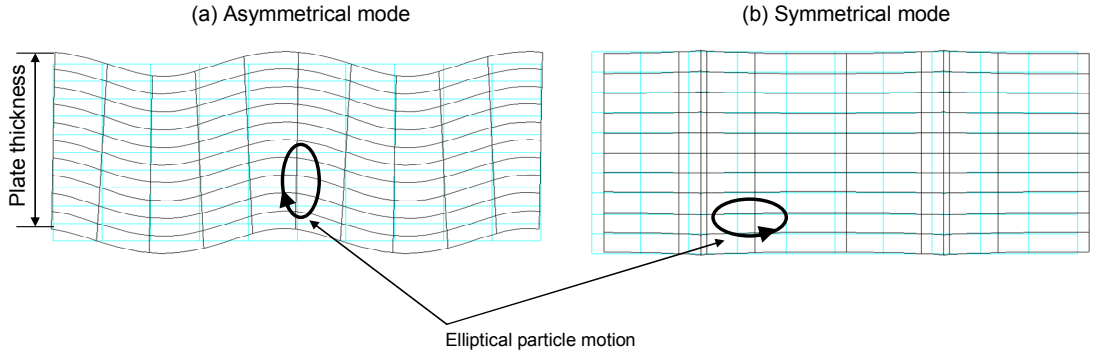

Figure 3.1. Illustration of Lamb wave mode shapes, (a) the asymmetrical mode A_0, (b) the symmetrical mode S_0. Drawings generated by Disperse software. Higher modes have similar shapes, with only exact proportions changed.

The illustrations in Figure 3.1 show several basic characteristics of symmetrical and asymmetrical Lamb wave modes which are of importance to the ultrasonic system designer. Asymmetrical modes are characterised by a relatively large out-of-plane motion (displacement) amplitude. In comparison, symmetrical modes exhibit nearly no out-of-plane motion. Asymmetrical and symmetrical modes are also characterised by comparable magnitudes of in-plane strain amplitudes. (For an explanation of the in-plane (IP) and out-of-plane (OOP) direction naming conventions refer to Figure 3.2.)

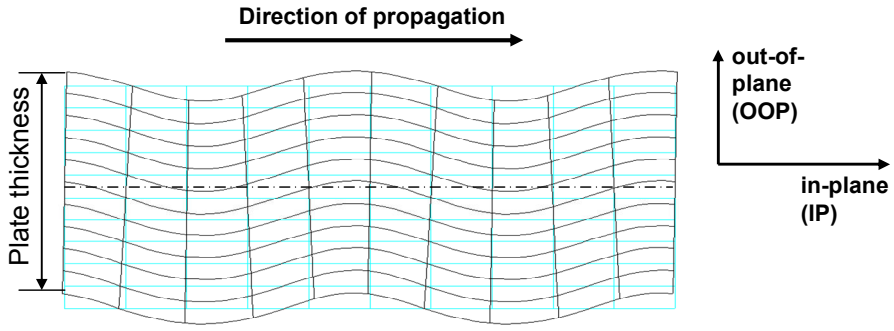

Figure 3.2. Direction naming convention in description of Lamb wave oscillation.

Figure 3.3 and Figure 3.4 show these characteristics quantitatively. The information shown was calculated using the Disperse software. Shown are data for the first two Lamb wave modes – referred to A_0 and S_0 – occurring in a 1.5 mm-thick aluminium plate within the frequency range of 30 to 190 kHz used in the energy transmission system developed during the project described in this thesis.

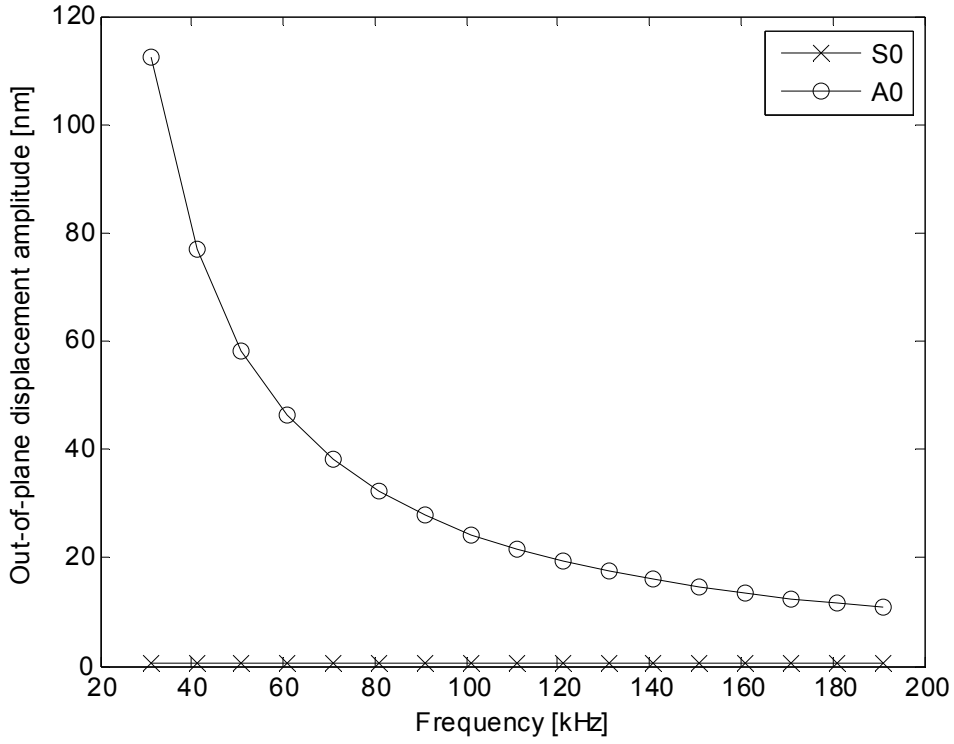

Figure 3.3. Out-of-plane surface displacement amplitude plot for Lamb wave in 1.5 mm-thick aluminium plate. Strain magnitudes calculated for a 1 W/m (metre of plate width at 1.5 mm thickness) energy flux in each mode.

The magnitudes of displacement and strain are calculated with the assumption that each mode, at each frequency, carries the energy flux of 1 W/m of plate width at

the assumed thickness of 1.5 mm. As shown in Figure 3.3, the out-of-plane displacement amplitude of the A_0 mode decreases significantly with frequency, changing in the range from approximately 115 nm to 10 nm. The S_0 mode out-of-plane displacement amplitude is less than 1 nm and remains constant throughout the frequency range. As shown in Figure 3.4, the in-plane strain amplitude of the A_0 mode is only two to three times larger than the corresponding S_0 mode amplitude.

It should be emphasised that the quantities shown in Figure 3.3 and Figure 3.4 were calculated for the specific case in which the energy flux of both modes is fixed at 1 W/m. Such a situation is rare in practice. Depending on the type of transducer used as well as the frequency, the excitation strength of each mode changes widely. Thus, it is not uncommon to observe an S_0 mode which has a larger in-plane strain amplitude than the coexisting A_0 mode. However, the difference between the out-of-plane displacement amplitudes of the two modes is so large that in practice the A_0 mode nearly always has a larger OOP displacement amplitude than the S_0 mode.

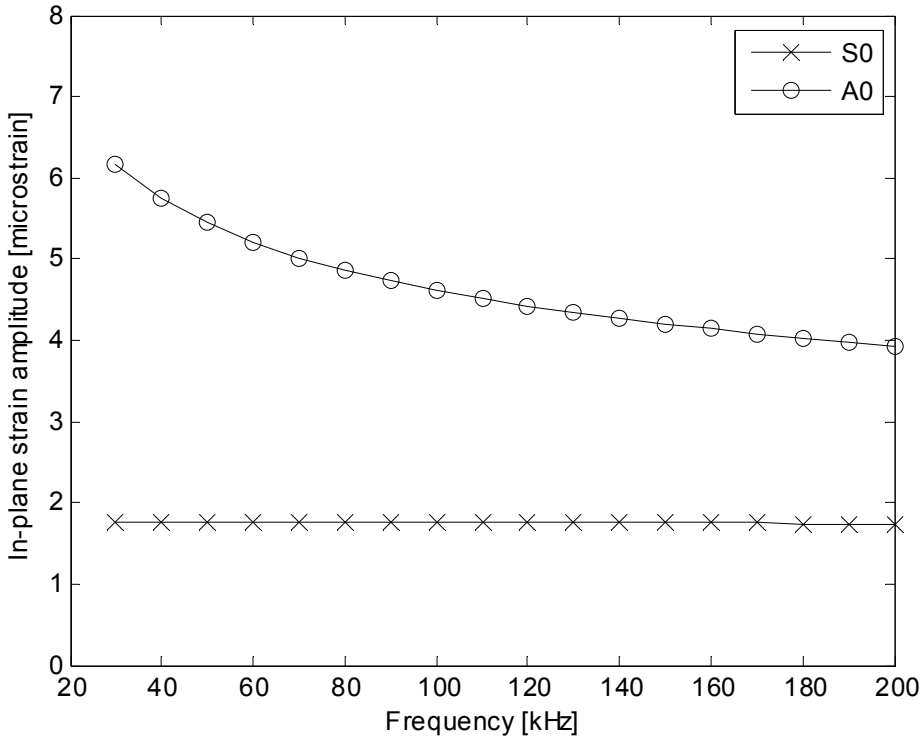

Figure 3.4. In-plane surface strain amplitude plot for Lamb wave in a 1.5 mm-thick aluminium plate. Strain magnitudes calculated for a 1 W/m (metre of plate width at 1.5 mm thickness) energy flux in each mode.

3.4. Dispersion curves

For a given plate material, the propagation velocity of Lamb wave modes changes with the product of the frequency and the plate thickness. This again constitutes a significant difference from bulk acoustic waves, whose velocity is independent of frequency and material properties.

An intermittent Lamb wave signal (i.e. a pulse containing a finite number of wave cycles) will propagate, as a whole, at a velocity different to the propagation velocity of the wave itself. The propagation velocity of the pulse is referred to as the group velocity. The propagation velocity of the wave is referred to as the phase velocity. For a given material, both velocities change with the product of frequency and plate thickness, and each velocity follows a different curve. These curves are referred to as dispersion curves. An illustration of dispersion curves for a fixed material type (aluminium) and a fixed plate thickness (1.5 mm) is shown in Figure 3.5.

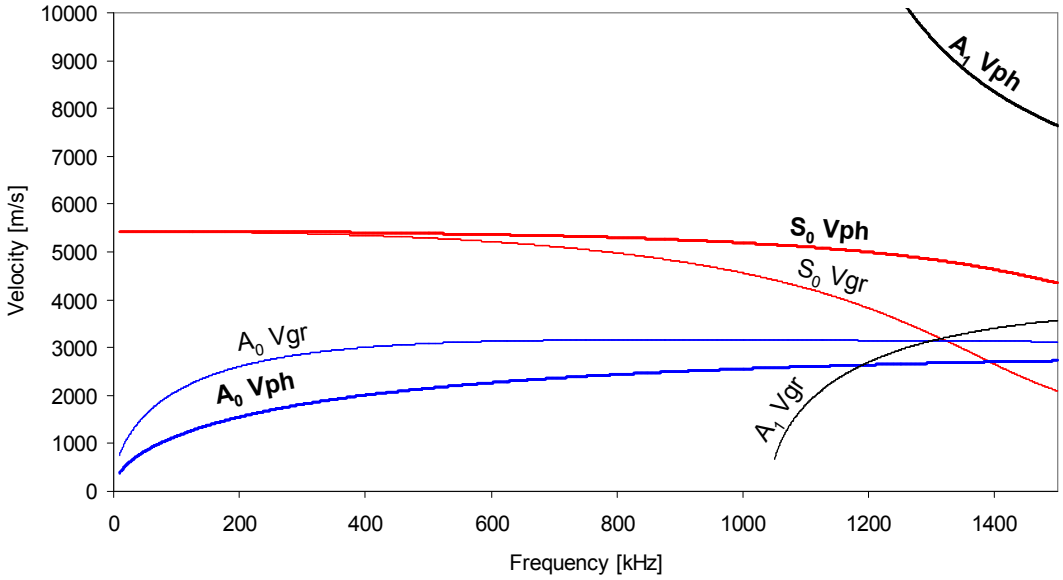

Figure 3.5. Example Lamb wave dispersion curves for a 1.5 mm-thick aluminium plate in the frequency range 0 - 1500 kHz. Phase (v_{ph}) and group (v_{gr}) velocities are shown. With further increase of frequency more modes will appear.

The coexistence of differing phase and group velocities is referred to as dispersivity. Dispersivity results in the lengthening of a pulse during its propagation and a consequent decrease in its amplitude. Such behaviour is known as dispersion (Figure 3.6). It should be emphasised, however, that in the energy transmission

system described in this work the Lamb wave signal is transmitted continuously. Therefore dispersion does not occur.

As a consequence of the changing propagation velocities, the relationship between Lamb wave wavelengths and frequency is nonlinear (Figure 3.7).

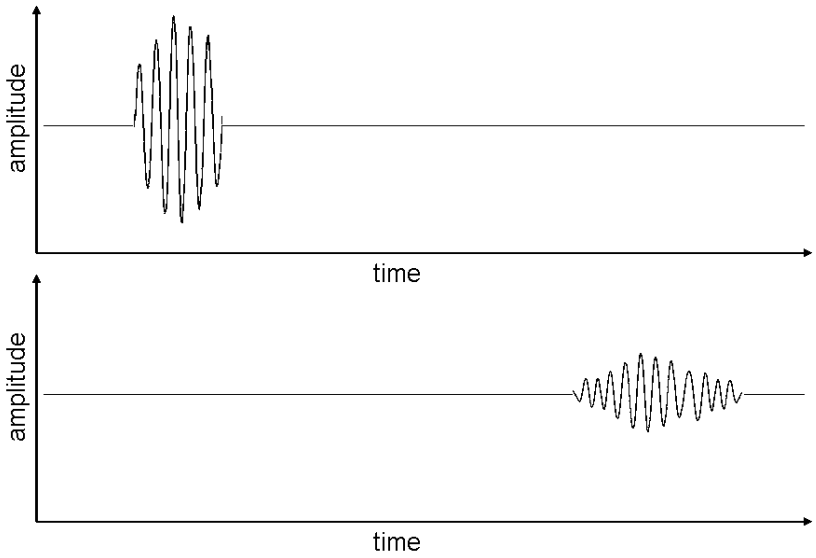

Figure 3.6. Illustration of the Lamb wave pulse dispersion. Note that the wavelength remains constant, but the pulse envelope lengthens to encompass more wave cycles. The amplitude correspondingly reduces as the total amount of energy in the pulse is maintained. (The oscillation amplitude shown can refer to any relevant characteristic of the wave, e.g. surface displacement or strain.)

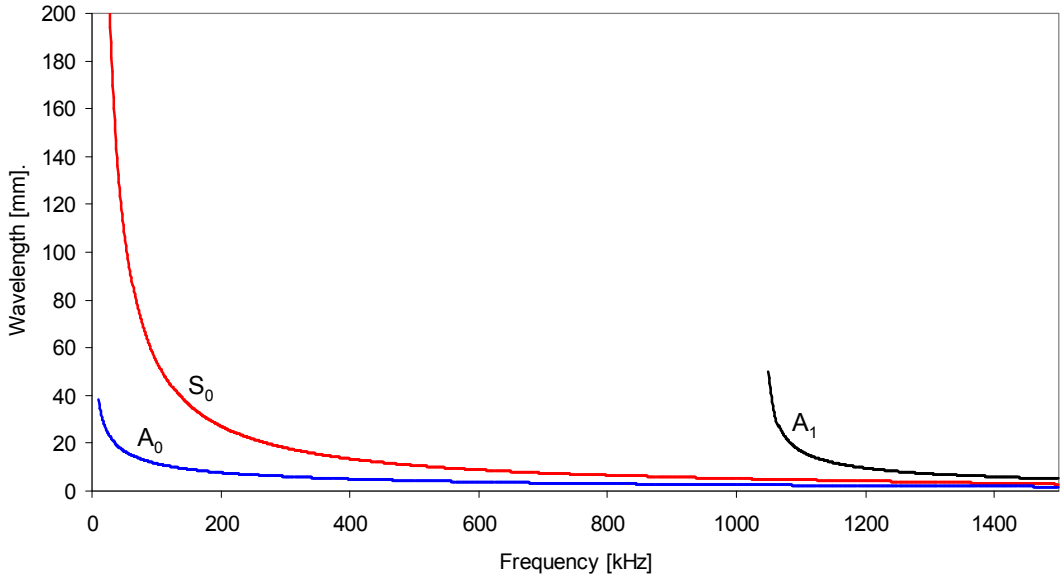

Figure 3.7. Example plot of Lamb wave wavelengths for a 1.5 mm-thick aluminium plate in the frequency range 0 - 1500 kHz.

3.5. Attenuation and other types of signal amplitude decrease

Several factors contribute to the decrease of the Lamb wave signal amplitude as it propagates. Two are classified as attenuation: material absorption and leakage. Material absorption (viscoelastic damping) is caused by friction between the particles of the material in which the Lamb wave propagates. The absorbed portion of the wave energy is converted to heat. Viscoelastic damping is prominent in materials such as polymers, rubbers and composites (Luangvilai 2007). In metals this kind of attenuation is negligible at distances of the order of metres, and thus is not considered a problem in the energy transmission application described in this thesis.

Leakage occurs when a portion of the Lamb wave energy is transferred to the medium surrounding the plate in which the wave propagates. This mechanism is prominent when the plate is surrounded by a dense material, such as a liquid or a solid. If the surrounding medium is air, leakage is negligible. In the laboratory set-up of the energy transmission system described in this text, the test panel was placed on several foam blocks and hence surrounded by air. In the author's experience variation in the location of the foam blocks did not influence the Lamb wave pattern in the plate. Thus, the leakage loss to the blocks is considered negligible.

Thus, the leakage loss to the blocks is considered negligible. In a practical application, however, the Lamb wave propagation path may pass through sections of the wing skin forming walls of fuel tanks. Thus, the energy leakage into aircraft fuel requires further investigation. Moreover, the aircraft skin is supported by various structural elements such as spars and ribs. These elements are made of aluminium or composites. It is expected that the leakage into these structural elements will become a major cause of the Lamb wave signal loss. Further investigation is needed into the operation of the energy transmission system in a plate supported by structural members.

Two further amplitude loss factors are not classified as attenuation. These are geometric spreading and dispersion. The geometric spread of Lamb waves is limited in comparison to the spread of bulk waves. Bulk waves spread in a three-dimensional space, whereas the Lamb wave is contained between the surfaces of the plate and thus spreads in a two-dimensional space. Furthermore, the square patch-type transducers used to generate Lamb waves in the investigated energy transmission system proved to be strongly directional, sending a narrow beam of vibration along

their axes of symmetry. Therefore in the investigated set-up the geometric spread of the signal was minimised.

Dispersion of Lamb wave pulses also results in a decrease of the signal amplitude. In damage detection applications, where transient signals are used, dispersion is considered the major cause of the amplitude loss. Damage detection systems designers often strive to use frequencies at which the phase and group velocities of the Lamb wave modes used are similar, therefore minimising dispersion. In the investigated energy transmission application, however, dispersion is not a concern. This is because in this application a continuous signal is used and the pulse propagation characteristics are not applicable.

3.6. Generation and reception

In practical applications Lamb waves are generated by applying mechanical vibration to the surface of the plate. This is typically done with the use of a piezoelectric transducer converting an AC electric signal of the chosen frequency to vibration. (The transducer used to generate Lamb waves will be further referred to as the transmitting transducer.) The configuration of the transmitting transducer has a strong effect on the Lamb wave generation - in particular the relative strength with which different modes are excited. The characteristics of various transducer configurations have been thoroughly researched. A brief summary of the relevant literature follows.

Figure 3.8 illustrates the three most common transmitting transducer configurations. A single transducer vibrating out of plane (Figure 3.8 (a)) generates bulk acoustic waves which, through a couplant (not shown) propagate into the plate and excite the Lamb waves (Giurgiutiu 2005). Such transducers are typically used in laboratory damage detection applications and are made of a block of a piezoelectric material. Typical dimensions are of the order of 10 to 20 mm in diameter and height. Because of their size and stiffness, bulk transducers have a well-defined resonance frequency and operate efficiently only within a narrow window around this frequency.

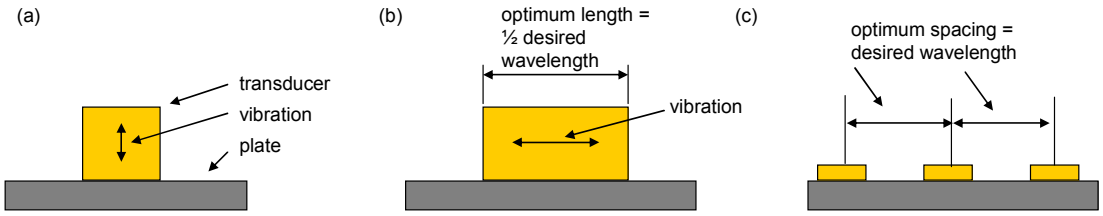

Figure 3.8. Illustration of three basic Lamb wave transmitting transducer configurations. (a) transducer vibrating out of plane, (b) transducer vibrating in plane, (c) comb transducer built of multiple transducer units spaced by the distance equal to the desired Lamb wave wavelength. All transducers vibrate in the same direction (either in plane or out of plane) and phase.

A transducer vibrating in-plane couples directly to the in-plane strain field of the Lamb wave (Figure 3.8 (b)). In order to transmit the in-plane stress a strong couplant, such as epoxy, must be used. In-plane-vibrating transducers are typically square and relatively thin (less than 1 mm) patches of piezoelectric material. Such transducers typically are not resonant and can be efficiently operated over a wide frequency range. A theoretical model of the Lamb wave excitation by a patch transducer was developed by Giurgiutiu (2005). According to the model, the shear stress transmission from the transducer to the plate occurs only near the edges of the transducer. This is caused by a combination of the differing stress fields of the transducer and the Lamb wave (a free transducer expands linearly, whereas Lamb waves have a more complex strain distribution along the wavelength) with the stiffnesses of the thin transducer, the couplant and the plate. The model also defines the optimum transducer length as an odd multiple of ½ the generated Lamb wave mode. Outside of the optimum length the mode excitation effectiveness changes nonlinearly, reaching minima at odd multiples of the full wavelength. The S_0 mode wavelength is an even multiple of the A_0 mode only at selected frequencies (e.g. 32, 145 and 1041 kHz in a 1.5 mm aluminium plate). Only at these frequencies it is possible to excite one mode with a maximum strength while suppressing the other. At other frequencies (which is a more typical case) a transducer optimised to one mode will also generate another with a considerable strength.

The comb transducer set-up comprises several smaller transducers separated by a set distance (Figure 3.8 (c)). The operation of such a transducer was modelled by Grondel (2002). In his publication the transducers used operated in-plane, although one can expect that a comb set-up built of out-of-plane operating transducers will also work. The optimum spacing between the transducers is equal to the wavelength of the Lamb wave mode to be generated. In most cases other modes, to which the

set-up is not tuned, will be excited. Modes having a wavelength twice as long as the distance between the transducers will be suppressed.

The reception of the Lamb wave signal can be carried out by any type of transducer. The patch transducer, however, is of particular interest as it couples to the strain field of the Lamb wave passing underneath (Di Scalea 2007). Thus it is assumed that the strain field of the transducer is the same as the strain field of the plate surface to which it is attached. The transducer strain field is in turn coupled to the electric field in the transducer through the piezoelectric constant. In turn, the overall voltage produced by the transducer is proportional to the average of the strain calculated over the transducer area. The maximum reception efficiency occurs when the wavelength of the received Lamb wave is equal to 1.5 times the transducer length (Haig 2010). For waves shorter than this value the decrease of the reception efficiency is rapid, for longer wavelengths the decrease is significantly slower (Figure 3.9). In practical applications, however, the situation is more complicated. Usually, at least two superimposed Lamb wave modes, each with a different wavelength and with unknown phase differences in relation to one another, pass underneath the receiving transducer. These superimposed modes can therefore produce a strain with a near zero average over the transducer area even if the transducer is matched to the shortest wavelength mode.

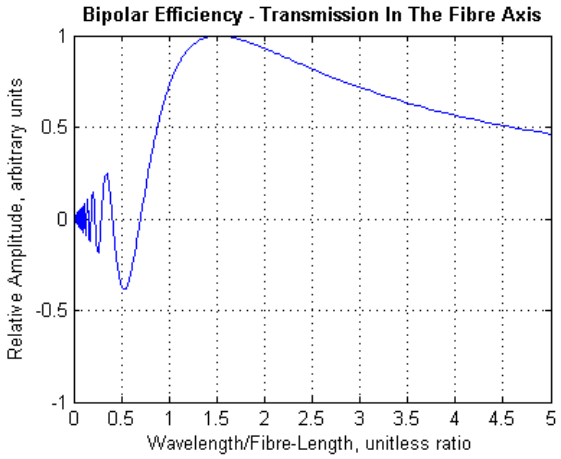

Figure 3.9. Efficiency of Lamb wave reception by a patch transducer coupled to the in-plane strain field of the Lamb wave. Source: Haig (2010).

3.7. Measurement method

The measurement of Lamb wave-related surface motion is typically carried out using a laser vibrometer. A vibrometer uses the Doppler shift of a reflected laser beam to measure the instantaneous velocity of a surface. Thus, it is able to measure the changing velocity of the plate surface caused by the passing of Lamb waves. In order to measure the out-of-plane motion, a single laser head with the beam approximately perpendicular to the measured surface is used. Such a set-up is referred to as the one-dimensional (1-D) laser vibrometer. In order to measure the in-plane surface motion, a set up of two or three laser heads must be used. The heads are positioned in such a way that the laser beams are orientated at an angle to the plate surface and are pointed at the same measurement point. From the data coming from all laser heads two or three velocity components are calculated. Such set-ups are known as 2-D or 3-D laser vibrometers. The laser heads typically offer an automatic scanning capability thanks to a built in moveable mirror. A complete scanning vibrometer set-up, including a PC with control software, is able to produce an image of Lamb wave motion over a large area of a plate surface. In the author's experience areas of 1 × 1 m were scanned without difficulty.

A 1-D scanning laser vibrometer was available to the author. Thus, only the out-of-plane motion component could be measured. In order to derive the in-plane strain amplitudes, the information shown in Figure 3.3 and Figure 3.4 was used. The ratio between the OOP displacement and the IP strain was calculated, for each Lamb wave mode separately, from the data presented in these figures. Subsequently, the IP strain amplitudes were calculated from the measured OOP displacement data. Such an operation required a correct identification of Lamb wave modes. This was done by referring to the wavelengths shown in Figure 3.7 and comparing them with the wavelengths of the waves imaged by the scanning laser vibrometer.

3.8. Summary

In this chapter the characteristics of Lamb waves and their suitability for application in a long-distance ultrasonic energy transmission system were described. In the preceding two chapters the requirements for such a system designed to supply power to aircraft SHM sensor nodes were presented.

In the following chapter the application of these requirements and characteristics in the design of a laboratory prototype of a Lamb wave energy transmission system is described. The conceptual design is first explained, followed by a description of the resulting laboratory setup.

Chapter 4. Experimental energy transmission setup

4.1. Introduction

In this chapter the design of the experimental setup used in the project is described. The assumptions and simplifications adopted in order to model a fragment of the intended operating environment – an aircraft structure – in the laboratory are explained. The geometry as well as the design of the associated electric circuits are described. The choice of the investigated ranges of operational parameters, such as the frequency and voltage, is explained. Finally, a block diagram of the laboratory setup is presented and the experimental as well as computer simulation tasks carried out in relation to particular setup components are listed.

4.2. Conceptual design

The block diagram shown in Figure 4.1 illustrates the conceptual design of the investigated energy transmission system. The diagram shows the main system components and the sections of the system in which electricity or ultrasound are the energy carrier.

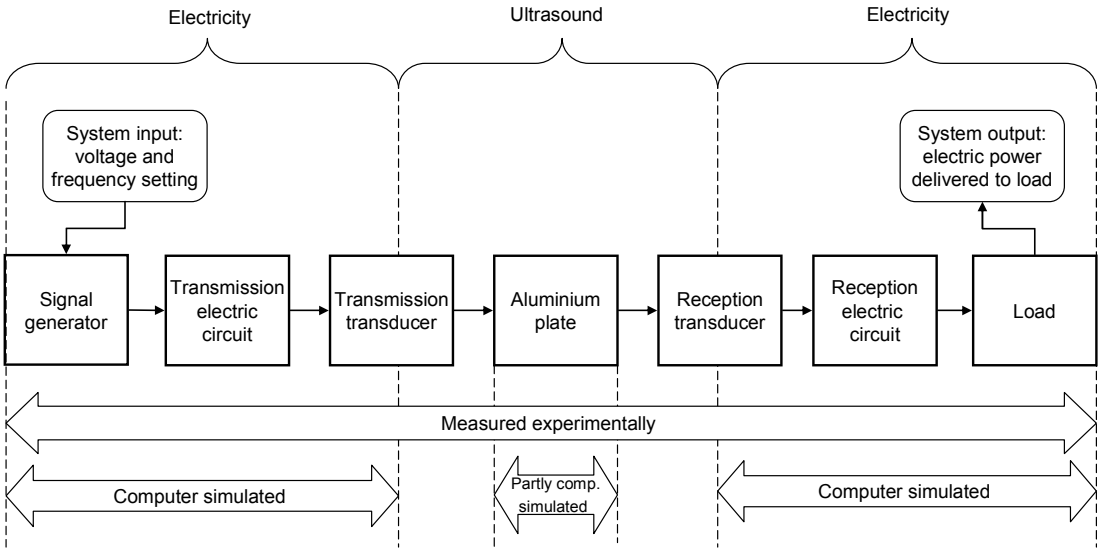

Figure 4.1. Block diagram of the experimental energy transmission setup, also showing areas of experimental and computer simulation work.

The input and output of the complete system are also shown. These are:

- Input: the voltage and frequency setting on the signal generator.

- Output: the electric power delivered to the load.

An experimental setup was built to according to the concept presented in Figure 4.1. The detailed design of this setup is described in the following section.

4.3. Experimental setup

4.3.1. Mechanical design

The experimental setup was designed to model an aircraft skin panel in a simplified form. In a jet transport (e.g. Airbus A320) wing structure stringers attached to the underside of the wing skin are approximately 150 mm apart, the distance between the ribs varies significantly with the typical value being 600 mm and the distance between the front and the rear spar is 2400 mm near the wing root and decreases towards the wing tip (Grigg 2013). This indicates that the distance over which the Lamb waves will travel in the wing skin without being interrupted by structural elements will be in the range between 150 mm (between stringers) and 600 mm (along the stringers, between ribs). The passing of the ultrasound through structural elements is likely to cause reflections and signal loss.

A single 1000 × 821 mm aluminium plate was used as a laboratory model of an aircraft skin panel (Figure 4.2.). Underlying structural elements such as ribs and stringers were not included, since it was decided that at this stage of work the basic characteristics of the Lamb wave energy transmission method would be best investigated in a simplified structure model. The addition of structural elements to the model would have complicated the ultrasound propagation patterns and could have obscured basic characteristics of the phenomenon. The plate was 1.5 mm thick and made of non-aviation grade 6082-T6 aluminium. It was decided that the acoustic properties of the standard stock thickness and grade of the aluminium sufficiently resembled those of an aviation-grade material while allowing a significant reduction in the cost of the experimental setup. The choice of the material was discussed with the project sponsor. In all experiments the plate was placed on a set of foam blocks. The blocks provided acoustic insulation, minimising the influence of the supporting elements on the propagation of acoustic waves in the plate.

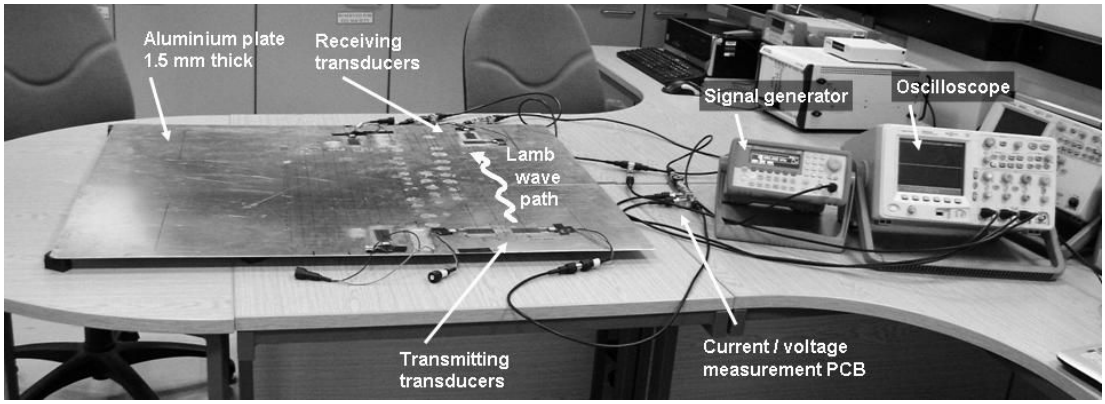

Figure 4.2. Photograph of the experimental setup.

Pairs of piezoelectric transducers used to generate and receive Lamb waves were positioned along the longer edges of the plate at the locations shown in Figure 4.3. The distance between transducers in each pair was 535 mm. This distance corresponded to the approximate 600 mm distance between aircraft wing ribs. The distance also ensured the placement of the transducers sufficiently far from the edges of the plate as to allow the observation of the Lamb wave propagation between these transducers and the edge.

The transducers were bonded to the plate with the use of a Vishay epoxy resin marketed for the use with strain gauges. The bonding process was handled by a technician experienced in working with strain gauges.

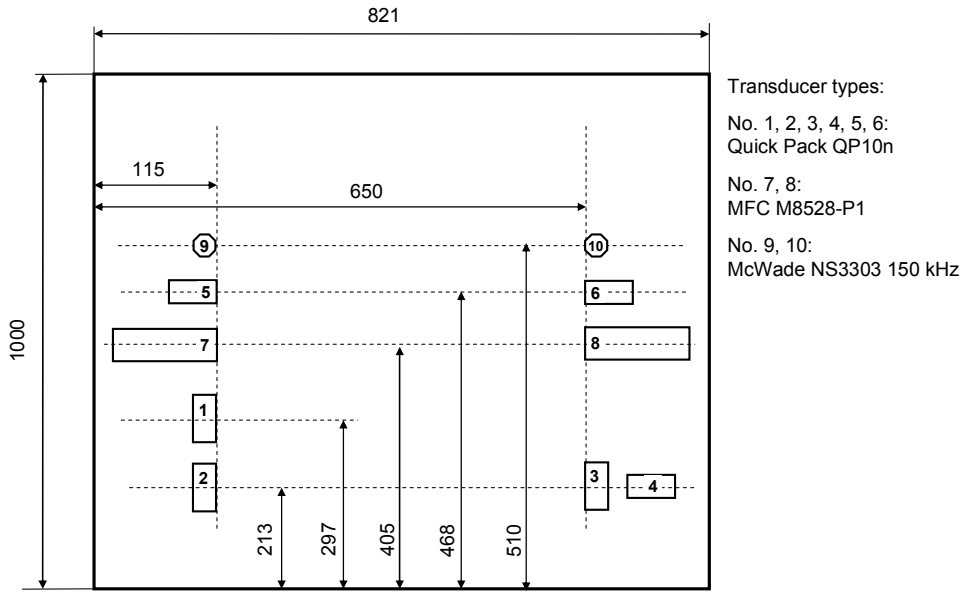

Figure 4.3. Dimensions of the experimental aluminium plate and locations of transducers.

4.3.2. Electric circuits

Dedicated electric circuits were designed and built in order to facilitate the drive of the transmission transducer and the reception of electric energy from the receiving transducer as well as the measurement of the input and output electric power. The circuits are shown in Figure 4.4.

The transmission circuit comprised a transmission piezoelectric transducer, an Agilent 33220A signal generator and a 1 Ω series resistor for current measurement. The signal generator was used to supply a continuous sinusoidal signal driving the transmission transducer. In some configurations an inductor was added to compensate for the capacitive characteristics of the transducer. (The operation of the circuit elements is described in detail in Chapter 5.

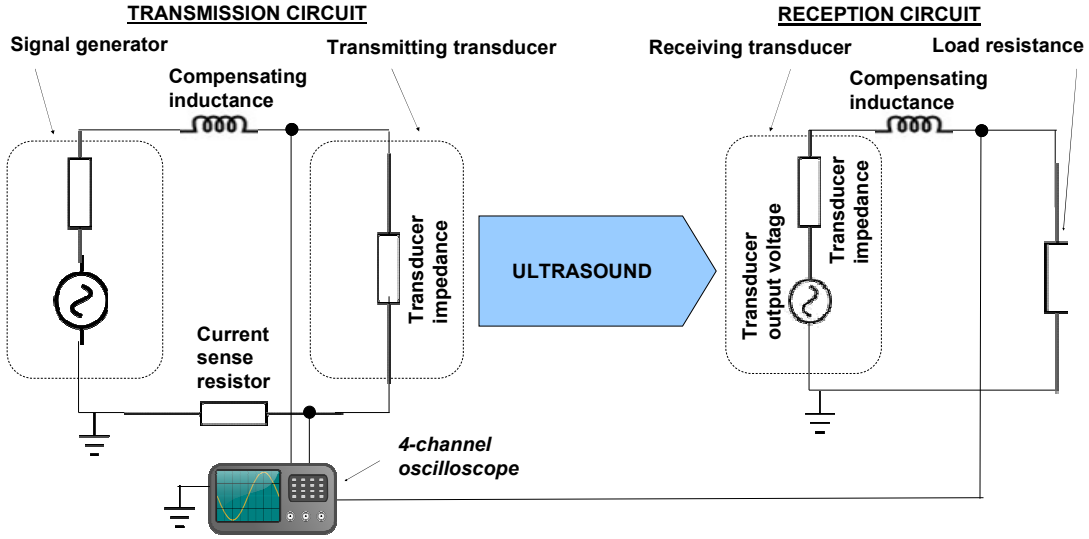

Figure 4.4. Electric circuit diagram of the experimental energy transmission setup.

The reception circuit consisted of a receiving piezoelectric transducer, a load resistor and, in selected configurations, a compensating inductor. The value of the load resistor was set to be an approximate match to the resistance of the transducer type used. It was 10 Ω for the Quick Pack QP10n and MFC 8528-P1 transducers and 150 Ω for the McWade NS3303 transducer.

The input power measurement was realised with the use of two digital oscilloscope channels allowing the measurement of the amplitudes and phases of the voltages across the transmission transducer and the current sensing resistor. The output power measurement was carried out with one oscilloscope channel measuring the amplitude of the voltage across the load resistor. Data from the oscilloscope were

downloaded to a PC and processed using a MATLAB script. A detailed description of the data processing routine follows in Chapter 5.

4.3.3. Operating parameters

In all experiments modelling the intended energy transmission operation, the transmission transducer was driven by the signal generator using a continuous sinusoidal voltage signal. The use of a continuous signal is a marked difference from the typical mode of operation used in ultrasonic damage detection applications, in which signal pulses of several sine cycles are used. To the author's knowledge this project is the first published effort investigating the continuous transmission of Lamb waves.

A pulsed sine signal was used in selected experiments designed to measure the transmission characteristics of the investigated transducers types. These experiments are described in section 6.4.

The voltage amplitude of the signal generator was typically set to the maximum available value of 20 V peak-to-peak (Vpp). The frequency range used in most experiments was 20 – 200 kHz. The choice of this frequency range was based on the following considerations:

- The minimum operating frequency of the system must be above the human audible range. Using lower, audible frequencies in a practical system could be disturbing to the aircraft passengers and crew. This dictates the minimum frequency of 20 kHz. (The influence of the frequencies used by the system on animals which can hear above 20 kHz may need to be checked as well, as possible negative effects may concern both animals transported on the aircraft and those living in the vicinity of the airport. Another area of concern requiring investigation would be interference with the operation of hearing aids.)
- The maximum frequency was chosen based on the characteristics of the off-the-shelf transducer types used in the project. As detailed in Chapter 5. , simulations based on the measured electric impedance characteristics of transducers indicated that in the majority of circuit configurations the maximum power throughput will be achieved at frequencies lower than 200 kHz. These simulated results were later confirmed in experimental measurements.
- A further factor contributing to the choice of the maximum investigated frequency was the size of the available transducer types. The dimensions of the

investigated transducers ranged from 18 mm to 85 mm. In the 20 – 200 kHz frequency range the Lamb wave wavelengths ranged from 270 to 27 mm (S_0 mode) and from 26 to 7 mm (A_0) mode. Thus waves could be investigated using transducers with dimensions comparable to their wavelength.

4.4. Scope of work

The following tasks were carried out using the experimental setup as well as its computer models:

- The operation of all system components was characterised experimentally.
- The voltage and electric current were measured at several points of both the transmission and the reception electric circuits.
- The propagation of the ultrasonic Lamb waves in the aluminium plate were measured and visualised using a scanning laser vibrometer.
- The generation of the ultrasonic waves in the transmission transducer as well as the reception of these waves in the reception transducers was also mapped in detail with the vibrometer.
- The operation of the transmission and reception electric circuits was simulated using a MATLAB code. A good match with the experimental measurements was achieved.
- The propagation of Lamb waves from the transducer through the aluminium plate was modelled using the LISA finite difference method software. A good match with experiment was achieved, which proves the usability of this method for future work.

4.5. Summary

In this chapter the conceptual design as well as a laboratory prototype of the ultrasonic Lamb wave energy transmission system were described. The scope of the work carried out using this prototype system was presented.

The following four chapters present this work and its results in detail. In the next chapter the measurement and simulation of the electrical characteristics of the investigated piezoelectric transducers and the complete energy transmission system are presented. This is followed by a report on Lamb wave imaging using a scanning laser vibrometer in Chapter 6, an investigation of the setup geometry modifications in Chapter 7 and a report on Lamb wave computer simulation in Chapter 8.

Chapter 5. Electrical characteristics and performance

5.1. Introduction

In this Chapter the three transducer types investigated during the project are introduced. The details of the mechanical and the electrical designs are described and the important differences between these are explained. The measurement of the transducers' electric impedance characteristics is described and the results are presented. The computer simulation tool written to predict the performance of the system's electric circuit as well the measurement system designed to experimentally measure this performance are described. Finally, the energy transmission simulation and experimental results are presented. The performance figures achieved by the three transducer types and the performance improvements achieved with the use of inductive compensation are discussed.

5.2. Piezoelectric transducers and their characteristics

Three models of piezoelectric transducers were used and compared in the experimental energy transmission system: the McWade NS3303 150 kHz, the Mide Technology Corporation Quick Pack QP10n, and the Smart Material Corporation MFC 8528-P1. The three transducer types were built using different basic designs and differed in size. Thus, the choice allowed a comparison of the power transmission performance of three transducer design concepts and observation of how various transducer sizes interact with changing Lamb wave wavelengths. A photograph of the three transducers is shown in Figure 5.1.

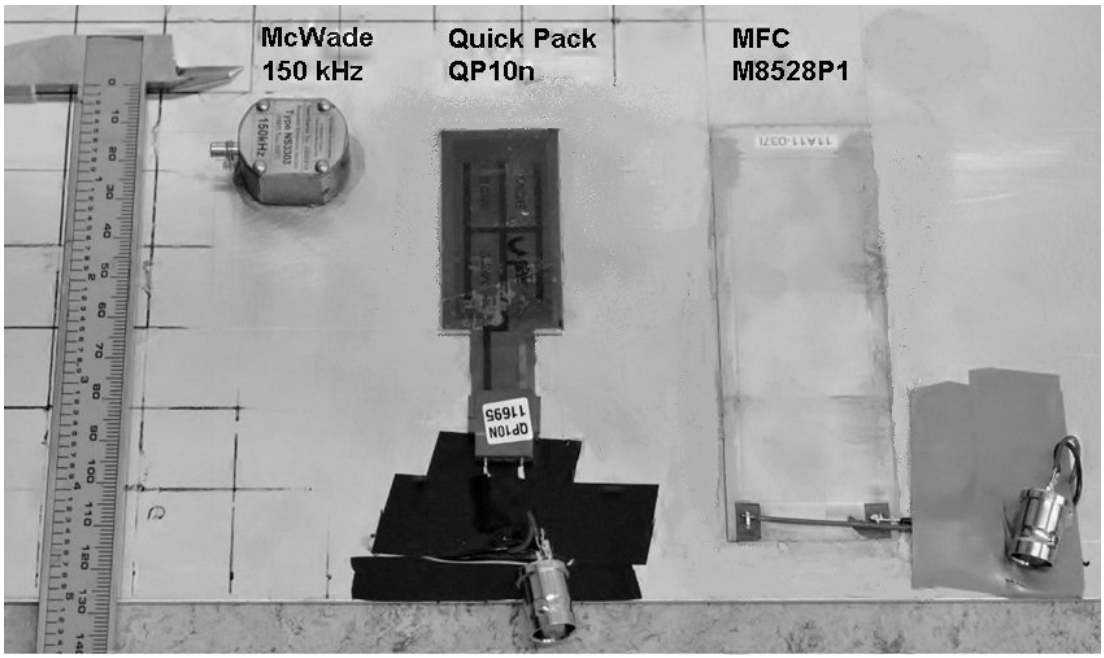

Figure 5.1. Photograph of the three types of piezoelectric transducers used in the experimental energy transmission system.

5.2.1. Basic characteristics

McWade NS3303 150 kHz

The dimensions and designs of the three transducer types are summarised in Table 5.1. The McWade 150 kHz transducer was designed for use in the acoustic emission damage detection application (McWade, n.d.). The design of this transducer was selected in consultation with Airbus and conforms to aviation specifications (Paget 2010). It has been extensively used in acoustic emission research at Cardiff University. The ultrasonic energy transmission system project draws from the University's ultrasonics experience and is targeted at an aviation application. Thus the McWade transducer was the first to be evaluated in the energy transmission application.

Table 5.1. Basic information about transducer types used in the energy transmission system

Transducer model	**Piezoelectric element type**	**Piezoelectric element dimensions [mm]**	**Enclosure dimensions [mm]**	**Electrical capacitance**
McWade NS3303 150 kHz	Bulk crystal of PZT	~∅18 (height n/d)	~ ∅20 × 15	no data provided by supplier
Mide Quick Pack QP10n	Solid crystal patch of PZT	20 × 46 × 0.25	25 × 50 × 0.5	50 nF
Smart Material MFC 8528-P1	Patch of PZT fibres	85 × 28 x 0.18	112 × 35 × 0.3	10 nF

The brass enclosure of the transducer is approximately 20 mm in diameter and 15 mm in height. On one face of the transducer is a ∅18 ceramic face plate which protects the piezoelectric element inside while allowing the transmission of vibration. The piezoelectric element inside the transducer is a bulk crystal of PZT. The dimensions of the element are not given by the manufacturer. As the enclosure was sealed permanently, it was not possible for the author to access and measure the piezoelectric element. The NS3303 transducers are manufactured in several versions designed to have different resonance frequencies: 90, 150, 300, 600, 900 kHz. The 150 kHz type has been proved to be the most usable in the acoustic emission application in plates of thicknesses similar to that used in the energy transmission project. This version was therefore used in the energy transmission setup.

Mide Quick Pack QP10n

The Mide Quick Pack series transducers are built from a 0.25 mm-thick solid sheet of PZT material (Mide, n.d.). These commercially available models are sold in several dimension versions, ranging from 33 × 6 mm to 51 × 38 mm. On both faces of the PZT sheet are electrodes which deliver electric charge to these faces and generate a uniform electric field across the thickness of the sheet. The PZT material is polarised patch thickness direction. The useful deformation of the patch, in the direction of its length and width, occurs through the d_{31} and d_{32} piezoelectric

coupling, that is in the direction perpendicular to the direction of the electric field, as shown in Figure 5.2 (Pretorius 2004).

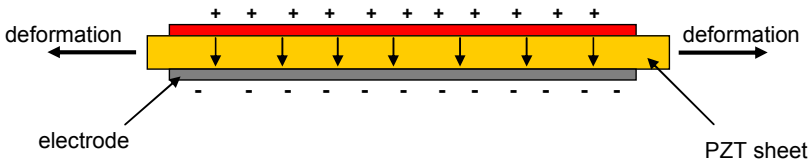

Figure 5.2. Cross-section diagram of the Quick Pack transducer showing its principle of operation. Arrows on the PZT material show direction of electric field. Enclosure not shown for clarity.

In comparison to bulk crystal transducers, such as the McWades, the Quick Pack transducers are thin and light, while having a significantly larger area within the plane in which the deformation occurs. This suggests that they are capable of achieving a significantly larger in-plane deformation than the bulk transducers. The PZT sheet is not flexible, therefore the transducer can be bonded only to surfaces which are flat or have a large radius of curvature. The transducers are brittle and need to be handled with care.

The manufacturer advertises the transducers for static or low-frequency actuation and sensing applications. The use of similarly designed "wafer sensors" for Lamb wave generation and reception has been reported in literature (Giurgiutiu 2005). At Cardiff University, Quick Pack transducers have been successfully used both in ultrasonic-frequency acoustic emission and in low-frequency energy harvesting applications (Greaves 2008).

In the experimental energy transmission system the Quick Pack type QP10n transducers were used. These transducers are a mid-sized product of the series. The dimensions of these piezoelectric patches are 20 × 46 mm. Both of these dimensions correspond to the ½ wavelength of the S_0 modes in the investigated frequency range 20 – 200 kHz (Table 5.2). Thus, the transducers offer several possibilities to test the influence of the frequency-to-transducer length matching on the energy transmission system efficiency. The transducers have an electrical capacitance of approximately 50 nF and have been safely operating with driving voltages up to 1200 V (Pretorius 2004).

Table 5.2. Frequencies at which the Lamb wave wavelengths in a 1.5 mm aluminium plate are twice the length of investigated transducer edges

Transducer edge	Edge length [mm]	Frequency at which Lamb wave wavelength is twice the transducer edge length [kHz]	
		S_0 mode	A_0 mode
QP10n short edge	20	135	n/d (less than 10)
QP10n long edge	46	59	n/d (less than 10)
MFC M8528-P1 long edge	85	32	n/d (less than 10)

Smart Material MFC M8528-P1

The Macro-Fiber Composite (MFC) transducers are manufactured by Smart Material Corporation. The MFC production process was invented at NASA Langley Research Center and subsequently licensed to the current manufacturer (Sodano 2003). The piezoelectric patch is built of multiple parallel PZT fibres in an epoxy resin matrix. The fibres are approximately 180 μm tall and 360 μm wide and separated from each other by approximately 50 μm. Such a composite structure makes the actuator flexible, which is a significant advantage over rigid actuators such as the Quick Pack. It also reduces the lateral deformation of the transducer during its intended longitudinal operation due to a reduced coupling through the Poisson's ratio. In the production process the fibres are cut from a single wafer of a piezoelectric material using a diamond saw.

The MFC fibres are actuated with the use of interdigitated electrodes (Figure 5.3). During the production process the piezoelectric material is poled longitudinally in alternating directions. During operation the interdigitated electrodes generate a longitudinal electric field with directions alternating between the electrodes. The correspondingly alternating poling of the piezoelectric material allows it to deform in a uniform way (i.e. either expand or shrink along its entire length) in response to the alternating field. Such an arrangement uses the longitudinal (d_{33}) piezoelectric coefficient (Pretorius 2004).

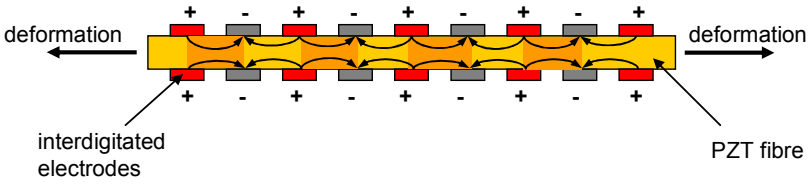

Figure 5.3. Cross-section diagram of the MFC transducer showing its principle of operation. Arrows on the PZT material show the direction of the electric field. Different shades of the PZT indicate alternating direction of material poling. Enclosure not shown for clarity.

In the experimental energy transmission system MFC M8528-P1 transducers are used. This model is one of the largest available from the manufacturer. In an early stage of this project smaller models of MFC were also tested, but the Lamb wave magnitude they generated was the smallest of several types of evaluated actuators. Therefore they were excluded from further investigation in favour of the larger M8528-P1. The length of the piezoelectric patch in the actuator is 85 mm, which corresponds to ½ of the S_0 mode wavelength at 135 kHz (see Table 5.2). The electrical capacitance is 10 nF and the transducer was shown to operate safely at voltages up to 1500 V (Prestorius 2004).

5.2.2. Operation as a generator of mechanical vibration

Regardless of the design, all piezoelectric transducers employ the same principle when operated as generators of mechanical vibration. The electrodes of the transducer are driven with an alternating voltage signal whose frequency is the same as the desired mechanical vibration frequency. The voltage generates an oscillating electric field between the electrodes. The piezoelectric characteristics of the transducer material mean that it deforms in the presence of an electric field. This behaviour is known as the reverse piezoelectric effect. The magnitude of the deformation is linked to the magnitude of the electric field through the piezoelectric constant, which is specific to the material type. Subjected to an oscillating electric field the piezoelectric element will oscillate mechanically.

In AC circuits, depending on the characteristics of the circuit components, phase shifts between the voltage and current waveform phases may occur. This is mathematically represented by using complex numbers to describe the voltage, current and power present in the circuit. The characteristics of circuit components are described by their impedance. The real number part of the impedance is the resistance and the imaginary number component is known as reactance. The theory

of AC circuit calculation is described in many general textbooks, such as (Kuphaldt 2007).

The current passing through an electric element in the presence of an alternating voltage is calculated using the AC form of the Ohm's law:

$$\boldsymbol{I} = \frac{\boldsymbol{V}}{\boldsymbol{Z}} \tag{4}$$

where $\boldsymbol{I}$ is the current, $\boldsymbol{V}$ is the voltage and $\boldsymbol{Z}$ is the impedance. All these quantities are complex numbers. (Bold typeface denotes complex numbers.)

In the AC current flowing through a circuit element a certain amount of electric power is contained (Kuphaldt 2007):

$$\boldsymbol{S} = \tfrac{1}{8} \cdot \boldsymbol{V} \cdot \boldsymbol{I}^{*} \tag{5}$$

where $\boldsymbol{S}$ is the complex number power, and $\boldsymbol{I}^{*}$ is the complex conjugate of the current. The factor $\tfrac{1}{8}$ is necessary to obtain correct values when the voltage and current amplitudes are expressed in peak-to-peak values (Vpp – volts peak-to-peak, App – amperes peak-to-peak).

The amount of power dissipated (transmitted) by the transducer in the form of mechanical vibration corresponds to the amount of electrical real power absorbed by the transducer from the driving electric circuit. The real power is the real number component of the complex AC power flowing through the transducer (Kuphaldt 2007):

$$P = \mathrm{Re}(\boldsymbol{S}) \tag{6}$$

where P is the real power.

It follows that the efficiency of the piezoelectric transducer as an electrical-to-mechanical energy converter depends in part on electrical impedance characteristics. These characteristics were therefore measured for all three transducer types used in this project. The measurement method and results are presented in Section 5.2.4.

It should be noted that the impedance characteristics describe the overall behaviour of the transducer measured at its electrical terminals. Since the transducer is an electromechanical device, its electrical impedance is a result of both electrical design features (such as the distance between the electrodes) and mechanical ones

(such as the natural mechanical resonance frequency of the piezoelectric material block). The modelling of the transducer operation was not carried out as a part of this project, therefore it is not known in what way the electrical and mechanical characteristics of the described transducer types contribute to their measured impedance characteristics. (The transducer modelling task was excluded from the project scope, since, due to its complexity, it would have significantly exceeded the allocated timeframe.)

It also needs to be emphasised that the efficiency of the energy conversion process in the transducers must be expected to be less than 100 %. Thus, the amount of transmitted mechanical vibration power is lower than the amount of the electric real power absorbed by the transducer. A precise measurement of the energy conversion efficiency of an isolated transducer, if possible, would have been a complex task likely to exceed the time allocated for this project and therefore was not carried out. (This assumption was based on the fact that no description of such a method was found in literature. The author also was not able to readily propose a suitable experiment.) The author focussed on the measurement of the overall efficiency of the complete energy transmission system.

5.2.3. Operation as a receiver of mechanical vibration

The energy conversion in the receiving transducer is the reverse of the process occurring in the transmitting transducer. The acoustic waves passing through the structure underneath the transducer induce oscillating mechanical deformation in the transducer's piezoelectric element. Through the direct piezoelectric effect the element generates an electric field, which in turn creates an oscillating voltage between the electrodes. This oscillating voltage can be measured with the transducer connected to an open circuit with no current flowing.

While the transfer of the mechanical vibration from the structure to the transducer is a complex process, a simplified description for patch transducers such as the Quick Pack and the MFC is available in literature (di Scalea 2007). According to this model, the in-plane strain field of the transducer follows the in-plane strain field of the underlying structure surface. In the case of the system described in this thesis, the surface strain of the structure is associated with the passing of Lamb waves. The instantaneous voltage generated by the transducer is, in consequence, proportional to the average of the strain field calculated over the transducer area. This model is used

in this thesis in the analysis of the strain field data obtained with the use of the laser vibrometer.

By attaching a conducting load to the transducer terminals the flow of an alternating current is made possible. The amplitude and phase of this current depends, through the Ohm's law, on the open circuit voltage generated by the transducer and the impedances of the elements of the circuit. The largest of these impedances are the impedance of the transducer itself and the impedance of the load. Others, assumed to be negligible in the experiment, are the impedances of the connecting conductors.

The match between the impedance of the load and impedance of the transducer has an effect on the amount of power that can be extracted from the transducer. The optimum match occurs when the impedance of the load is a complex conjugate of the impedance of the transducer. This means that the resistances of the two components are equal, while their reactances are of equal magnitudes and opposing signs (Kuphaldt 2007).

5.2.4. Electric impedance characteristics

The electrical impedance characteristics describe the behaviour of electric circuit elements. Knowledge of these characteristics is necessary in order to allow the prediction of the behaviour of an electric circuit by means of solving its mathematical model. Impedance characteristics are commonly known for standard circuit elements such as resistors, capacitors and inductors. Characteristics of piezoelectric transducers, however, vary significantly with the design of the transducer and are not provided by the manufacturers of any of the three transducer types used in this work.

A computer simulation model of the electric circuits used in the ultrasonic energy transmission was considered to be an important tool needed for the development of the system. In order to build such a model it was necessary to obtain the impedance characteristics of the piezoelectric transducers used. It was decided that it would be most time-effective and accurate to perform a laboratory measurement of the impedance characteristics of the specific transducer units used in the experimental set up.

The measurement was carried out using a HP 8753E network analyser. A network analyser is a device used in a wide range of measurements in the field of

radio frequency (RF) electronics (Agilent, 2004). One of its capabilities is the measurement of the reflection coefficient of the measured component. In the discussed context the reflection coefficient, $\boldsymbol{\Gamma}$, denotes the fraction of the RF signal delivered to the measured component via a connecting cable which is reflected back towards the source (in this case the network analyser). The remaining portion of the signal $(1-\boldsymbol{\Gamma})$ is absorbed by the component and converted to a different type of energy. This energy can be, among others, heat (true for all non-ideal components) or, in the specific case of piezoelectric transducers, mechanical vibration. The reflection coefficient $\boldsymbol{\Gamma}$ is a complex number and contains information about the signal phase shift which the component introduces.

In electric circuit calculations it is more convenient to use the impedance to describe the characteristics of circuit components. Reflection coefficient values obtained from a network analyser can be converted to impedance using the following formulas (Kim, 2001):

$$\mathrm{Re}(\boldsymbol{Z}) = R = \frac{1-[\mathrm{Re}(\boldsymbol{\Gamma})]^2-[\mathrm{Im}(\boldsymbol{\Gamma})]^2}{[1-\mathrm{Re}(\boldsymbol{\Gamma})]^2+[\mathrm{Im}(\boldsymbol{\Gamma})]^2}\cdot Z_0 \qquad (7)$$

$$\mathrm{Im}(\boldsymbol{Z}) = X = \frac{2\cdot[\mathrm{Im}(\boldsymbol{\Gamma})]^2}{[1-\mathrm{Re}(\boldsymbol{\Gamma})]^2+[\mathrm{Im}(\boldsymbol{\Gamma})]^2}\cdot Z_0 \qquad (8)$$

where $R = \mathrm{Re}(\boldsymbol{Z})$ is the resistance of the measured circuit element, $X = \mathrm{Im}(\boldsymbol{Z})$ is the reactance of the element and $Z_0 = 50\ \Omega$ which is the characteristic impedance of the measurement circuit.

The network analyser was calibrated before each series of measurements. Calibration proved to be a crucial step needed to obtain meaningful results. The frequency range in which the measurements were carried out (30 – 300 kHz) was at the low end of the network analyser's capability. The instrument is rated 30 kHz – 6 GHz, but the users' experience is that it is most robust at higher frequencies, whereas at lower frequencies its calibration tends to drift significantly in a short time. Calibration was always conducted at (referenced to) the network analyser's terminal. Since different types of transducers required different types of cables, it was assumed

that conducting separate calibrations in reference to the far end of each cable would be impractical.

The reflection coefficient measurement was carried out in the frequency range of at least 20 – 200 kHz using the frequency sweep function and averaged over four or more sweeps. The data was then transferred to a PC and converted to impedance characteristics using Equations (7) and (8) in an Excel chart. All transducer types were characterised when bonded to a plate. This was especially important in the case of the Quick Pack and MFC transducers. These transducers are relatively flexible in the free state and attaching them to a stiffer object significantly changed their impedance characteristics. The characteristics of the bulk crystal McWade transducers did not change when bonded. Measurements were performed for several examples of each transducer type. No significant differences between the examples were observed.

McWade NS3303 150 kHz

The impedance characteristics of the McWade transducer are shown in Figure 5.4. A distinct resonance can be observed. At resonance the reactance and the impedance angle crosses zero. At the same time the impedance magnitude reaches its minimum. For the McWade 150 transducer shown the resonance occurs at near 117kHz (with less than ± 1 kHz variation between the three tested units) and the minimum impedance magnitude is 153 Ω. Away from the resonance frequency the impedance magnitude increases steeply and the phase angle reaches values close to 90 deg. The antiresonance occurs near 150 kHz. (Resonance is defined as the condition in which the impedance reaches a minimum, antiresonance is defined as the condition at which the impedance reaches a maximum.)

It is expected that a transducer with such characteristics will transmit power efficiently only near resonance. The high magnitudes of resistance away from the resonance frequency will limit the electric current which can be passed through the transducer at a given drive voltage to near zero. The same is expected to be the case for the receiving transducer: even if a large electromotive force is generated in the transducer by a large amplitude incoming Lamb wave, very little current will flow because of the high resistance.

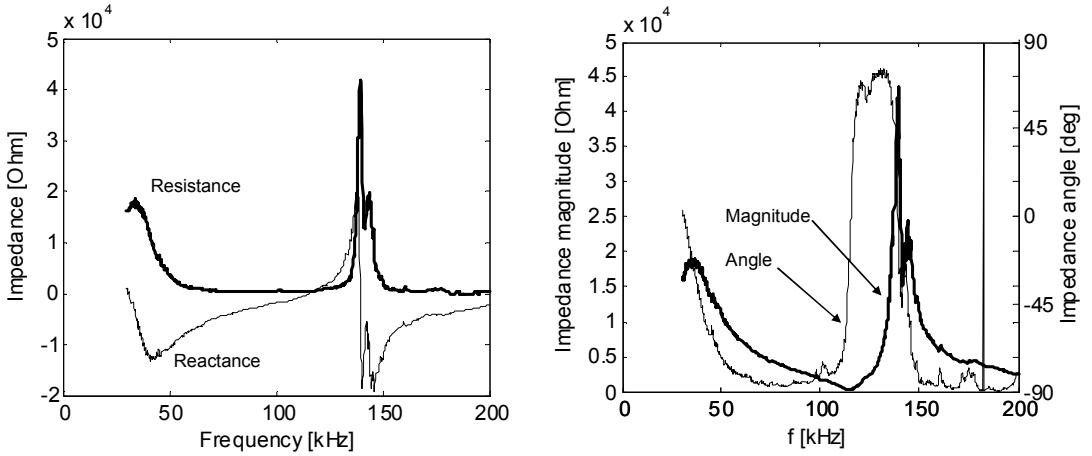

Figure 5.4. Electric impedance characteristics of McWade NS3303 150 kHz transducer (S/N 647).

Quick Pack QP10n

The impedance characteristics of the Quick Pack QP10n transducer are shown in Figure 5.5. The characteristics were measured on a transducer bonded to a 1.5 mm aluminium plate with epoxy adhesive. (As described above, a Vishay strain gauge epoxy was used and the bonding process was carried out by an experienced technician.) The measurement was carried out in the bonded state since this configuration was relevant to the power transmission system operation. Patch transducers (both Quick Pack and MFC) are relatively flexible (even the brittle Quick Pack is far more flexible than a PZT block, such a the one used in the McWade transducer.) Therefore the bonding to a metal plate significantly adds to their stiffness. Measurements in the free state were also made before bonding. These revealed that the patch transducer electric impedance characteristics differed between the free and the bonded state. This shows that the mechanical stiffness of the transducer and, consequently, its vibration characteristics affect its electrical impedance characteristics.

Unlike the block crystal McWade transducer, the solid-patch QP10n does not exhibit a first-order resonance in the tested frequency range. The measured curves, however, are jagged, which suggests the occurrence of multiple higher-order resonances throughout the tested frequency range. This conclusion is backed by the fact that the Quick Pack's piezoelectric patch is solid and stiff, which is likely to support mechanical resonance. The MFC transducer's impedance curves (shown in the subsequent section), on the other hand, are smooth. This corresponds to the

MFC's design comprising multiple thin and soft fibres, which is likely to make the transducer too soft to resonate.

The QP10n impedance is composed of a small (approximately 10 Ω) resistance component and a reactance component ranging from approximately -150 Ω to -30 Ω. This results in the impedance angle remaining close to -90 ° throughout the frequency range. Such behaviour is referred to as capacitive, since it resembles the behaviour of a capacitor. The impedance magnitude of the QP10n transducer is significantly lower than in the case of the McWade transducer, whose impedance magnitude reaches several tens of thousands of ohms away from the resonance. This suggests that the transducer will allow a much higher current at a given drive voltage. Due to the large impedance angle, however, much of the resulting power will be reactive and will not be converted to mechanical vibration. This characteristic can be overcome by adding an inductor in series with the transducer to the drive circuit (Kim 2007). The use of the compensating inductance is described in 5.6.2.

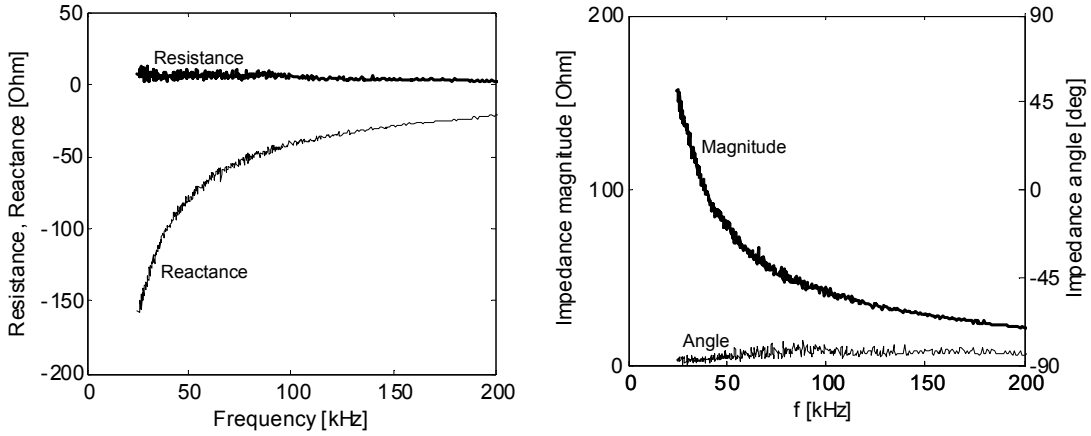

Figure 5.5. Electric impedance characteristics of the Quick Pack QP10n transducer S/N 11696.

MFC 8528-P1

The impedance characteristics of the MFC 8528-P1 transducer are shown in Figure 5.6. The characteristics are also capacitive, similar to those of the QP10n. Above 50 kHz the resistance component remains close to 10 Ω and the reactance component remains below 500 Ω. Below 50 kHz, however, both components increase sharply. While a high reactance can be compensated with the use of an inductor, a high resistance cannot. A resistance increase will therefore unavoidably lead to a reduction of the current, and consequently, power, which can be passed

through the transducer. This suggests that the MFC transducer will operate efficiently at frequencies higher than the QP10n – generally no less than 50 kHz.

Another marked difference between the two patch transducers is in the smoothness of their characteristics. The QP10n impedance curves are visibly jagged. This repeats consequently in all measurements. The MFC impedance curves are smooth. This suggests that QP10n will require a more precise tuning of the optimum operating frequency in order to make it operate at a local minimum of the impedance. The MFC will not require such precise tuning. The source of the jagged characteristics of the QP10n is unknown to the author. It can be speculated that the fact that it is built of a solid, rigid sheet of PZT introduces such behaviour through the influence of mechanical resonance of the sheet.

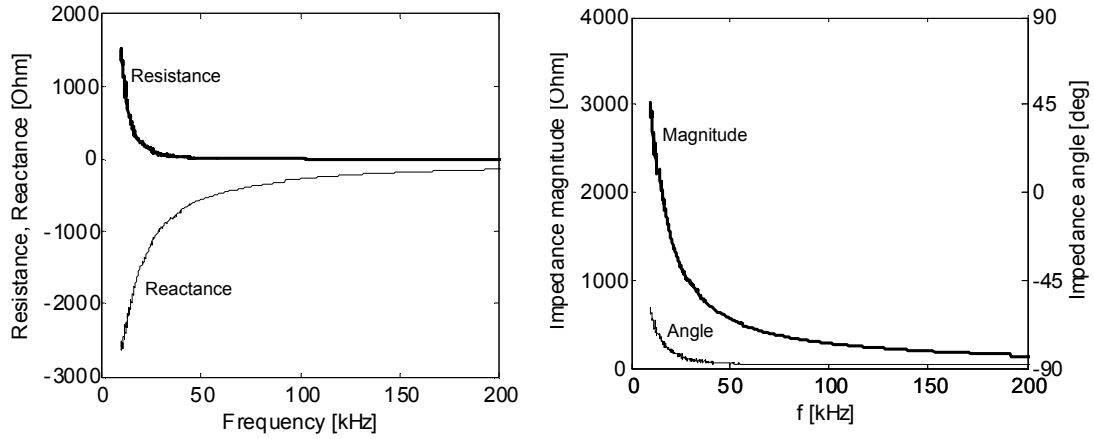

Figure 5.6. Electric impedance characteristics of the MFC M8528-P1 S/N 11A11-039I.

5.3. Inductive compensation

As noted above, the impedance characteristics of piezoelectric transducers are capacitive. The resistance component of a transducer's impedance is small compared to the absolute value of the reactance component. In accordance with Equations (4) - (6), when electric current is passed through a transmission transducer with such characteristics, the majority of the associated electric power is reactive. This means it remains in the electric circuit and is not dissipated in the form of mechanical vibration or heat. Only a small portion of the power passed through the transducer is resistive and is used, in part, for the generation of vibration. An analogous condition exists in the reception circuit. The majority of the electric power generated by the reception transducer is in the reactive form and is not absorbed by the load. Such a

situation, both in the transmission and the reception circuits, is also characterised by the phase shift between the voltage and the current waveforms approaching 90°.

The problem can be mitigated by placing a correctly matched inductor in series with the piezoelectric transducer. The reactance introduced by the inductor is of the opposite sign (positive) to the reactance introduced by the transducer (negative). The two reactances cancel out, resulting in an increase in the amount of the resistive power absorbed by the transmission transducer or the load connected to the reception circuit. The inductive reactance is calculated using the following formula:

$$X_L = 2 \cdot \pi \cdot f \cdot L \qquad (9)$$

where f is the AC frequency and L is the inductance. In order to achieve optimum compensation, the reactance of the inductor, X_L , must be equal (with opposite sign) to the capacitive reactance of the transducer, X_C.

Table 5.3 shows examples of compensating inductance values required to cancel the reactance of the MFC M8528-P1 transducer at several frequencies calculated using Equation (9). In further work a circuit simulation MATLAB code (described in section 5.4) was used to predict the influence of the compensating inductance value on the operating frequency and the power throughput of the transmission transducer. Frequencies used in Table 5.3 were chosen to match those predicted by computer simulation for several commercially available inductors, as shown in Table 5.6 in Section 5.6.2. The inductance values calculated using both methods are approximately the same.

Table 5.3. Examples of compensating inductance values calculated to match the capacitive reactance of the MFC M8528-P1. Frequencies chosen to match those predicted by computer simulation for commercially available inductors, as shown in Table 5.6

Frequency [kHz]	Transducer's capacitive reactance [Ω]	Required compensating inductance [mH]	Commercially available inductor used in simulation (Table 5.6) [mH]
97	-289	0.474	0.47
141	-199	0.224	0.22
170	-165	0.155	0.15
208	-135	0.103	0.1

The described process is referred to as impedance matching. Further information about various methods of impedance matching in relation to piezoelectric transducers is given in (Kim 2007) and (Lawry 2010).

The resistance of the inductors used was not taken into account in circuit simulations. This assumption appears founded for the 0.1 mH – 0.69 mH range inductors. Their resistances are in the range of 0.04 – 0.028 Ω respectively. The 1 mH inductor, however, had a resistance of 3.8 Ω. In hindsight, this resistance should have been taken into account in simulation, which would probably have reduced the simulation vs. experiment error with 1.22 mH compensating inductance, where the 1 mH inductor was used.

5.4. Electric circuit simulation tool

5.4.1. The transmission circuit

A MATLAB script was written to allow the calculation of the voltage, current and power in the transmission transducer and its drive circuit. The model used nominal values for the circuit components, with the exception of the piezoelectric transducer. The piezoelectric transducers were modelled using their previously measured impedance curves. The amplitude and frequency of the drive voltage was set by the user. This reflected the operation of the experimental setup, in which these parameters were set by the operator on the signal generator used to drive the circuit and constituted the input parameters of the overall energy system (see Figure 4.1). Thus, all input parameters necessary to model the operation of the transmission circuit were available. The simulation tool proved to be highly useful. Once validated against experimental results, it allowed prediction of the behaviour of various circuit configurations, including the use of different types of transducers and the effect of changing the values of the inductive compensation. Different routes of optimisation could be iteratively tested without the need to carry out time-consuming experiments.

The mathematical model used in the simulation script corresponded to the circuit diagram shown in Figure 4.4. A list of the input values is given in Table 5.4. The script was able to perform the calculation over a predefined range of frequencies and plot the results as a function of frequency.

Table 5.4. Input values of the transmission circuit simulation script

Symbol	Description	Typical value, source
E_{Tx_gen}	Signal generator voltage amplitude (electromotive force)	up to 20 Vpp (maximum setting available on the signal generator used in experimental work)
$\boldsymbol{Z}_{\boldsymbol{Tx\_gen}}$	Internal resistance of signal generator	50 + 0j Ω (from signal generator manual)
R_{Tx_sense}	Current sensing resistance	1 Ω
$\boldsymbol{Z}_{\boldsymbol{Tx\_piezo}}(f)$	Impedance of Tx piezo transducer	Measured beforehand, transducer and frequency dependent. Available as a data file used by simulation software.
X_{L_comp}	Compensating inductive reactance	Value adjusted to achieve desired operation characteristics of the circuit

The calculation performed by the script was as follows (an e-book by Kuphaldt (2007) was used as a reference for AC circuit theory):

In the first step the overall impedance of the circuit is calculated:

$$\boldsymbol{Z}_{\boldsymbol{Tx\_tot}} = \boldsymbol{Z}_{\boldsymbol{Tx\_gen}} + R_{Tx\_sense} + \boldsymbol{Z}_{\boldsymbol{Tx\_piezo}} + X_{L\_comp} \quad (10)$$

Subsequently, the current in the circuit is calculated:

$$\boldsymbol{I}_{\boldsymbol{Tx}} = E_{Tx\_gen} / \boldsymbol{Z}_{\boldsymbol{Tx\_tot}} \quad (11)$$

followed by voltage across the Tx piezoelectric transducer

$$\boldsymbol{V}_{\boldsymbol{Tx\_piezo}} = \boldsymbol{Z}_{\boldsymbol{Tx\_piezo}} \cdot \boldsymbol{I}_{\boldsymbol{Tx}} \quad (12)$$

The apparent (complex number) power can now be calculated.

$$\boldsymbol{S}_{\boldsymbol{Tx\_piezo}} = 1/8 \cdot \boldsymbol{V}_{\boldsymbol{Tx\_piezo}} \cdot \boldsymbol{I}^{*}_{\boldsymbol{Tx}} \quad (13)$$

where $\boldsymbol{I}^{*}_{\boldsymbol{Tx}}$ denotes a complex conjugate of $\boldsymbol{I}_{\boldsymbol{Tx}}$ and the 0.125 factor is used to account for the fact that both current and voltage are expressed as peak-to-peak values. Finally, the real power dissipated by the piezoelectric transducer can be calculated as the real part of the apparent power:

$$P_{Tx\_piezo} = \mathrm{Re}(\boldsymbol{S}_{\boldsymbol{Tx\_piezo}}) \quad (14)$$

5.4.2. The reception circuit

A MATLAB script simulating the operation of the reception electric circuit was also developed but found to be of only limited use. This was due to the fact that complete simulation tools for the generation, propagation and reception of the ultrasonic waves were not developed during the project. Thus, a gap existed in the chain of simulation models between the transmission and reception circuit (see Figure 4.1). Therefore the reception circuit model lacked input parameters which could be, by means of simulation, derived from the overall system's input parameters – the voltage and current settings of the signal generator.

The simulation script used the mathematical model and the MATLAB code written for the transmission circuit simulation. Minor modifications, such as the renaming of variables, were made.

5.5. Electric circuit measurement tool

A four channel digital oscilloscope (Agilent MSO6104A) and PC-based MATLAB data processing script was used to measure the voltage, current and power in the transmission and reception electric circuits. The oscilloscope was used to measure the following voltage waveforms:

- V_{Tx_1} - across the transmission transducer together with the current sensing resistor
- V_{Tx_sense} - across the current sensing resistor in the transmission circuit
- V_{Rx_load} - across the load resistor in the reception circuit

The waveforms recorded by the oscilloscope were transferred to a PC and processed using a MATLAB script. The script performed the following calculations:

For the transmission circuit:

In the first step, the amplitudes, phases and frequencies of the supplied voltage waveforms were determined. The phase of the voltage V_{Tx_1} was used as a reference for all other waveforms. The three measured voltages were then written in the complex number form. Subsequent calculations were performed in these values. The current in the circuit was calculated from the voltage across the current-sensing resistance R_{Tx_sense}:

$$I_{Tx} = V_{Tx\_sense} \cdot R_{Tx\_sense} \qquad (15)$$

The voltage across the transmission transducer was calculated:

$$\boldsymbol{V}_{\boldsymbol{Tx\_piezo}} = \boldsymbol{V}_{\boldsymbol{Tx\_1}} - \boldsymbol{V}_{\boldsymbol{Tx\_sense}} \quad (16)$$

Finally the apparent and real power values in the transmission transducer were calculated, as in the circuit simulation script, using Equations (13) and (14).

For the reception circuit

The waveform of the voltage across the known load resistor was measured. This waveform was converted into a complex number form with its phase set to zero. In this particular case all calculations applied to the load resistor, which was assumed not to introduce any voltage-current phase shift. Therefore, it would have been sufficient to perform calculations on real numbers. The complex number calculation was retained as it allowed code commonality with other scripts and ensures that the script can be expanded to include the calculation of values in other circuit elements.

In the first calculation step the current in the reception circuit was calculated:

$$\boldsymbol{I}_{\boldsymbol{Rx}} = \boldsymbol{V}_{\boldsymbol{Rx\_load}} / R_{Rx\_load} \quad (17)$$

subsequently the power delivered to the load resistor using equations analogous to Equations (13) and (14) was determined.

In a typical measurement the drive frequency was changed, in steps, multiple times in order to cover the entire investigated frequency range. The voltage waveforms were recorded at each frequency step. The data processing script was written to load all the recorded waveforms and perform calculations for all investigated frequencies. Finally, the calculated values were plotted against frequency.

During the development of the method the determination of the voltage-current phase shift angle in the transmission circuit proved to be challenging. The accuracy of the waveform phase measurement can be affected by non-ideal (capacitive or inductive) characteristics of the circuit elements, in particular the current-sensing resistor. The voltage-current shift introduced by the capacitive impedance characteristics of the piezoelectric transducers is close to 90 °. Therefore, even small angle measurement inaccuracies have a strong influence on the power calculation. Furthermore, these small inaccuracies can increase the phase shift angle beyond 90 °, resulting in the calculation of non-physical, negative power values. This problem was reported earlier by Bao *et al.* (2008). Such erroneous measurements were indeed recorded during the development of the method. The problem was eventually

mitigated by building the measurement circuit using dedicated printed circuit boards (PCBs) with a surface-mount current sensing resistor and with all connections realised only using BNC cables. All measurements presented in this thesis were made using this improved version of the measurement hardware.

Validation of the measurement system and results

In author's experience, the developed measurement system delivered repeatable results. Performing a statistical validation of the measurement system was considered, however, the need to provide a broad overview of the power transmission performance compensation led to the judgement that allocating the available time to testing multiple configurations of transducers and inductive compensation values was a priority. Results between configurations differed significantly and consistently. Therefore the author decided that testing the statistical significance of the measured differences was also of less priority.

5.6. Results

5.6.1. Initial circuit configuration

Three configurations of the energy transmission setup were initially tested. These comprised pairs of McWade, QP10n and MFC 8528-P1 transducers operated in circuits not comprising a compensating inductor. The input and output power was measured. In addition, the operation of the transmission circuit was simulated and the simulation result was compared with the measured result.

McWade NS3303

The results of the experiment and simulation for the McWade NS3303 are shown in Figure 5.7. The McWade transmission transducer draws meaningful amounts of power only near its resonance frequency. The measured input real power maximum of 153.5 mW was identified at 115 kHz in the tested unit. The circuit simulation closely matches the experimental result.

The reception transducer output power also reaches its maximum of 0.001 mW at 115 kHz. This corresponds to a transmission efficiency of only 0.0007 %. The output power consists of several very narrow peaks around this frequency. Subsequent findings indicate that the complicated shape of the reception power curves is a result of a combination of the electrical characteristics of both transducers combined with the Lamb wave generation, propagation and reception characteristics.

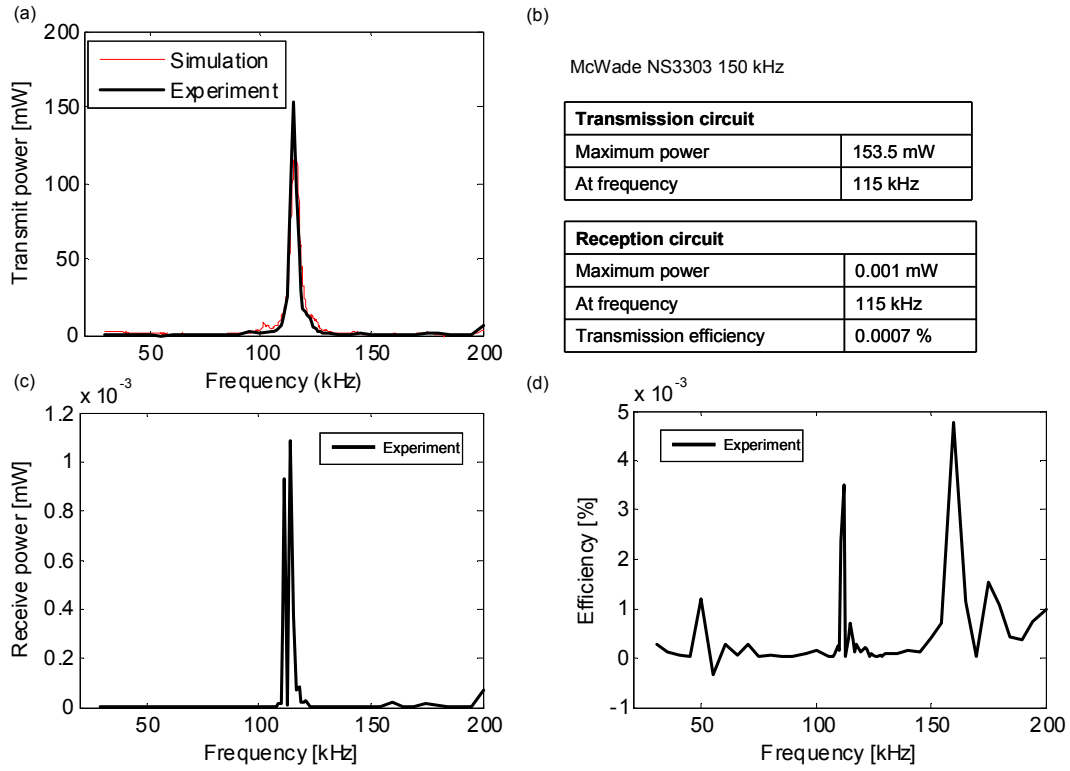

Figure 5.7. Measurement and simulation results of the energy transmission setup comprising two McWade NS3303 transducers in circuits without inductive compensation. (a) measured and simulated transmission input power vs. frequency, (b) summary of best performance figures, (c) measured reception output power vs. frequency, (d) energy transmission efficiency vs. frequency.

Quick Pack QP10n

The results of the Quick Pack QP10n experiment and simulation are shown in Figure 5.8. The measured transmission input power characteristic follows a curve composed of multiple peaks and troughs, mostly varying in the range between 40 and 80 mW over a major part of the tested frequency range. The maximum of 96 mW is reached at 89 kHz. The simulation curve follows a similar shape, falling in the same magnitude range, but reveals a significantly larger number of peaks positioned distributed at narrow intervals. This a shape follow the shape of the transducer impedance characteristic (affected by multiple small higher-order resonances, as mentioned earlier), on which the simulation is based. The discrepancy in the frequency of the peaks between the simulated and measured curves is caused by the fact that in the circuit measurement the frequency change and data capture was controlled manually and it was not practical to decrease the frequency step interval below 5 kHz. A second measurement was carried out over a narrow frequency range with a frequency step of 0.1 kHz. More peaks were indeed recorded. A discussion of the significance of this observation follows.

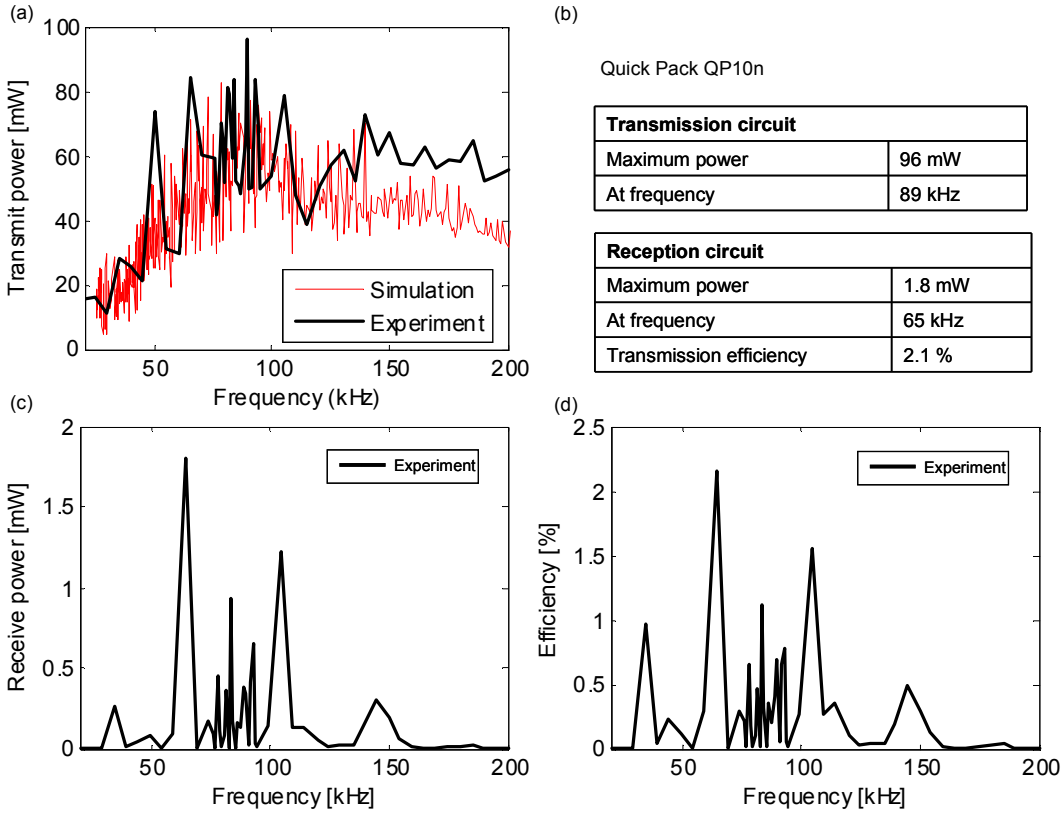

Figure 5.8. Measurement and simulation results of the energy transmission setup comprising two Quick Pack QP10n transducers in circuits without inductive compensation. (a) measured and simulated transmission input power vs. frequency, (b) summary of best performance figures, (c) measured reception output power vs. frequency, (d) energy transmission efficiency vs. frequency.

The reception transducer output power curve is also composed of multiple narrow peaks, mostly falling in the range between 50 and 100 kHz. The maximum of 1.8 mW was recorded at 65 kHz, corresponding to a transmission efficiency of 2.1%.

The measurement with the 0.1 kHz step was therefore carried out in the vicinity of the 65 kHz drive frequency. The transmission circuit results are shown in Figure 5.9 and the reception circuit results are shown in Figure 5.10. The measurement captured multiple peaks, some of them of significant magnitude. Based on this observation, the development of a fully automatic measurement system (e.g. based on a National Instruments LabView-controlled equipment) was considered. Such a system would allow the use of narrow frequency steps without the impractical measurement time increase occurring in the manually controlled system. The utility of such a development was, however, found questionable in the wider scope of the project. The reason for this decision was as follows. The existence of multiple narrow peaks of output power, separated by near-zero troughs, makes the operation

of a Quick Pack-based energy transmission system a complicated task. In addition to the small width of the peaks, the exact locations of these differ between the transducer examples. Thus, in order to achieve the optimum power transmission efficiency, the practical system would have to be equipped with a closed-loop control system which would tune the operating frequency. In the view of this, the identification of all individual power peaks in one particular realisation of the system, such as the experimental setup described here, makes little sense. It was therefore deemed reasonable to retain the manually controlled measurement system and use its results as a general indication of the performance which the Quick Pack transducers can deliver. Furthermore, measurements of the MFC 8528-P1-based setup showed that this transducer type delivers a significantly smoother power-frequency characteristic and may therefore be a more suitable candidate for the use in a practical system.

The discrepancy between the measured and simulated average input power magnitudes, which occurs particularly above 100 kHz (Figure 5.8 (a)), should also be discussed. It is believed that this is caused by the imperfect (inductive or capacitive) characteristics of the measurement circuit which influence the measurement result. This assumption could not, unfortunately, be fully confirmed. An attempt was made to characterise the circuit components using the VNA, but the results were inconclusive. This was due to the low impedance magnitudes of these components, which were below the range in which the VNA measures accurately (assumed by experienced operators with whom the author worked to begin at 20-30 kHz).

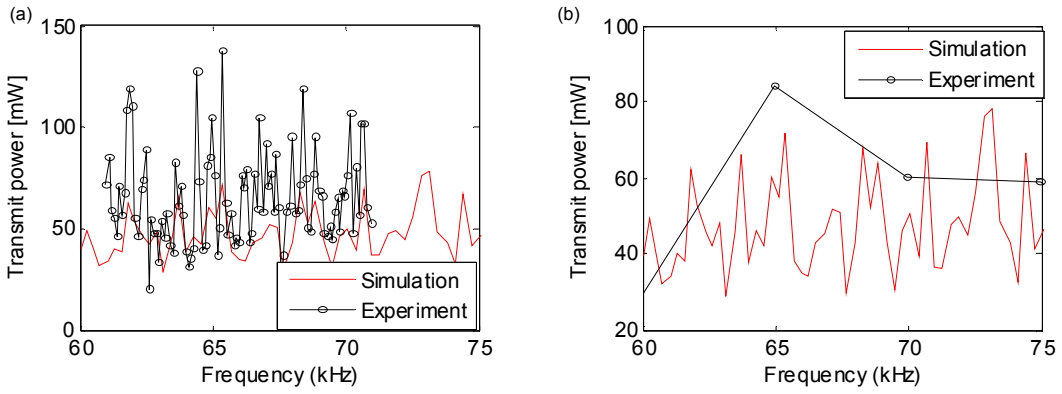

Figure 5.9. Comparison of two transmission input power measurements of the QP10n transducers. (a) with 0.1 kHz frequency steps, (b) with 5 kHz frequency steps.

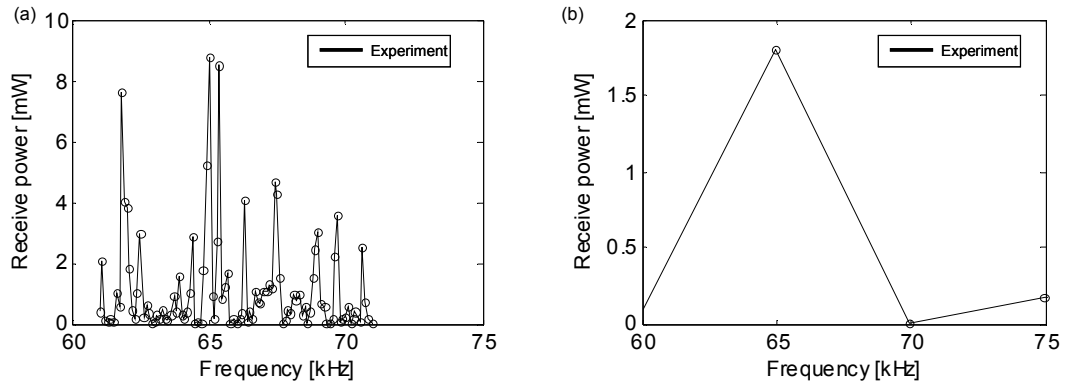

Figure 5.10. Comparison of two reception output power measurements of the QP10n transducers. (a) with 0.1 kHz frequency steps, (b) with 5 kHz frequency steps.

MFC 8528-P1

The results of the experiment and simulation for the MFC 8528-P1 are shown in Figure 5.11. The measured transmission input power follows, on average, the simulated curve. The measured curve contains periodic variations which, again, are believed to be artefacts caused by the imperfection of the measurement system components. The maximum power of 11.2 mW was recorded at 192 kHz. This value was recorded in one of the periodic peaks. A comparison with the simulated curve suggests that the input power-frequency characteristics is more likely to follow a steadily increasing curve and the maximum power should be found at the end of the investigate frequency range, i.e. at 200 kHz. The difference between the simulated and measured characteristics is approximately 10 %. In the light of subsequent experiments with the use of a compensating inductor (which increased the power throughput several times and removed the periodic artefacts), a further investigation of this simulation-experiment discrepancy was assumed to be of less importance.

The measured reception output power curve was found to increase steadily with frequency. The maximum was recorded at 200 kHz, corresponding to a 1.15 % efficiency. As mentioned before, the frequent peaks characteristic of the QP10n transducer were not found with the MFC 8528-P1 transducer.

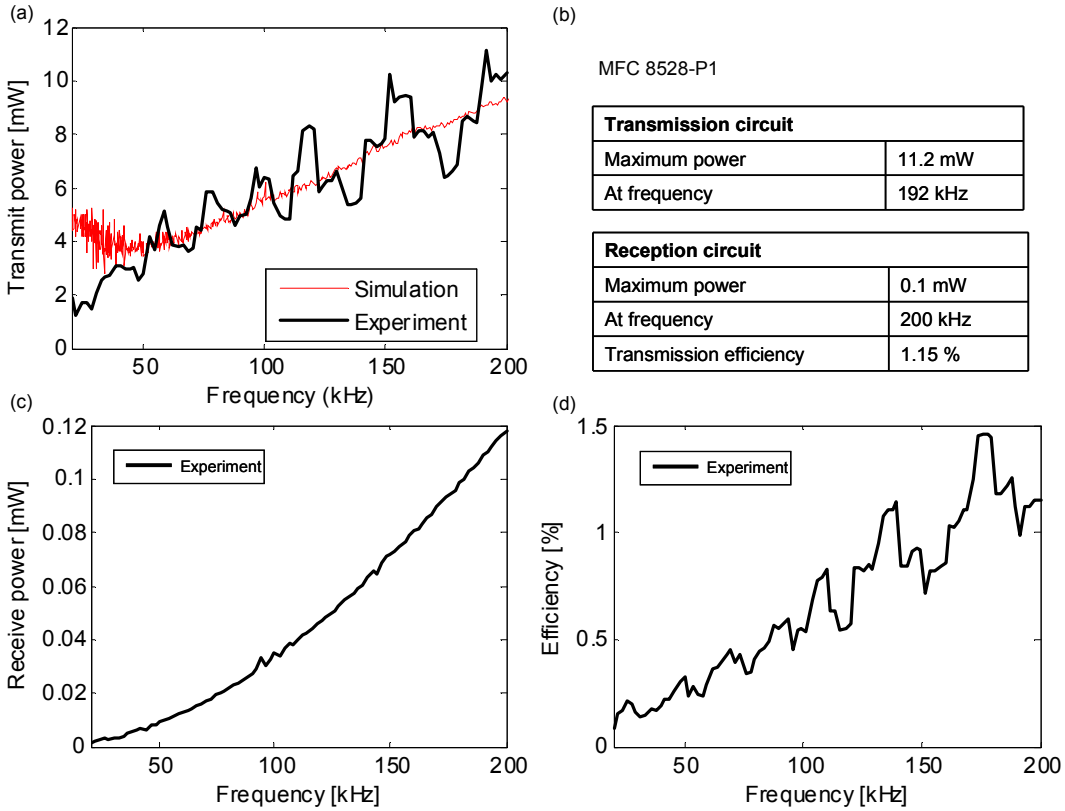

Figure 5.11. Measurement and simulation results of the energy transmission setup comprising two MFC 8528-P1 transducers in circuits without inductive compensation (a) measured and simulated transmission input power vs. frequency, (b) summary of best performance figures, (c) measured reception output power vs. frequency, (d) energy transmission efficiency vs. frequency.

5.6.2. Circuit with inductive compensation

In a subsequent series of measurements the influence of using compensating inductors in the transmission and reception circuits was investigated. The transmission circuit simulation MATLAB script was used in order to estimate the required inductance values. The script was modified to run in a loop, performing a series of simulations across a predefined inductance range. The maximum input power values were identified and plotted against the inductance values. The frequencies at which these maximum values occurred were also recorded.

For the experimental work several commercially available inductors, with inductance values in the range identified by the simulations, were obtained. Input and output power measurements were performed.

Only the two patch transducer types – QP10n and MFC 8528-P1 were chosen for the work with inductive compensation. The McWade NS3303 was previously shown to deliver the power throughput three orders of magnitude smaller than the patch

transducers and to operate only within a narrow frequency range near the resonance. Therefore the McWade transducer was not further investigated.

Quick Pack QP10n

A simulation of the influence of inductive compensation on the transmission transducer input power for the Quick Pack QP10n was carried out. Results are shown in Figure 5.12 (a). Based on the simulation results, the following commercially available compensating inductors were chosen for experimental measurement: 0.15 mH, 0.22 mH, 0.69 mH, 1.22 mH. In each experiment inductors of the equal values were placed both in the transmission and in the reception circuits.

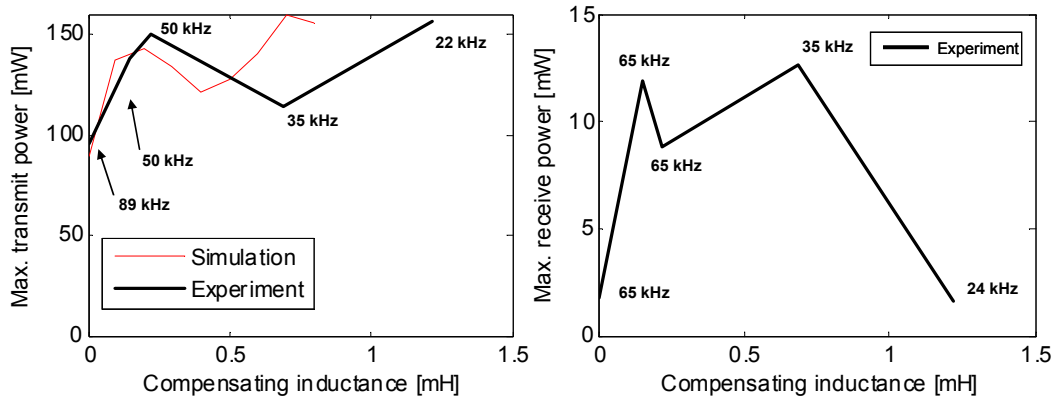

Figure 5.12. Influence of inductive compensation on (a) transmission transducer input and (b) reception transducer output power in setup with QP10n transducers.

The results of the experimental measurements of both transmission and reception circuits are presented in Figure 5.12. They are also summarised in Table 5.5 for easier numerical comparison.

In the transmission circuit the input power was expected to peak at 0.22 mH and 0.69 mH according to the simulation. (The appearance of two peaks is understood to be a result of the jagged resistance and reactance characteristics of the Quick Pack transducer again combined with the frequency step of the vector network analyzer used to measure the transducer characteristics (approximately 100 Hz) and the inductance step size used in the simulation shown in Figure 5.12 (0.1 mH). In hindsight, at least the latter could have been improved. This, however, would have had limited practical significance, since the impedance values of stock inductors used in experiment were separated by at least 0.1 mH.)

The simulation result was confirmed in the experiment at 0.22 mH. However at 0.69 mH the measured power was approximately 30 % lower than the predicted value. It is believed that this discrepancy was caused by the character of the power vs. frequency characteristics of the Quick Pack-based circuit combined with the measurement limitations. The power vs. frequency curves are composed of multiple narrow peaks separated by deep troughs. The power measurement was conducted with 1 kHz steps. (Such a step size was used throughout the project as a compromise between the measurement duration and resolution. It is advisable to develop a fully automatic frequency scan setup which will allow a significant increase of the resolution for further work, especially with Quick Pack transducers.) This could have led to a narrow power peak not being recorded in the measurement (see Figure 5.13 (c)).

Another measured input peak occurred at 1.22 mH and a frequency of 22 kHz. This peak occurred below the frequency range covered by the simulation, which started from 25 kHz.

The measured reception output power reached peaks of 10.2 mW at 0.15 mH and 11.2 mW at 0.69 mH. These values corresponded to a 4.9 and 5.3 times increase in comparison to a circuit without inductive compensation.

Table 5.5. Summary of inductive compensation simulation and measurement results in setup with QP10n transducers

	Compensating inductance [mH] →	**0**	**0.15**	**0.22**	**0.69**	**1.22**
1	Simulated maximum transmission input power [mW]	89	132	143	158	103
2	At frequency [kHz]	89	65	54	29	26
3	Measured maximum transmission input power [mW]	96	138	150	114	156
4	At frequency [kHz]	89	50	50	35	22
5	Measured maximum reception output power [mW]	1.8	11.9	8.8	12.7	1.6
6	At frequency [kHz]	65	65	65	35	24
7	with efficiency [%]	2.1	10.3	7.6	11.2	1.2
8	Reception output power improvement factor with respect to circuit without compensation	n/a	4.9	3.6	5.3	0.6

The use of inductive compensation altered the shapes of the power vs. frequency characteristics of both transmission and reception circuits. With an increasing inductance value, the maximum transmission input power frequency decreased. The input power peak also became narrower (Figure 5.13 and Table 5.5 row 4). Similarly, the reception output power peaks became narrower and occurred at decreasing frequencies (Figure 5.14 and Table 5.5 row 6).

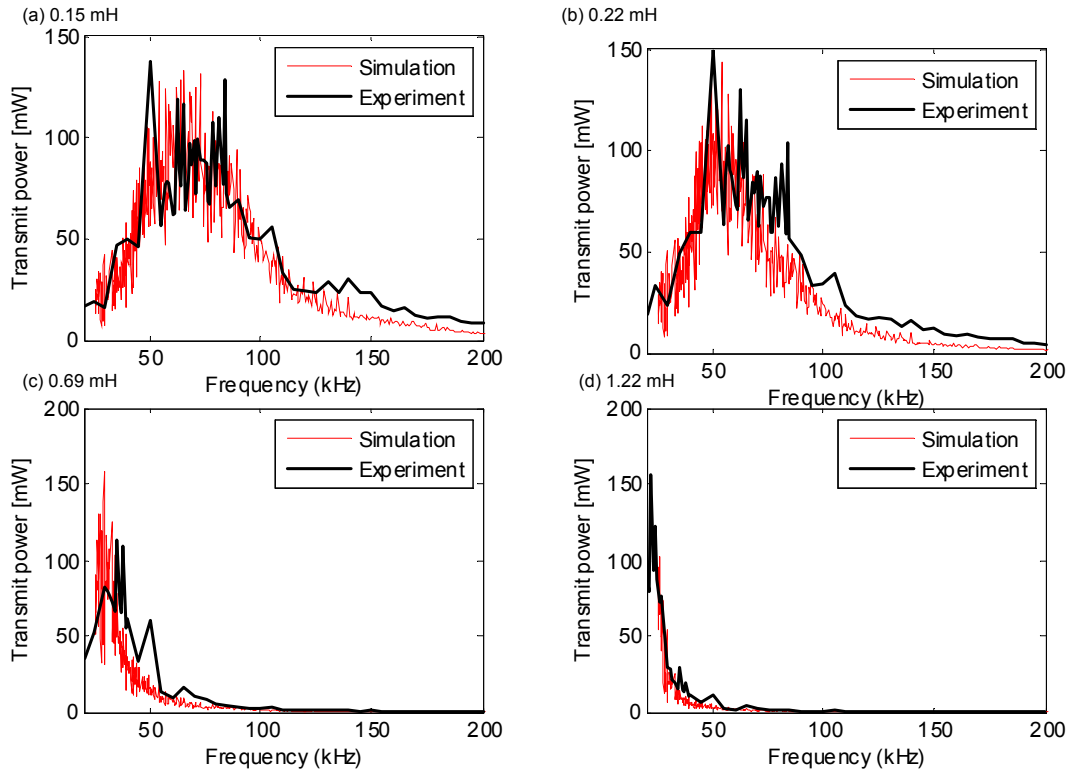

Figure 5.13. Input power vs. frequency curves of transmission circuit with QP10n transducer and various inductive compensation values.

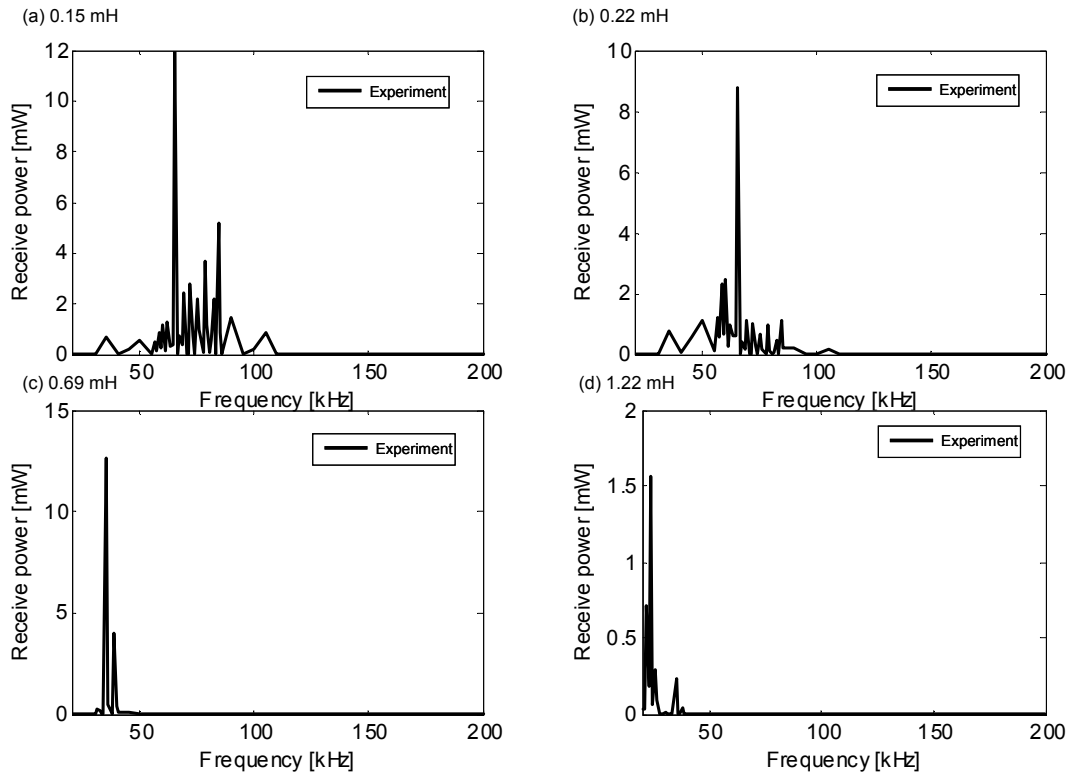

Figure 5.14. Output power vs. frequency curves of reception circuit with QP10n transducer and various inductive compensation values.

MFC 8528-P1

The results of transmission circuit inductive compensation simulation for MFC 8528-P1 are shown in Figure 5.15 (a). The simulation showed that the increase of the inductance value up to 4 mH will result in a continuing increase of the transmission input power. With no inductive compensation a transmission power maximum was predicted at 547 kHz (Table 5.6), which was significantly higher than the previously considered range of up to 200 kHz. The use of 0.1 mH or higher inductive compensation decreased the frequency of maximum transmission power to 208 kHz and less.

The simulation results indicated two obstacles expected in the experimental measurements. First, the Agilent 33220A signal generator used to drive the experimental setup has a maximum output power rating of 100 mW. In experiments with the Quick Pack transducers power values up to 150 mW were measured. This showed that the signal generator was able to supply higher than nominal power. In the case of the simulated MFC-based circuit behaviour, however, the maximum expected input power reached 250 mW. In this case it was unlikely that the signal generator available to the author will be able to supply the required amount of power.

The second indicated obstacle was that at inductance values of 0.1 mH and above the predicted voltage across the transmission transducer exceeded 40 V (Figure 5.16), which was the limit of the Agilent MSO6104A oscilloscope used. Thus, the transmission power measurement would become impossible at higher compensating inductance values. A voltage divider was made on a dedicated circuit board with surface mounted resistors and was tested to limit the voltage reaching the oscilloscope. It was found, however, to produce voltage values which were far from those predicted by calculation. The effect was assumed to be caused by unknown reactive characteristics of the circuit, which at the frequencies used in the experiment proved to significantly influence the divider's operation.

(In hindsight the simplest solution to the above problems would have been to reduce the driving voltage amplitude. The behaviour of the system was linear with respect to the drive voltage, which was proven in *ad hoc* measurements. Therefore the measurements collected with a lower drive voltage could have been scaled in order to be made comparable to those of other transducers made at the 20 V drive voltage.)

Taking these limitations into consideration, measurements with inductances up to 0.69 mH were tested experimentally. This allowed comparison with the previously tested Quick Pack transducers under the same drive conditions. The measurement frequency range was limited to 230 kHz at 0.1 mH (due to the predicted power peak at 208 kHz) and to 200 kHz at all other frequencies. At 0 mH it was considered not necessary to expand the measurement range in order to cover the predicted power peak at 547 kHz. This decision was made based on the observation that the peak transmission power was predicted to be 16.5 mW (Table 5.6), significantly less than peak values predicted for higher compensating inductance values. Therefore, the measurement at 0 mH was considered of less importance for the improvement of the energy transmission system performance.

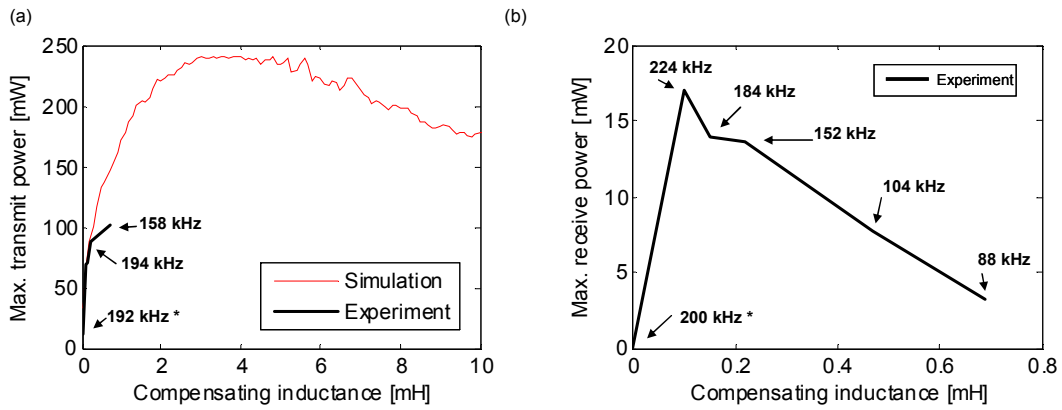

Figure 5.15. Influence of inductive compensation on (a) transmission transducer input and (b) experimentally recorded reception transducer output power in setup with MFC 8528-P1 transducers. Drive voltage amplitude 20 Vpp. (* measurement conducted up to 200 kHz).

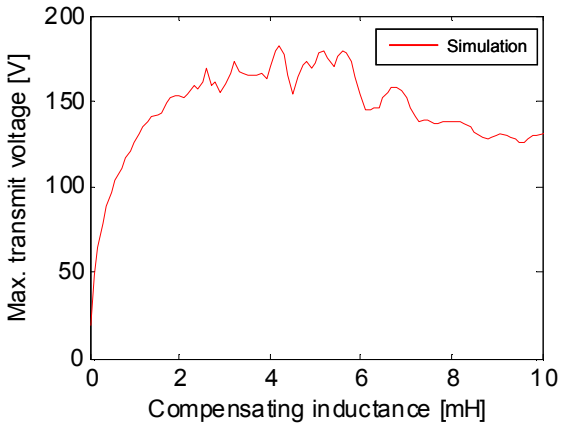

Figure 5.16. Influence of inductive compensation on the maximum voltage across the transmission transducer (simulated curve).

The oscilloscope 40 V voltage limit was reached at 0.15 mH. Beyond this value the measurement of maximum input power values was not possible. The reception transducer output power reached a maximum of 17 mW at 0.1 mH, corresponding to 64 % efficiency (Table 5.6). Above the 0.1 mH inductance the output power steadily decreases. This took place despite the continuing increase of the input power at higher inductance values. It is believed that this effect is caused by the decrease in the efficiency of Lamb wave generation and reception at lower frequencies dictated by the use of inductive compensation.

Table 5.6. Summary of inductive compensation simulation and measurement results in setup with MFC 8528-P1 transducer. N/d (no data) are characteristics of the transmission circuit which were not recorder as the measured voltage exceeded the 40 V limit of the oscilloscope. Note that measurements of the reception circuit were still carried out for these data points, since the voltages measured in this circuit were within the oscilloscope's range. (* indicates measurements conducted in the frequency range up to 200 kHz)

	Compensating inductance [mH] →	**0**	**0.1**	**0.15**	**0.22**	**0.47**	**0.69**
1	Simulated maximum transmission input power [mW]	16.4	69	75	94	135	149
2	At frequency [kHz]	547	208	170	141	97	80
3	Measured maximum transmission input power [mW]	11.2*	69	70	*n/d*	*n/d*	*n/d*
4	At frequency [kHz]	192*	194	158	*n/d*	*n/d*	*n/d*
5	Measured maximum reception output power [mW]	0.1*	17	14	13.6	7.7	3.2
6	At frequency [kHz]	200*	224	183	152	104	88
7	with efficiency [%]	1.2	64	57	*n/d*	*n/d*	*n/d*
8	Reception output power improvement factor with respect to circuit without compensation	*n/a*	170	140	136	77	32

It is important to note that while the measured output power values can be treated with a good level of confidence, the calculated power transmission efficiency should be treated with caution. The measurement of the input power, even with improved PCB-based hardware, often delivered results which were a good match with the simulation. It is expected that the voltage-current angle measurement in particular remained the source of a limited error. The power transmission efficiency values are calculated in relation to the input power. Since the power measurement is expected to contain a small, but not quantified error, the efficiency values are also expected to contain some inaccuracy.

The use of inductive compensation decreases the frequency at which the maximum input power occurs and makes the power peak narrower (Figure 5.17). With MFCs the effect is, however, much less pronounced than with Quick Pack transducers. A similar effect occurs in the case of the reception output power curves (Figure 5.18).

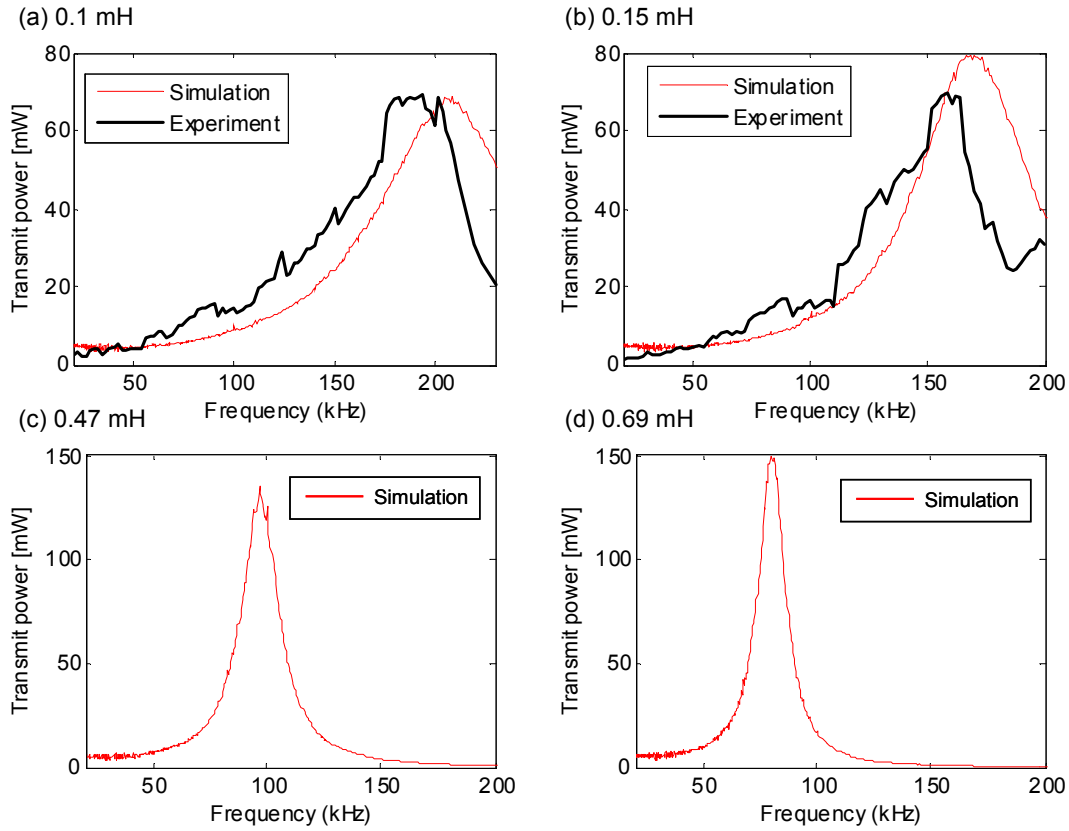

Figure 5.17. Input power vs. frequency curves of transmission circuit with MFC 8528-P1 transducer and various inductive compensation values. (a) simulated and experimental curves for 0.1 mH inductive compensation (b) simulated and experimental curves for 0.15 mH inductive compensation (c) simulated curve for 0.47 mH inductive compensation (d) simulated curve for 0.69 mH inductive compensation.

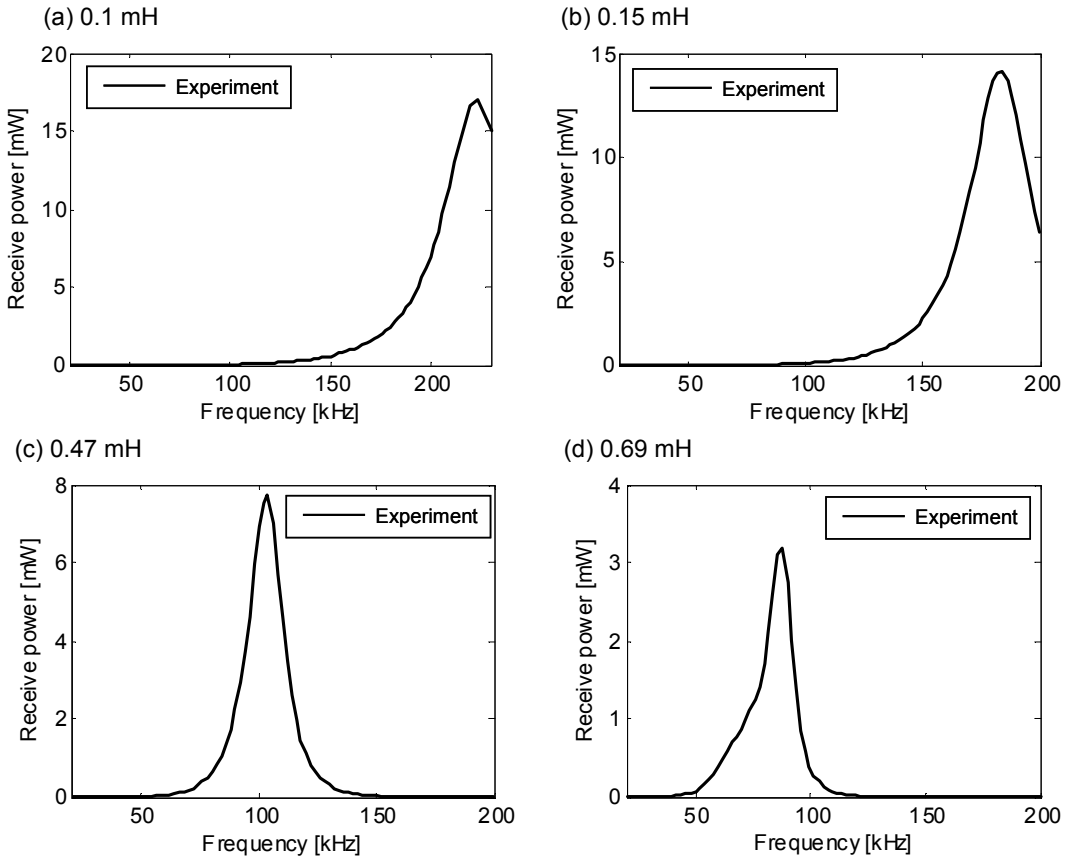

Figure 5.18. Output power vs. frequency curves of reception circuit with MFC 8528-P1 transducer and various inductive compensation values: (a) 0.1 mH, (b) 0.15 mH, (c) 0.47 mH, (d) 0.69 mH.

5.7. Summary and discussion

The electrical operation of the experimental ultrasonic Lamb wave energy transmission system was evaluated. Three configurations, using three different piezoelectric transducer types, were compared. The impedance characteristics of the transducers were measured. A circuit computer simulation tool was written and used to predict the operation of the transmission electric circuit, aiding the selection of cases designated for experimental evaluation. An input and output power measurement system was built and a corresponding data processing script was written. Finally, the optimisation of the energy transmission electric circuits with the use of compensating inductors was evaluated, indicating a significant performance improvement.

The electric impedance characteristics of all three evaluated transducer types were found to be highly capacitive. Otherwise the transducer types were found to differ significantly from one another:

- The McWade NS3303 150 kHz is made of a bulk crystal of PZT with a resonance at 117 kHz. The impedance of the transducer is low only within a narrow range around the resonance frequency. Away from the resonance the impedance increases rapidly. Thus, the transducer can operate efficiently as a transmitter and receiver of energy only within the narrow frequency range near the resonance
- The Quick Pack QP10n transducer is made of a thin sheet of PZT. Its impedance-frequency curve does not contain a single resonance peak. Instead, the favourable low-impedance range is spread across the entire tested frequency range of 20 to 200 kHz. The transducer can be operated efficiently within a range of frequencies significantly larger than the McWade. An unfavourable characteristic of the Quick Pack however, is that its impedance-frequency curve contains multiple, frequently distributed local peaks. This indicates that an energy transmission system using the Quick Pack transducer will have to be precisely tuned to operate within one of these peaks in order to achieve optimum performance. Such tuning will involve both a precise setting of the operating frequency and the selection of transmission and reception transducer units with overlapping characteristics, which may be problematic due to the transducer manufacturing inaccuracies.

- The MFC 8528-P1 transducer is built of multiple thin PZT fibres aligned along its longitudinal direction. The transducer is flexible, which makes it easier to handle and allows it to be bonded to curved surfaces. The impedance characteristics of this transducer are similar to those of the Quick Pack. The favourable impedance range extends upwards of 50 kHz. In addition, the impedance-frequency curves of the MFC are much smoother than those of the Quick Pack, indicating that it will not require similar frequency fine-tuning in order to operate optimally.

The performance of the energy transducer setups using each of the three transducers was first compared in circuits without inductive compensation using a 20 Vpp AC drive signal across a 20 – 200 kHz frequency range. The results are as follows:

- The system using the McWade transducer transmitted measurable amounts of power only within approximately ± 1 kHz of the 115 kHz optimum frequency. (The minor frequency difference in comparison to the 117 kHz transducer resonance frequency may have been caused by the impedances of other circuit components as well as a measurement error). The maximum transmitted power was 0.001 mW, corresponding to 0.0007 % efficiency.
- The system using the Quick Pack transducer transmitted significantly higher amounts of power within several peaks, each several kHz wide, distributed in the 50 – 100 kHz range. The optimum performance was achieved at 65 kHz, with 1.8 mW transmitted power and 2.1 % efficiency. The narrow shape of the power transmission peaks indicated that frequency fine tuning is necessary in order to achieve satisfactory power throughput.
- The power throughput curve of the MFC based system increased steadily with the increase of the frequency. The optimum performance was achieved at 200 kHz, with 0.1 mW power throughput and 1.15 % efficiency. Thanks to the smoothness of the power-frequency curve even large changes in operating frequency did not result in a large performance decrease. This indicated that the MFC based system does not require fine frequency tuning and is therefore the easiest to operate efficiently.

The above comparison showed a significant – three orders of magnitude – power throughtput advantage for the Quick Pack and MFC transducers over the McWade transducer. Therefore the McWade transducer was not selected for further

investigation. Of the two selected transducers, the Quick Pack transmitted a higher amount of power, but its performance was composed of multiple narrow peaks, which indicated a difficulty in optimum frequency tuning and a high sensitivity to tuning errors. The MFC transmitted a smaller amount of power, but its smooth power-frequency characteristic indicated easy frequency tuning and robustness against tuning errors.

Further investigation of the two selected setups was conducted with the use of compensating inductors in both the transmission and the reception electric circuits. The inductors were used to cancel the capacitive characteristics of the piezoelectric transducers. As expected, the use of inductive compensation significantly improved the power transmission performance. Specifically:

- The Quick Pack-based system achieved optimum performance with a 0.69 mH inductor. The power throughput reached 12.7 mW, which was a 5.3 times improvement over the system without compensation. The corresponding power transmission efficiency was 11.2 %. The optimum operating frequency decreased to 35 kHz. A second power transmission peak occurred with a 0.1 mH inductor. The power transmission was 11.9 mH with 10.3 % efficiency at 65 kHz. A significant disadvantage of the use of compensating inductance was the narrowing of the power transmission peak frequency ranges. With both aforementioned values these peaks were less than 1 kHz wide, resulting in a further increase of the tuning difficulty.
- The MFC-based system achieved optimum performance with a 0.1 mH inductor. The power throughput increased to 17 mW, which was a 170 times improvement over the uncompensated system. The corresponding transmission efficiency was 64 %, at the optimum operating frequency 224 kHz. A further increase of the compensating inductance up to 0.22 mH caused a slow power throughput decrease down to 13.6 mW. At the same time the optimum operating frequency was steadily decreased to 152 kHz. This indicated that with the MFC transducer the inductive compensation can be used to adjust the operating frequency without a significant loss of performance. Such a characteristic can be useful in accounting for other design considerations in a practical system. The maximum power transmission peaks observed with inductive compensation were also relatively wide. At 0.1 mH a 50 % decrease of the power throughput occurred 20

kHz away from the optimum frequency. This indicates an ease of tuning even with the use of inductive compensation.

The comparison of setups with inductive compensation revealed advantages of the MFC transducer over the Quick Pack transducer. With the same drive signal amplitude, the MFC setup transmits 1.3 times more power. Its optimum frequency ranges are also significantly wider than those of the Quick Pack-base system. Nevertheless, the performance of the Quick Pack-based system is still good. Therefore, both transducer types were retained for further investigation.

It is understood that the frequency at which the optimum electrical performance of a transducer is achieved is typically not the same as the frequency at which the efficiency of Lamb wave generation is the best (i.e. the dimensions of the transducer are correctly matched to the Lamb wave wavelength). The optimum performance frequencies identified during the project should be regarded as those at which the best compromise between the electrical and the acoustical efficiency is achieved.

5.8. Conclusion

In this chapter the electrical performance measurement and simulation of the prototype ultrasonic Lamb wave energy transmission system was described. Based on the results of this work, optimally performing transducer types and the corresponding optimum values of the electrical inductive compensations were chosen. The selected transducer types were the Quick Pack QP10n and the MFC M8528-P1. The optimum inductive compensation ranges were found to be: 0.1 – 0.69 mH for the Quick Pack and 0.1 – 0.22 mH for the MFC.

Chapter 6. Lamb wave generation, propagation and reception

6.1. Introduction

In this chapter the behaviour of the ultrasonic Lamb wave signal in the power transmission system is described. The information presented is based on measurements carried out using a scanning laser vibrometer. The emission characteristics of the transmit transducers, the propagation of the ultrasonic signal in the aluminium plate and the operation of the receive transducers are discussed. The chapter builds on the knowledge of the electrical performance of the system presented in the preceding section. The electrical characteristics of the transmission and reception circuits are related to the corresponding characteristics of the ultrasonic signal propagating between the transducers. In this way, a complete picture of the ultrasonic power transmission is built.

6.2. Laser vibrometry

The out-of-plane mechanical vibration of the plate and the transducers due to the passing of ultrasonic Lamb waves was mapped using a Polytec PSV-400 1-D scanning laser vibrometer. The vibrometer uses the Doppler effect to detect the movement of a point on a surface at which its laser beam is directed. The set-up used in this work comprised one laser head. This allowed the detection of the out-of-plane movement of the plate surface. The laser head was of a scanning type, employing a moveable mirror, thus allowing the device to change the direction of the laser beam and scan a user-defined area of the plate. A three-dimensional set-up, comprising two or three laser heads, is also offered by the manufacturer but. This allows the detection of both out-of-plane and in-plane movements. Such a setup, however, was not available to the author. The laser vibrometer is equipped with dedicated PC software facilitating the control of the scan as well as the processing of the acquired data. Two basic types of operation are available. The Fast Fourier Transform (FFT) mode performs a Fourier transform of the acquired data. From this type of measurement, one can obtain information about velocity and displacement amplitudes of the measured vibration pattern. The advantage of this mode is that the FFT processing is carried out by the software, reducing the analysis workload for the user.

The time domain scan mode records a waveform of the measured vibration at each point of the scan. The duration of the recording is defined by the user. For a single measurement point recording durations of up to several hundred milliseconds are practical. The laser beam can be directed and performs a measurement at only one point at a time. Thus, in order to obtain a time-synchronised scan of a larger area, the same vibration input (e.g. a Lamb wave burst) must be repeated for each scan point and the vibrometer measurement triggered at the same instant of each repetition, achieved via synchronised triggering from the vibration driving signal. The data processing software for the time domain mode allows the data to be presented in the following forms: video files showing the propagation of vibration in the entire scan area, a waveform presentation at a single scan point, and snapshots of out-of-plane velocity scans in the entire scan area at a chosen time. In the work carried out by the author the duration area time scans never exceeded 200 μs. Such a duration was sufficient to image the passage of several wave fronts over an area surrounding a piezoelectric transducer.

6.3. Transmission transducer: imaging of pulsed operation

In order to gain an initial insight into the operation of the Transmission transducers, time domain scans of the areas surrounding the transducers were performed. The transducers were excited with a five-cycle pulse at 20 Vpp, using a circuit with a 0.15 mH inductor. It should be noted that in the power transmission application the transmitting transducer is operated continuously and not in pulses. Thus, the pulsed operation described in this section is a departure from the intended mode. The use of a pulsed mode is necessary however in order to make it possible to distinguish signals associated with individual Lamb wave modes.

MFC M8528-P1

The MFC M8528-P1 transducer was operated at 181 kHz. (At the time of the measurement this frequency was thought to provide the highest power throughput. Following subsequent measurements the optimum frequency was revised to 180 kHz. In the case of the MFC, which has a smooth frequency-impedance characteristic, the 1 kHz difference between this and subsequent measurements is not significant.) Figure 6.1 shows a snapshot from the video made from this measurement. The following features can be observed:

- Waves with an 8 mm wavelength and amplitude ~ 200 μm/s. These correspond to the A_0 mode at 181 kHz. The A_0 wavelength is many times shorter than the length of the transducer. While the transducer is driven to expand and contract uniformly along its entire length under the electric signal, the five-cycle pulse is long enough for an 8 mm wave pattern to establish itself within the transducer length. The A_0 waves are radiated in a narrow beam along the longitudinal axis of the transducer.
- Waves with a ~35 mm wavelength and amplitude of less than 50 μm/s. These, with less confidence, can be interpreted as the S_0 mode at 181 kHz, which should have a wavelength of 30 mm at 181 kHz.

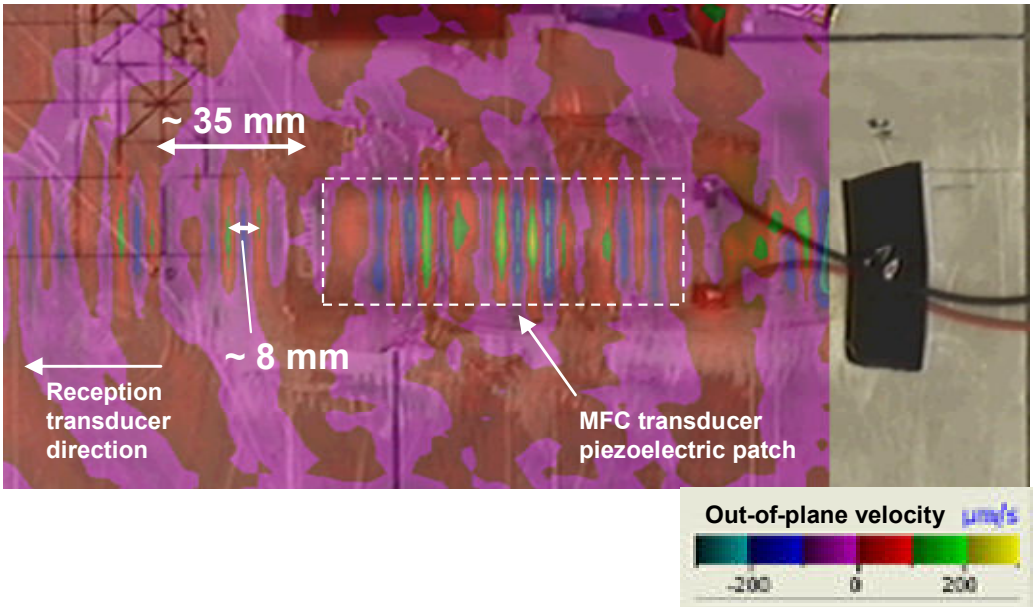

Figure 6.1. A snapshot of the MFC M8528-P1 transducer emitting a five-cycle pulse at 181 kHz.

QP10n

The Quick Pack QP10n transducer was operated at 65 kHz. Figure 6.2 shows a snapshot from the video made from this measurement. The following features can be observed:

- Waves with a ~16 mm wavelength and an amplitude of ~1 mm/s are radiated along the longitudinal axis of the transducer. These can be interpreted as the A_0 mode at 65 kHz.
- Similar A_0 mode waves are also radiated from the transducer's longer edges, along its transverse axis.

The difference between the operation of the MFC transducer, radiating a single beam along its longitudinal axis, and the QP10n transducer, radiating along both of its dimensions, can be linked to the principles of operation of these transducer types. The MFC, employing the d_{33} piezoelectric coupling, expands and contracts only along its longitudinal axis (Pretorius 2004) and thus sends a Lamb wave beam in only one direction. The QP, employing the d_{31} and d_{32} piezoelectric coupling (Pretorius 2004), expands and contracts along both of its axes and thus sends Lamb wave beams in two perpendicular directions.

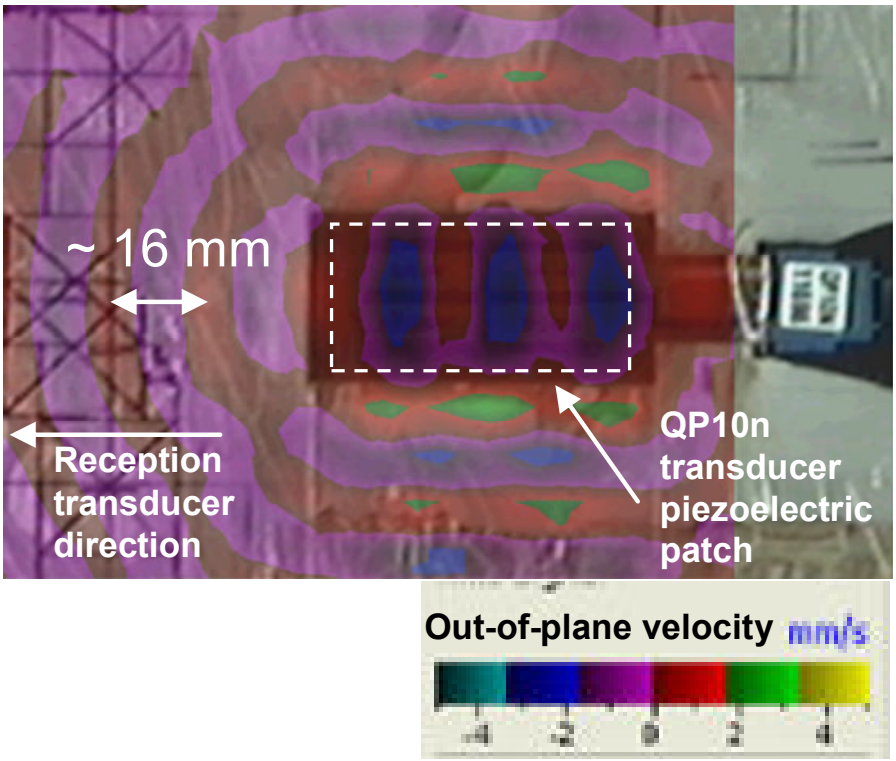

Figure 6.2. A snapshot of the QP10n transducer emitting a five-cycle pulse at 65 kHz.

6.4. Transmission transducer: quantitative characterisation

6.4.1. Methodology

The videos discussed in the preceding section provided a good qualitative overview of the Transmission transducers' operation. Further measurements were made in order to quantify the transmission characteristics of the transducers. In these measurements the transducers were again excited with five-cycle pulses. At predefined scan points waveforms of the passing Lamb wave signal were recorded by the vibrometer. The MFC transducer was tested in the 150 – 190 kHz frequency

range and the Quick Pack transducer was tested in the 55 – 75 kHz frequency range. In these ranges the highest energy transmission was previously observed and therefore they were chosen as the most valuable for further investigation.

Waveform identification

Based on the known time-of-flight from the transducer to the scan point, waveforms corresponding to the A_0 and S_0 modes were identified, as shown in Figure 6.3. The amplitudes of these waveforms were then read.

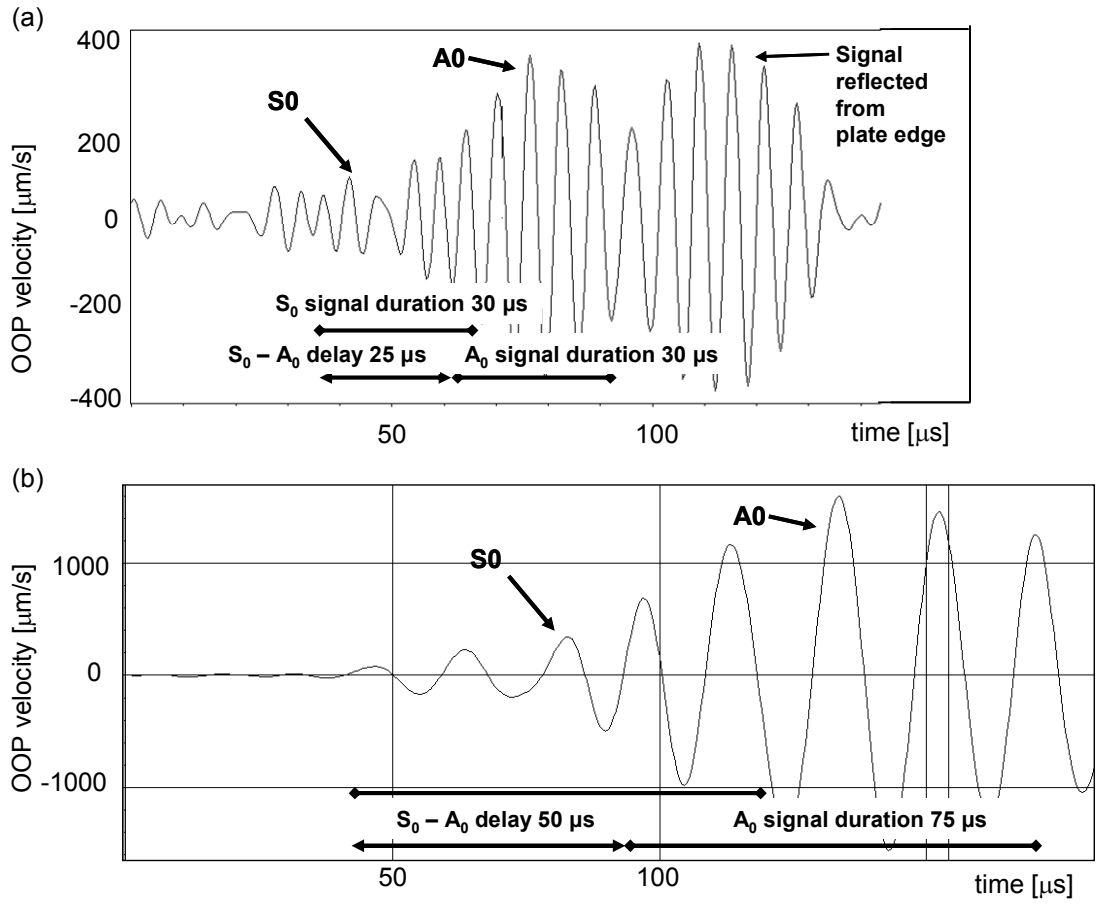

Figure 6.3. Examples of waveforms obtained at one of the radial characteristic scan points (scan point 1, see Figure 6.4). (a) MFC transducer at 160 kHz, (b) Quick Pack transducer at 55 kHz. Signal durations and identification of S_0 and A_0 mode waveforms are shown.

The identification of waveforms was not straightforward and the accuracy of their amplitude measurement was decreased due to several factors. Firstly, the S_0 and A_0 modes overlapped to some extent (see Figure 6.3). Therefore care had to be taken to record the amplitude of each mode in an area not affected by the other. Secondly, the recorded time of arrival was affected (with respect to the prediction based on the propagation velocity) by the accuracy of the vibrometer measurement trigger

(realised by supplying the electric drive signal to the trigger port of the vibrometer) and the assumption of the exact location from which the Lamb wave signals originated, which affected the distance of propagation. The latter was somewhat aided by an analysis of videos of the transducer operation recorded with the scanning laser vibrometer. Thirdly, in the case of the MFC transducer generating a lower-amplitude signal, the S_0 mode signal was barely visible above the noise level.

The differences between measurement results were not tested statistically due to the limited time available. Therefore, whenever applicable, the possibility of measurement error having a significant influence on results is explicitly mentioned.

Measurement series

Two series of measurements of the transmission transducer pulsed operation were performed. These experiments will be referred to as "Measurement A" and "Measurement B". These measurements differed in the choice of variables selected from: the location of scan points, drive voltage, inductive compensation and frequency. The experiments were carried two months apart, giving information about the repeatability of this measurement method.

Measurement A

- Sixteen scan points distributed every 22.5º on a 150 mm radius circle were defined around each Transmission transducer (Figure 6.4). The points were numbered 1 to 16, where 1 faced the Reception transducer.
- The drive voltage amplitude was 20 Vpp.
- The inductive compensations were 0 mH and 0.15 mH. The latter value was chosen because it belonged to the optimum inductance ranges of both MFC and Quick Pack transducers.
- The frequencies were: 150, 160, 170, 180, 190 kHz for the MFC transducer and 55, 60, 65, 70, 75 kHz for the Quick Pack transducer. These values covered the optimum operating frequency ranges of the corresponding transducer types with 0.15 mH compensating inductance.

Measurement B

- Scan points were defined on the longitudinal centrelines of the transducers. The points were positioned at three distances from the transducer edge: 0.1, 0.25 and 0.5 m.
- Three drive voltage amplitudes were used: 5, 10 and 20 Vpp.

- The inductive compensation was 0.15 mH.
- The frequencies were 181 kHz for the MFC and 65 kHz for the Quick Pack.

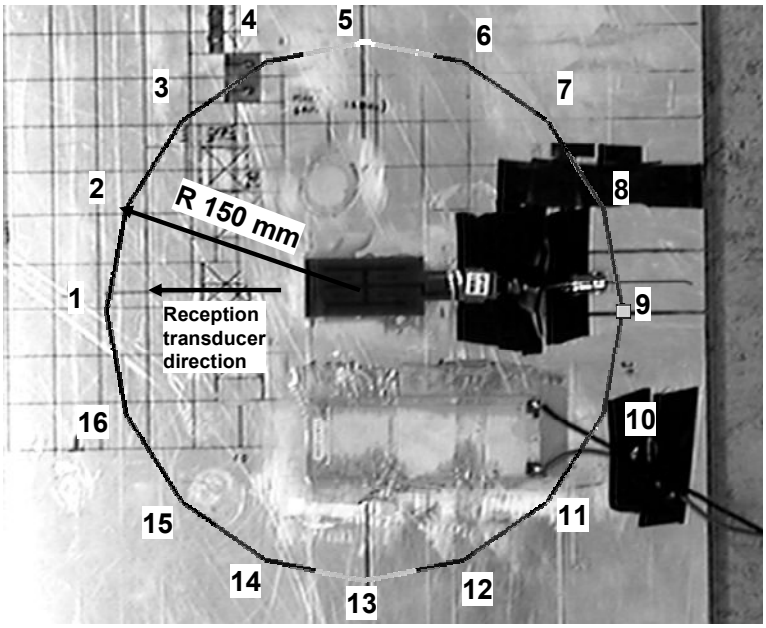

Figure 6.4. Location of scan points used to obtain the radial Lamb wave emission characteristics of Transmission transducers. (Here shown as applied to the QP10n transducer).

Calculations

The out-of-plane velocity amplitudes measured by the vibrometer were converted to out-of-plane displacement amplitudes using the following harmonic motion relationship:

$$A = \frac{V}{2 \cdot \pi \cdot f} \qquad (18)$$

where A is the displacement amplitude, V is the velocity amplitude and f is the frequency. From these, the in-plane displacement amplitudes, in-plane strain amplitudes and power flux of the Lamb wave signals were calculated using proportionality factors obtained with the use of the Disperse software. (It should be noted that all displacement and strain amplitudes are directly proportional to the out-of-plane amplitude, whicle the power power flux is proportional to the square of the amplitudes.) The transducer units used in the experiment were Quick Pack transducer no. 6 and MFC transducer no. 8 (numbering as shown in Figure 4.3).

6.4.2. Radial characteristics of Transmission transducer

The radial characteristics of the transducers were obtained from Measurement A. Figure 6.5 shows data for the MFC M8528-P1 transducer operating at the optimum frequency of 180 kHz. Figure 6.6 shows data for the Quick Pack transducer operating at the optimum frequency of 65 kHz. In both cases the drive signal had a 20 Vpp amplitude and a 0.15 mH compensating inductor was used in the drive circuit. Data for other measurement frequencies were omitted for clarity. Results from all measured frequencies, in two selected propagation directions, are presented in detail in sections 6.4.3. and 6.4.4.

Measurements in directions 7 to 11 were obscured by reflections from the nearest plate edge or were positioned outside the plate. Therefore data from these points is not plotted on the radial plots.

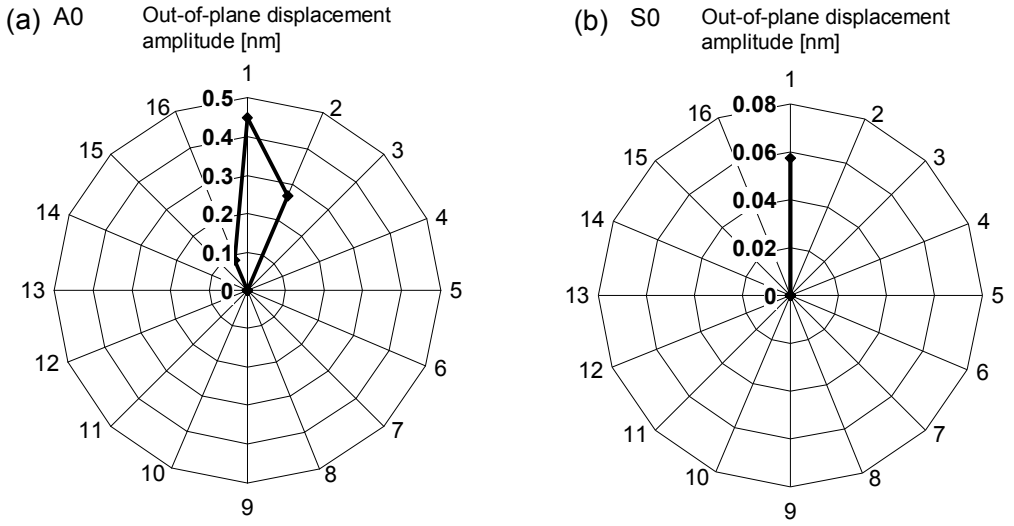

Figure 6.5. Radial emission characteristics of the MFC M8528-P1 transducer. (a): A_0 mode, (b): S_0 mode transmission. The quantity plotted is the out-of-plane displacement amplitude in nanometres. The frequency is 180 kHz. Drive signal 20 Vpp, circuit with 0.15 mH inductive compensation.

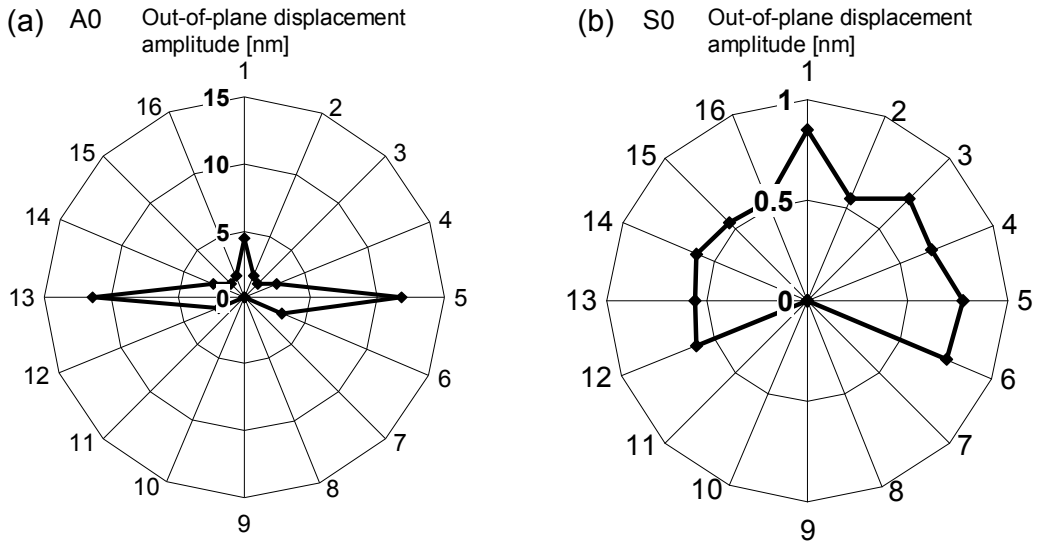

Figure 6.6. Radial emission characteristics of the QP10n transducer. (a): A_0 mode, (b): S_0 mode transmission. The quantity plotted is the out-of-plane displacement amplitude in nanometres. The frequency is 65 kHz. Drive signal 20 Vpp, circuit with 0.15 mH inductive compensation.

MFC M8528-P1

The MFC M8528-P1 transducer emits both A_0 and S_0 mode signals almost exclusively in the longitudinal direction. The A_0 signal can be detected within ± 22.5° of the transducer centreline (scan points "16", "1", "2") and its displacement amplitude at 180 kHz is 0.45 nm in the longitudinal centreline direction. The S_0 signal can be detected only in the centreline direction and its amplitude reaches 0.11 nm at the same frequency.

QP10n

The Quick Pack QP10n transducer emits the A_0 signal along its longitudinal and transverse axes. The signal fades rapidly away from these directions although it is still detectable at adjacent scan points (± 22.5 ° from the centrelines). The emission is stronger along the transverse centreline. At 65 kHz the displacement amplitude of the A_0 mode signal transmitted from the longer axial edge reaches 11.8 nm, while the amplitude of this mode transmitted from the shorter transverse edge reaches 4.4 nm. This suggests that the orientation of the Quick Pack transducer in the experimental set-up is not optimal. One can expect that the power transmission will be higher if the Quick Pack transmitting transducer is orientated with its longer edge facing the receiver. Such an orientation would allow the higher amplitude signal emitted along the transverse axis to reach the receiving transducer. The S_0 mode is transmitted almost uniformly in all directions with the amplitude in the vicinity of 0.8 nm.

6.4.3. Detailed comparison of transducers in the longitudinal direction

The presentation of the Transmission transducer characteristics on radial plots omits much of the available information, such as the dependence of the amplitude on the frequency and inductive compensation. Since both transducer types transmit almost exclusively along one or both of their axes, it is beneficial to present a detailed analysis of their performance in these directions. This section presents data from the "1" direction on the radial scan – that is along the longitudinal centreline. Transmission in this direction occurs in both the MFC and the QP transducer, allowing direct comparison.

In addition to the data from the radial measurement presented in the preceding section, results from Measurement B, carried out exclusively for the "1" direction, are presented. This experiment adds information about the dependence of the signal amplitude on the drive voltage and the distance from the transducer.

Figure 6.7 to Figure 6.10 show the how the behaviour of several Lamb wave mode characteristics changes depending on the frequency. Figure 6.11 shows the relation of the out-of-plane displacement amplitudes to the drive voltage and distance from the transducer.

The amplitudes of the signal generated by the QP transducer are approximately ten times higher than those of the signal generated by the MFC in their respective frequency ranges. Apart from this difference, within the investigated frequency range the characteristics of both transducer types are influenced in similar ways by factors such as frequency and inductive compensation. Therefore they will be discussed here jointly.

Out-of-plane displacement amplitude

The out-of-plane displacement amplitudes of the generated signal do not change significantly with the frequency (Figure 6.7). The A_0 mode amplitude is consistently approximately three to ten times larger than the amplitude of the S_0 mode.

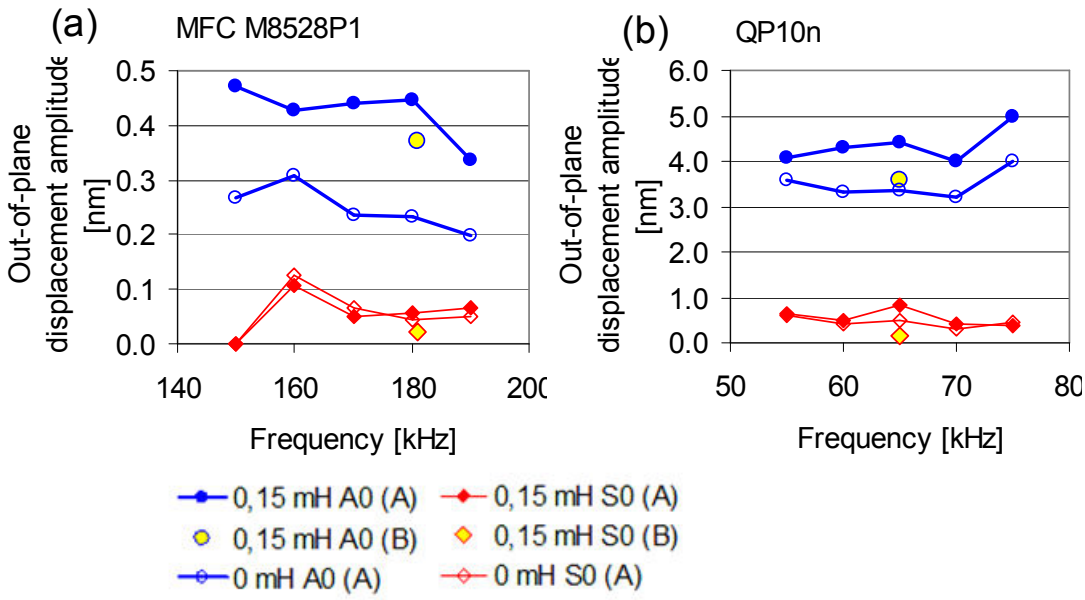

Figure 6.7. Emission characteristics of (a) MFC M8528-P1 and (b) QP10n transducer in direction 1 (longitudinal). The plotted quantity is the out-of-plane displacement amplitude. Capital letters (A) and (B) denote data from Measurement A and Measurement B.

Effect of inductive compensation

In the case of the Quick Pack transducer, the use of a 15 mH inductive compensation in the transmission system has a similar effect on amplitudes of both Lamb wave modes. Table 6.1 shows a summary of amplitude increases recorded in the tested frequency range. On average, both modes' amplitudes increased approximately by a factor of 1.25.

Table 6.1. Comparison of amplitude increase ratios caused by the use of a 15 mH inductive compensation in the circuit driving a Quick Pack QP10n transducer. Data from Measurement A.

Frequency [kHz]	Ratio of out-of-plane amplitudes: with 15 mH compensation / without compensation	
	A_0	S_0
55	1.133	1.086
60	1.297	1.171
65	1.315	1.784
70	1.238	1.370
75	1.241	0.865
Average:	**1.245**	**1.255**
St. deviation / average	0.057	0.276

Inductive compensation was expected and shown to work with different effect at different frequencies. Thus, the variation of amplitude increase across the frequency range for each mode can be a result of this phenomenon. Such variation, however, should be the same for both modes. Table 6.1 also shows values of the coefficient of variation (standard deviation normalised with respect to the average) for both modes' data. The S0 mode data has a higher variation than the A0 mode. This may suggest that the measurement variation was higher in the case of the S0 mode and added onto the variation caused by the changing effect of the inductive compensation. Such an effect may be explained by the lower amplitude of the S0 mode, which made the measurement and reading of its changes less accurate and repeatable.

Table 6.2 Comparison of amplitude increase ratios caused by the use of a 15 mH inductive compensation in the circuit driving a MFC8528-P1 transducer. Data from Measurement A.

Frequency [kHz]	Ratio of out-of-plane amplitudes: with 15 mH compensation / without compensation	
	A_0	S_0
150	1.759	no signal detected
160	1.379	0.856
170	1.862	0.750
180	1.931	1.327
190	1.706	1.311
Average:	**1.728**	**1.061**
St. deviation / average	0.124	0.284

In the case of the MFC transducer (data shown in Table 6.2), the A0 mode appears to be significantly more affected by the inductive compensation (increase by a factor of 1.73) than the S0 mode (increase by a factor of 1.06). This is contrary to what was expected, namely that both modes' amplitudes should increase by the same factor. In the author's opinion this discrepancy was caused by a large inaccuracy of the S0 mode amplitude measurement. The S0 mode amplitude was near the noise level (see Figure 6.3 (a)) and at 150 kHz the S0 mode could not be detected at all. This negatively affected the measurement accuracy.

In-plane displacement and strain

The in-plane displacement and strain amplitudes are plotted in Figure 6.8 and Figure 6.9. In the case of the S_0 mode, the in-plane displacement amplitudes are an

order of magnitude larger than the previously discussed out-of-plane displacement amplitudes.

The relation between the A_0 and S_0 mode amplitudes is the inverse of that which occurs in the case of the out-of-plane movement. The in-plane displacement amplitudes of the A_0 mode are between three and thirty times smaller than the corresponding amplitudes of the S_0 mode.

The in-plane strain amplitudes of the A_0 mode are up to four times smaller than those of the S_0 mode. This observation is especially important for the operation of patch transducers as they interact with the in-plane strain field of the Lamb wave (di Scalea 2007).

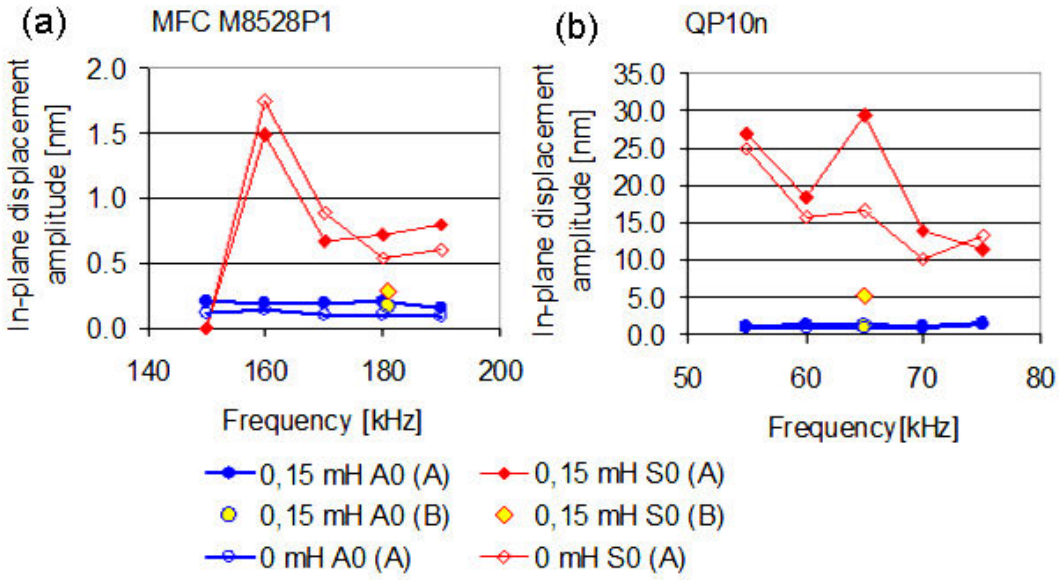

Figure 6.8. Emission characteristics of (a) MFC M8528-P1 and (b) QP10n transducer in direction 1 (longitudinal). The plotted quantity is the in-plane displacement amplitude. Capital letters (A) and (B) denote data from Measurement A and Measurement B.

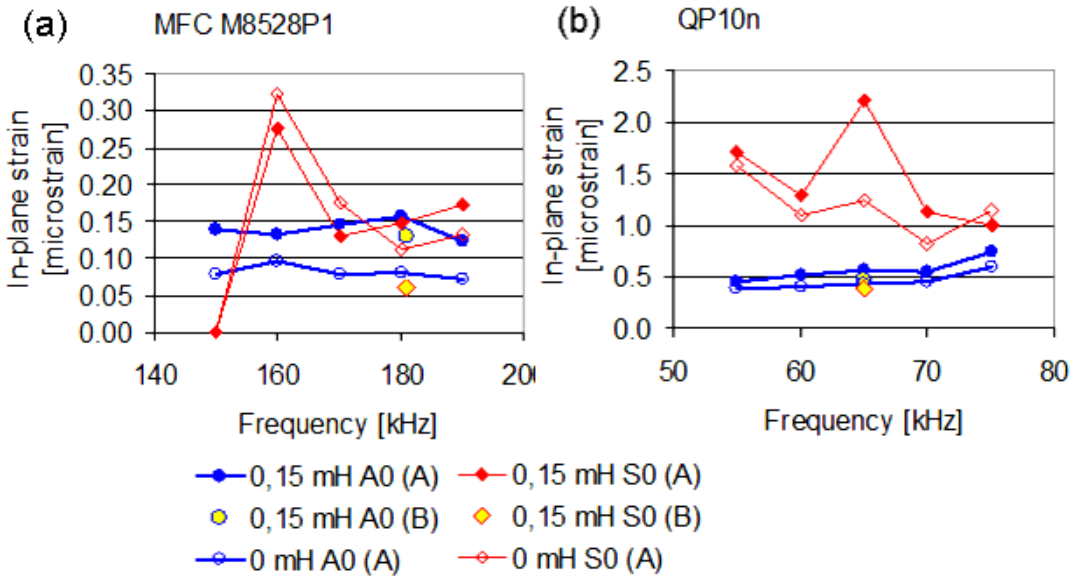

Figure 6.9. Emission characteristics of (a) MFC M8528-P1 and (b) QP10n transducer in direction 1 (longitudinal). The plotted quantity is the in-plane strain amplitude. Capital letters (A) and (B) denote data from Measurement A and Measurement B.

Energy flux

Figure 6.10 shows the energy flux associated with Lamb wave modes. The amount of power transported by the S_0 mode is on average one order of magnitude higher, than the amount of power transported by the A_0 mode. This emphasises the importance of the S_0 mode in the energy transmission application.

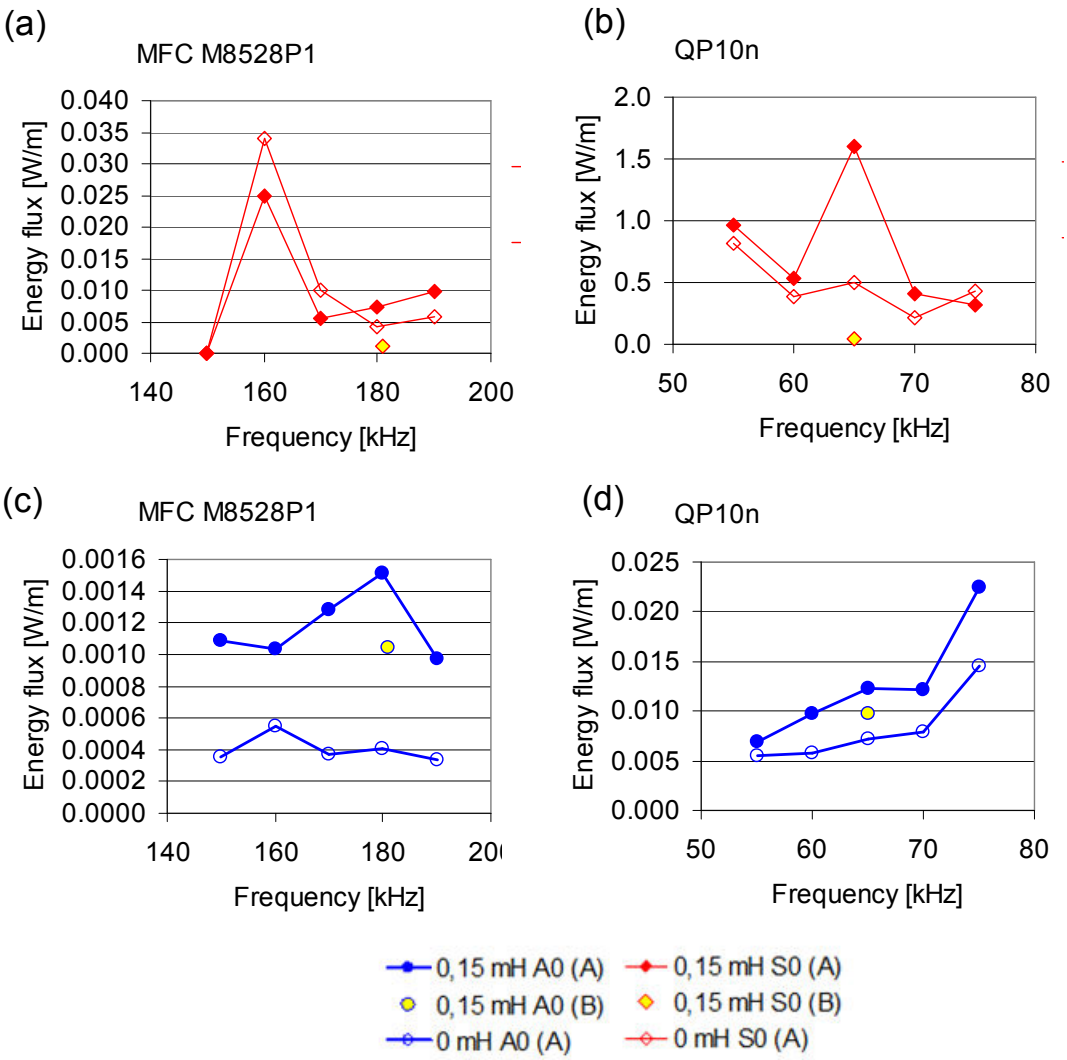

Figure 6.10. Energy flux of the Lamb wave generated by the tested transducers. The unit used is W/m, meaning power passing through a plate cross-section area 1 m wide in a plate of 1.5 mm thickness. Data are for (a) MFC M8528-P1 S_0 mode, (c) MFC M8528-P1 A_0 mode, (b) QP10n S_0 mode, (d) QP10n A_0 mode. Capital letters (A) and (B) in the legend denote data from Measurement A (direction 1) and Measurement B.

Dependence on drive voltage

Figure 6.11 shows the relations between the drive voltage, the distance from the transducer and the out-of-plane displacement amplitude. In all cases the amplitude increases linearly with the drive voltage and decreases in an approximately inverse proportion to the distance from the transducer. As mentioned in section 5.2.1. the Quick Pack transducer was reported to operate safely up to the drive voltage of 1200 V, and the MFC was reported to operate safely up to 1500 V (Prestorius 2004). The author's discussions with other researchers indicate that transducers are expected to behave linearly up to these maximum voltages, above which the failure mechanism is

electric arcing between the electrodes. The author was, however, unable to find published data confirming this experience.

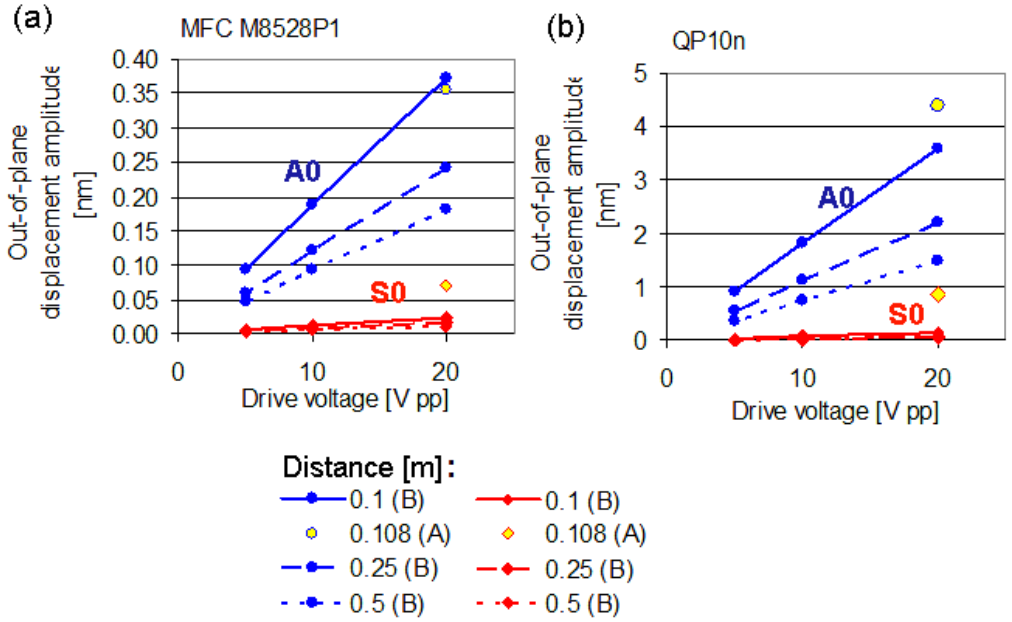

Figure 6.11. Emission characteristics of (a) MFC M8528-P1 and (b) QP10n transducer in direction 1 (longitudinal). Data for a single frequency (QP: 65 kHz, MFC: 181 kHz), plotted against the drive voltage and distance from the transducer. All data for a drive circuit with a 0.15 mH inductor.

6.4.4. Detailed comparison in the transverse direction

QP10n

The QP10n transducer transmits signals also in the transverse direction. The measured out-of-plane displacement amplitude of the A_0 mode is approximately three times higher than in the longitudinal direction (Figure 6.12 (a)). The amplitude of the S_0 mode is comparable to that measured in the longitudinal direction.

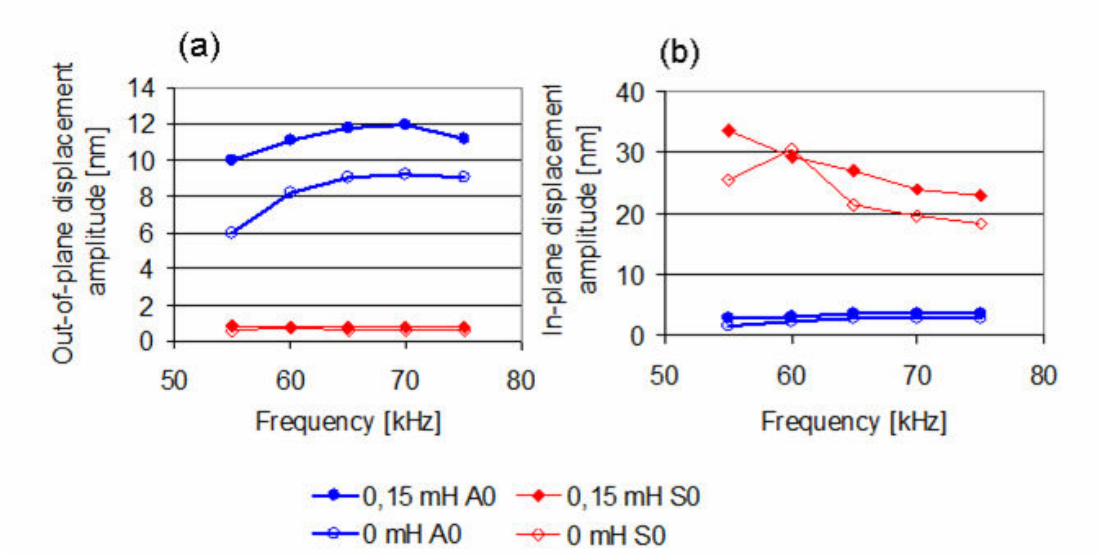

Figure 6.12. Emission characteristics of QP10n transducer in direction 5 (transverse). (a) out-of-plane displacement amplitude as a function of frequency, (b) in-plane displacement amplitude as a function of frequency.

The in-plane displacement amplitudes of the S_0 mode are approximately ten times higher than the corresponding amplitudes of the A_0 mode (Figure 6.12 (b)). The difference between in-plane strain amplitudes of both modes is smaller (Figure 6.13 (a)). The amount of energy carried by the S_0 mode is between three and six times larger than that carried by the A_0 mode (Figure 6.13 (b)).

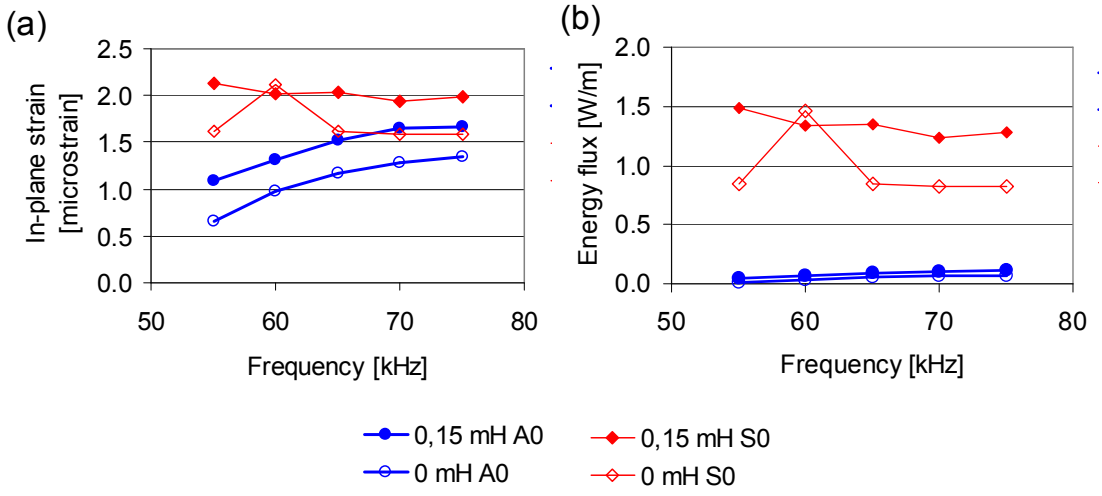

Figure 6.13. Emission characteristics of QP10n transducer in direction 5 (transverse). (a) out-of-plane strain amplitude as a function of frequency, (b) energy flux as a function of frequency.

6.5. Propagation of continuous Lamb wave signal in plate

6.5.1. Introduction

In this section the propagation of continuously generated Lamb wave signals in the experimental aluminium plate is characterised. This knowledge is necessary for understanding the energy transmission between the transmission and the reception transducers. In particular, the emergence of a standing wave pattern during the continuous propagation of Lamb waves is described in this section. The existence of a standing wave is of high importance to the design of the ultrasonic energy transmission system as it introduces another layer of complexity to the already difficult task of Lamb wave generation and reception.

6.5.2. Methodology

For the imaging of a standing wave the FFT mode of the laser vibrometer was the most suitable. In this measurement mode the time domain information was removed and only the vibration amplitude information was retained. Scans of areas ranging from the immediate transducer surroundings to the entire experimental plate were conducted. In small area scans a spatial resolution of approximately 1 mm was used. In entire plate scans a 2 mm resolution was used.

The transmission transducer units used in the experiment were Quick Pack transducer no. 6 and MFC: transducer no. 8 (see Figure 4.3).

6.5.3. Results

MFC M8528-P1

The transducer was operated continuously at 181 kHz and driven by a 20 Vpp signal. The circuit used 0.15 mH inductive compensation.

Figure 6.14 shows a map of the out-of-plane vibration displacement amplitude over the entire test plate. A beam with amplitudes reaching ~ 1.5 nm can be seen along the longitudinal axis of the transducers. The receiving transducer is positioned within this beam. In most areas of the plate outside of the beam the vibration amplitude is approximately 0.2 nm. Irregular strand-shaped areas of vibration with amplitudes reaching about 0.5 nm can also be identified. The maximum amplitude in continuous operation, 1.5 nm, is approximately three times higher than the amplitude

measured in pulsed operation. This shows that a significant amount of energy is pumped into and maintained in the plate during a continuous operation.

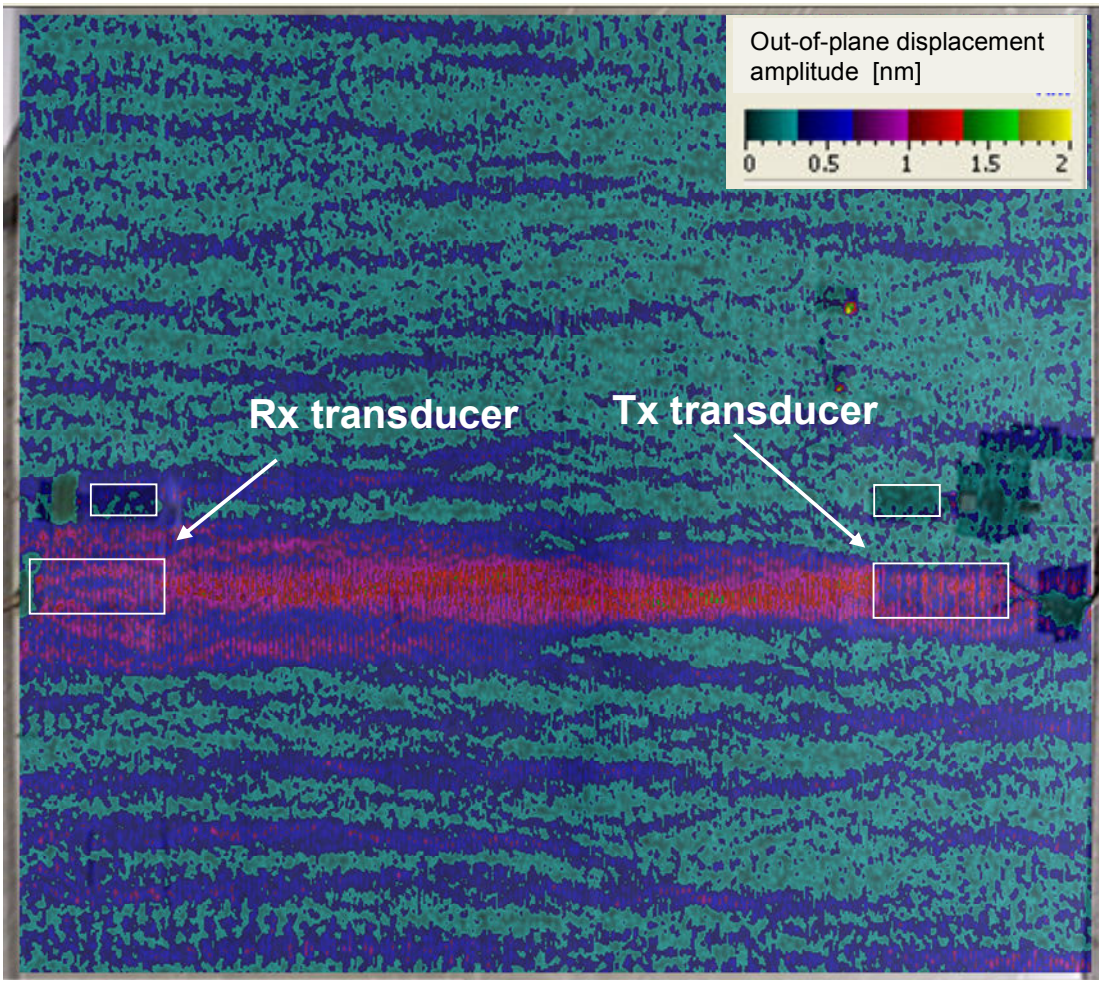

Figure 6.14. Laser vibrometer FFT scan of the entire aluminium plate during a continuous operation of the MFC M8528-P1 transducer at 181 kHz.

Figure 6.15 provides a close-up view of the areas surrounding the transmitting transducer. Within the main signal beam a standing wave pattern with the period of 4 mm can be seen. The 4 mm period equals one half of the 8 mm wavelength of the A_0 mode signal. A secondary pattern corresponding to the S_0 mode is not found. (Since the wavelength of the S_0 mode at 181 kHz is 30 mm, the standing wave pattern corresponding to this mode would have a period of 15 mm.) Another observation that can be made from analysing this figure is that within the main beam the signal amplitude never reaches zero. Thus the pattern is a so-called partial standing wave.

The observed amplitude pattern is an envelope under which a moving wave is travelling.

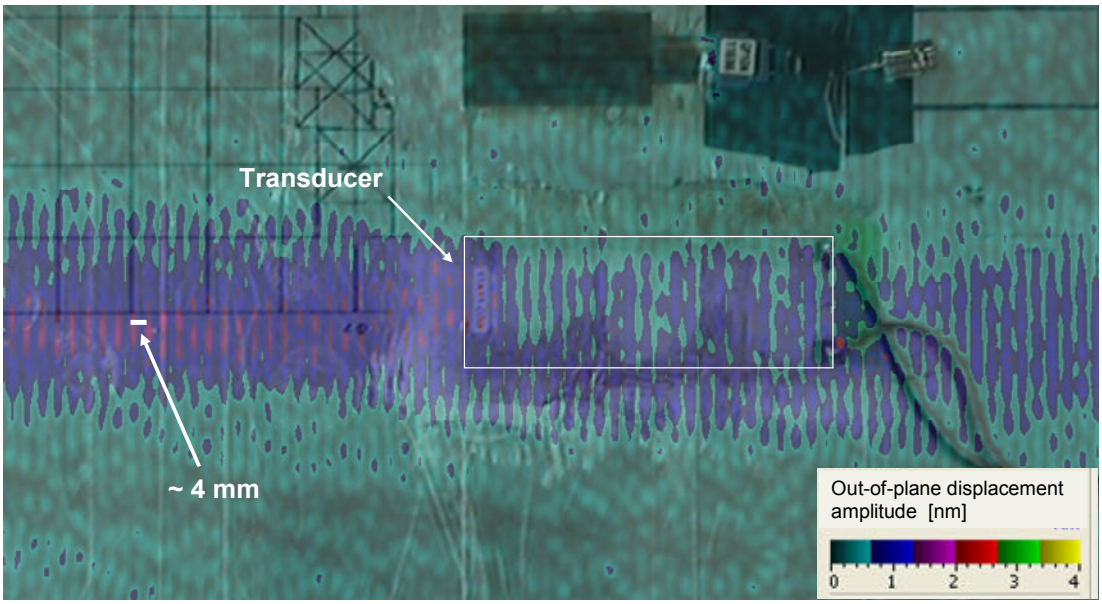

Figure 6.15. Out-of-plane vibration displacement amplitude scan of the area surrounding the MFC M8528-P1 transmit transducer during continuous operation at 181 kHz.

In order to measure the standing wave patter with more precision, profiles of the pattern were plotted along longitudinal and transverse axes of the transducers. Locations of these profile lines are shown in Figure 6.16. These will be referred to as A, B and C in the subsequent text.

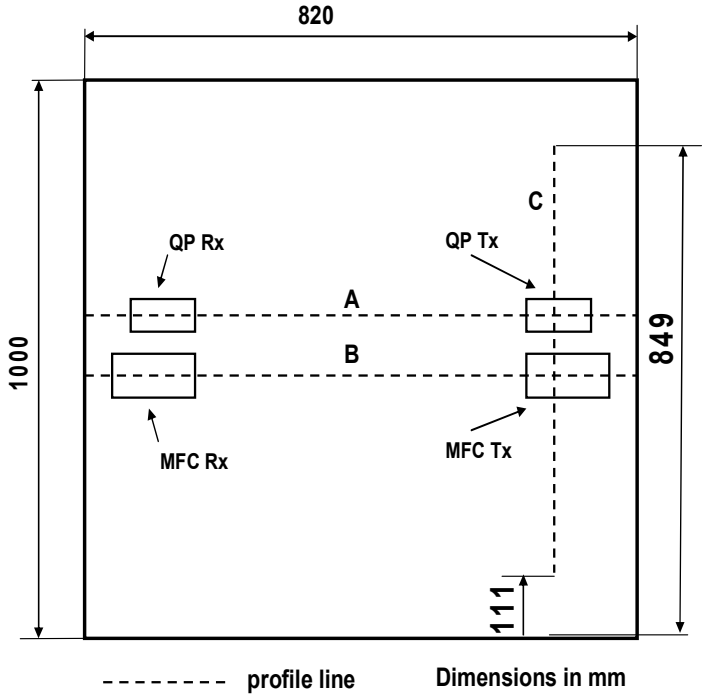

Figure 6.16. Sketch showing locations of amplitude profile lines on the plate.

Figure 6.17 shows a profile of the out-of-plane vibration displacement amplitude measured along the longitudinal axis of the MFC transducers (line A). Again, the 4 mm pattern can be easily distinguished. In the space between the transducers the average standing wave ratio of this pattern is 0.63. A longer-wavelength pattern seems to be present as well, but on closer inspection it becomes apparent that the period of this pattern is not constant and cannot be confidently related to the S_0 mode.

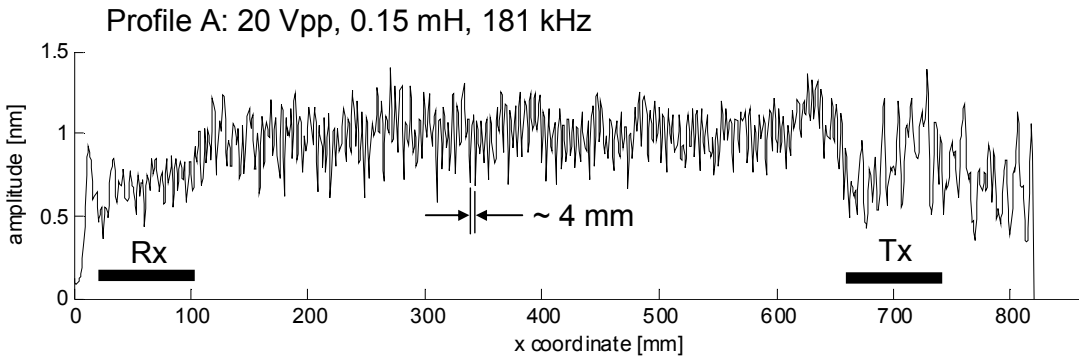

Figure 6.17. Vibration amplitude profile along the line connecting the MFC M8528-P1 transmit and receive transducers (line A on Figure 6.16). Transducer operating continuously at 181 kHz. Drive signal 20 Vpp, 0.15 mH inductive compensation. Locations of transducers shown under the profile line.

The signal amplitude on the surface of the transducers is smaller than in the space between them. One can speculate that the reasons for this are as follows. Firstly, the additional thickness of the transducer masks the vibration of the plate surface. Secondly, for the receive transducer, the decrease in the vibration amplitude may be caused by the damping effect of the piezoelectric transducer. Thirdly, the vibration pattern observed on the surface of the transmit transducer is a superposition of the Lamb wave vibration already present in the plate and the transducer's own actuating action. The Lamb wave pattern has the wavelength of 4 mm, whereas the transducer is actuated to contract and expand as a whole, uniformly along its 84 mm length, and there is a possibility of destructive interference between the two motions. In addition, Figure 6.15 shows that the vibration pattern on the transmit transducer is not positioned symmetrically in relation to its longitudinal axis. The vibration extends to one side – towards the bottom of the illustration - beyond the transducer's edge. This suggests some asymmetry in the transducer operation or in the quality of the bond between the transducer and the plate.

QP10n

The transducer was operated continuously at 65 kHz and driven by a 20 Vpp signal. The circuit used 0.15 mH inductive compensation.

Figure 6.18 shows a map of the out-of-plane vibration displacement amplitude over the whole test plate. A beam of vibration with the out-of-plane amplitude reaching 42 nm is radiated by the transmit transducer in the transverse direction. This effect is in line with the previously measured directional characteristics of the QP10n transducers, which were found to transmit a higher amplitude signal in the transverse direction. The amplitude in the continuous operation is approximately four times higher than the amplitude recorded earlier in a pulsed operation. The transverse beam is repeated multiple times along the transducer's longitudinal direction. The distance between the transverse beams is not constant. Along the line connecting the transmission and the reception transducers the distance between the beams varies around 120 mm. This distance cannot be correlated with any Lamb wave mode wavelength at the frequency of 65 kHz. In addition, the lines which the beams follow are curved.

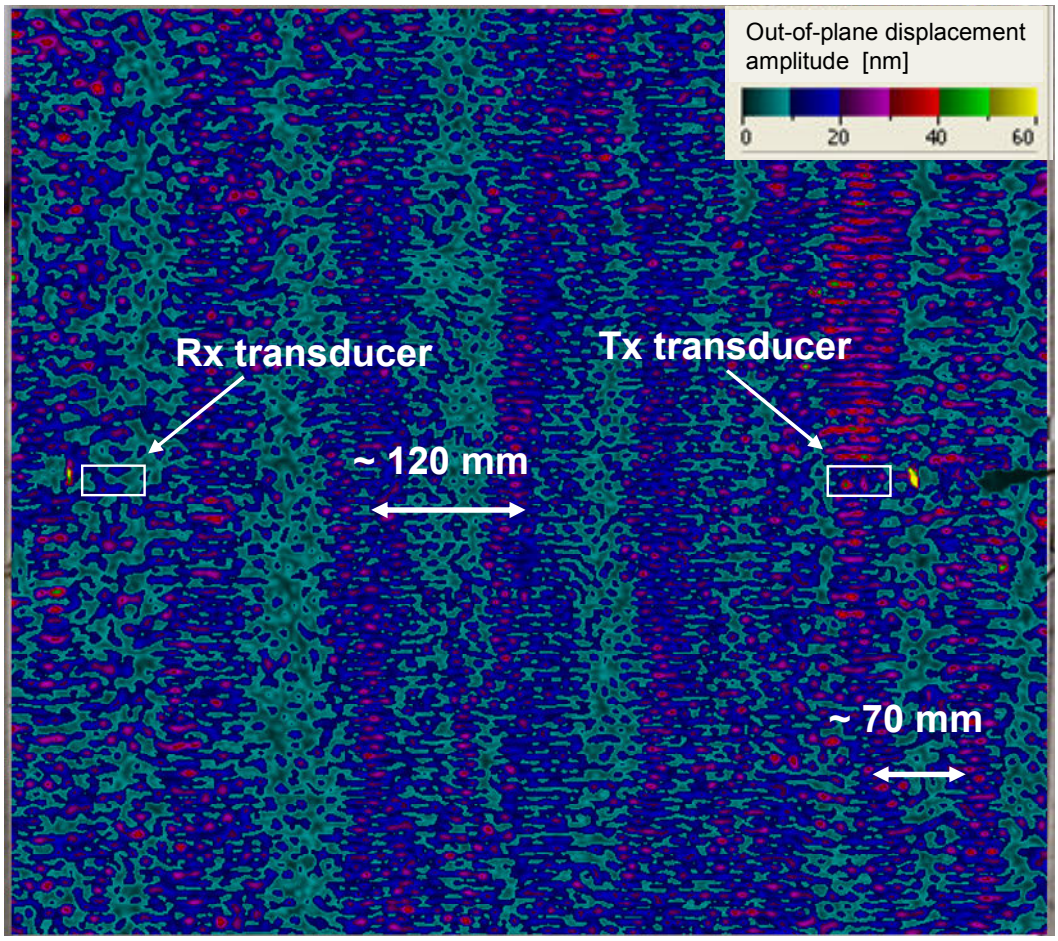

Figure 6.18. Laser vibrometer FFT scan of the entire aluminium plate during a continuous operation of the QP10n transducer at 65 kHz.

Figure 6.19 provides a magnified view of the areas surrounding the transmitting transducer. The standing wave pattern is two-dimensional and appears to be a superposition of signals propagating in both longitudinal and transverse directions. In the transverse beam radiated by the transducer a pattern with a period of roughly 8 mm can be found. This corresponds to one half of the A_0 mode wavelength, which at 65 kHz is 14.6 mm. A pattern with the same period can also, occasionally, be identified in the longitudinal direction. The S_0 mode wavelength at 65 kHz is 83.7 mm. A standing wave pattern with the period equal to one half of this wavelength could not be identified.

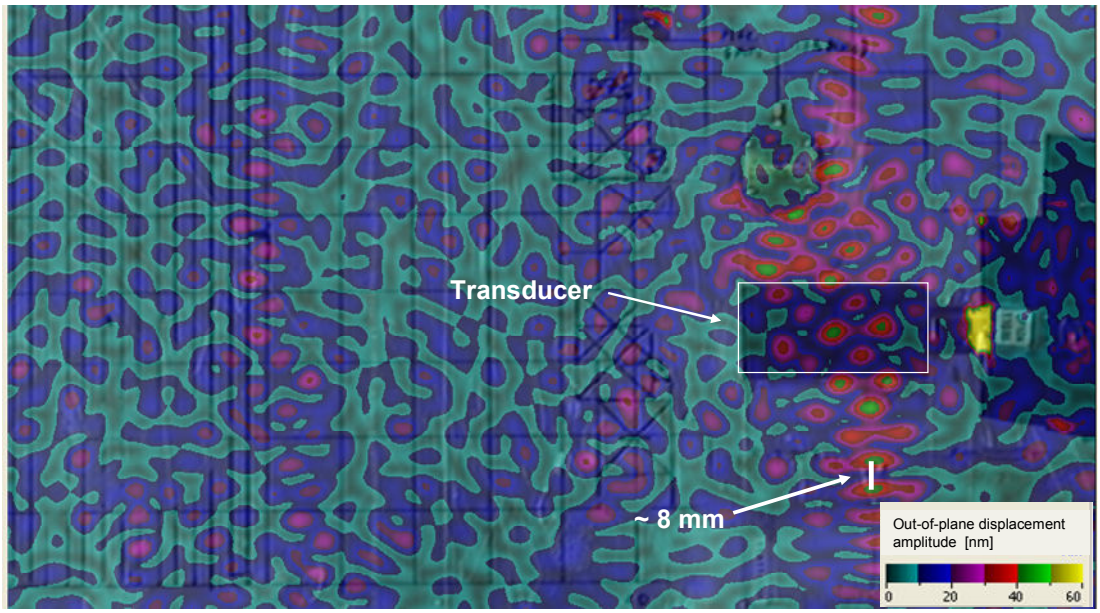

Figure 6.19. Laser vibrometer FFT scan of the MFC M8528-P1 transmit transducer surrounding area during continuous operation.

Figure 6.20 shows a profile of the out-of-plane vibration displacement amplitude measured along the longitudinal axis of the transducers (line B). The profile is irregular. Only in rare instances can peaks and troughs separated by about 8 mm be found. The maximum amplitude of the signal in the space between the transducers is 22 nm, the minimum amplitude is 2 nm.

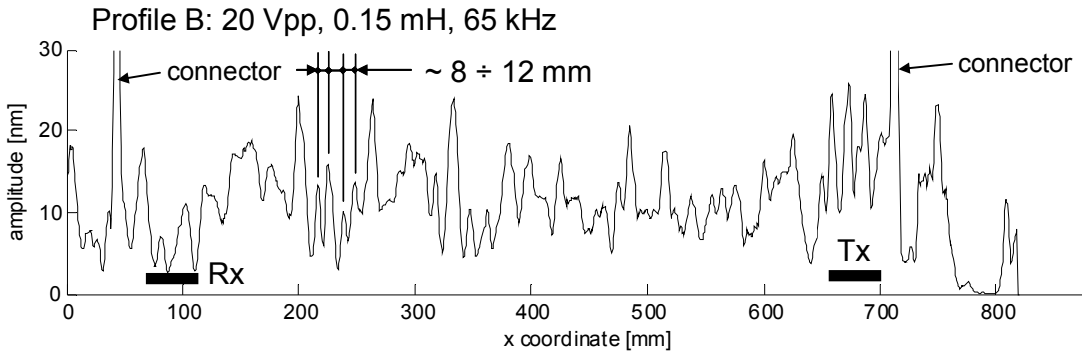

Figure 6.20. Vibration amplitude profile along the line connecting the QP10n transmit and receive transducers (line B on Figure 6.16). Transducer operating continuously at 65 kHz. Drive signal 20 Vpp, 0.15 mH inductive compensation. Locations of transducers shown under the profile line.

Figure 6.21 shows a profile of the out-of-plane vibration displacement amplitude measured along the transverse axis of the transmit transducer (line C). This is the profile of the strong transverse beam transmitted by the QP10n transducer. A regular pattern with the 8 mm period can be seen on the profile. Lower-frequency peaks

separated by approximately 45 mm can also be identified. These, with a degree of caution, may be related to the S_0 mode wave. The maximum signal amplitude recorded in the profile is 42 nm, the minimum amplitude is 6 nm. The average standing wave ratio of this pattern is 0.36.

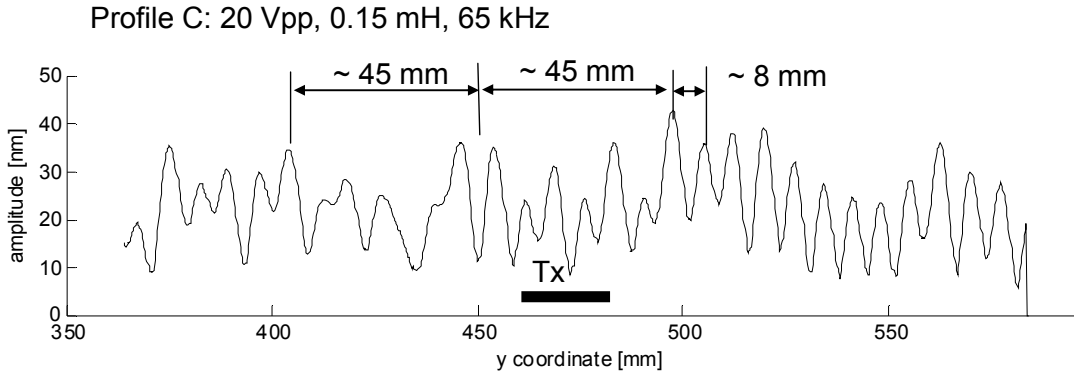

Figure 6.21. Vibration amplitude profile along the transverse axis of the transmit QP10n transducer (line C on Figure 6.16). Transducer operating continuously at 65 kHz. Drive signal 20 Vpp, 0.15 mH inductive compensation. Location of the transducer shown under the profile line.

The FFT scans of the QP10n set-up suggest that the orientation of the transmit transducer is not optimal. With the orientation used in the set-up analysed here the strongest signal is transmitted transversally, 90° away from the receiving transducer. This suggests an optimisation step whereby the transmit transducer is bonded with its longer edge facing the receive transducer. Such modified geometric configurations were built and tested experimentally. The results of these experiments, in regard to both Lamb wave propagation and the electrical power transmission performance, are described in Chapter 7.

6.6. Operation of Reception transducers

In this section the vibration signal reaching the receive transducer is characterised in the time domain. Subsequently, a single metric describing the signal's ability to excite the receive transducer is derived. Finally, this metric is compared with the output voltage of the transducer and the transducer transfer function is derived.

The method described in this section can be used to determine the optimum location of the receive transducer in a practical application. The vibration data can be sourced from laser vibrometer measurements (as described here) or from simulation. From these data, the transducer output voltage can be predicted for each considered

location, allowing the designer to choose the optimum point at which to place the receiver.

As described by di Scalea (2007) the output voltage generated by a patch piezoelectric transducer is proportional to the value of the in-plane strain field to which the transducer is subjected averaged over the transducer area. In di Scalea (2007) this proportionality constant is analytically derived from the elastic and piezoelectric constants of the transducer material and from the dimension of the transducer. One can expect that in a practical application it will also be affected by other design characteristics, such as the placement of the electrodes or the mechanical characteristics of the material in which the piezoelectric patch is encapsulated.

In this section a method of deriving the amplitude of the averaged strain field value from laser vibrometer measurements is presented. Subsequently, the derived values are compared with the transducers' open circuit output voltage amplitude measurements to experimentally derive the transducer's proportionality constant.

6.6.1. Incoming signal characterisation method

In this subsection a method for calculating the average strain amplitude based on laser vibrometer data is presented. It should be noted that all examples shown here use out-of-plane displacement field data, rather than the in-plane strain field data. This is an important factor affecting the applicability of the described method. The patch-type transducer responds to the in-plane strain field. The one-dimensional vibrometer used in the measurement provided only the out-of-plane displacement data. In the case of the A_0 mode the out-of-plane displacement and the in-plane strain occur in the same phase with proportional amplitudes. The out-of-plane displacement and the in-plane strain of the S_0 mode occur in opposite phases. Thus, the out-of-plane data is an indication of the in-plane strain seen by the transducer only if one of the modes is dominant. Results presented later in this section suggest that this is the case only in the Quick Pack transducer-based setup. With this limitation, all other steps of the method are considered correct and can be directly applied to in-plane motion data should it be available.

Figure 6.22 illustrates the calculation process. A MATLAB code was written to carry out the required calculations. In Step 1, the scan area of the vibrometer is adjusted to match the area of the transducer piezoelectric patch. The time domain

scan mode is used to record the vibration over the duration of one oscillation cycle. The cycle duration is assumed to be the period of the signal used to drive the transmitting transducer at the chosen frequency. Four snapshots of the displacement field (at 0.00, 0.25, 0.50 and 0.75 of the cycle) are exported as data tables.

In Step 2, the four snapshots are interpolated in order to create a set of 20 snapshots distributed within the duration of one vibration cycle. The interpolation assumes the vibration of each scanned point is sinusoidal in the time domain. This assumption is supported by the fact that the excitation signal is sinusoidal and that all time domain waveforms observed in the laser vibrometer measurements were sinusoidal. Subsequently, the average displacement value (over the area of the transducer) is calculated for each of the 20 time points.

In Step 3, the calculated 20 average displacement values are brought together and plotted against time. From this the amplitude of the resulting waveform can then be calculated.

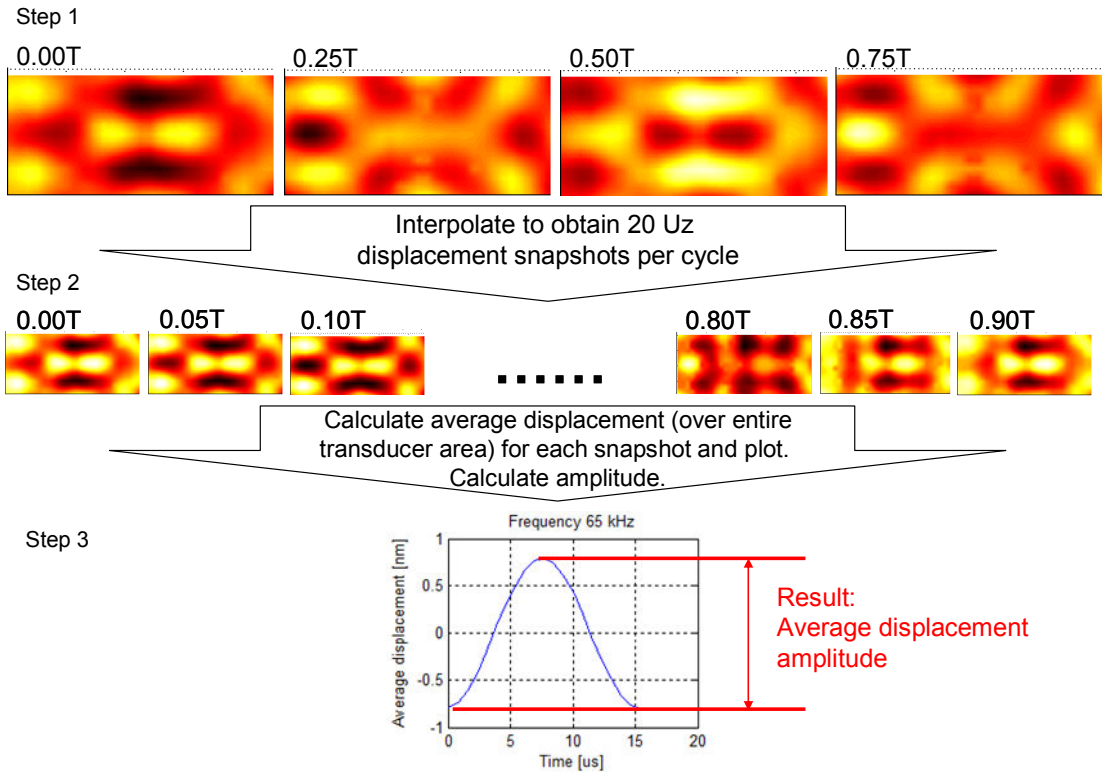

Figure 6.22. Diagram illustrating the process of calculating the averaged out-of-plane displacement amplitude from four out-of-plane displacement snapshots.

6.6.2. Incoming signal characterisation results

MFC M8528-P1

The four time domain snapshots of the out-of-plane displacement field which form the basis of the incoming signal characterisation are shown in Figure 6.23. The operating frequency is 180 kHz. At times equal to 0.0T and 0.50T (where T is the oscillation period) a wave with a wavelength of approximately 8 mm can be seen. These waves can be identified as the Lamb wave A_0 mode. At 0.25T and 0.75T, however, the waves nearly disappear. This can be interpreted as a destructive interference effect between the direct and reflected wave. The phenomenon can also be described as an 8 mm Lamb wave moving under the envelope of the standing wave pattern shown in Figure 6.14.

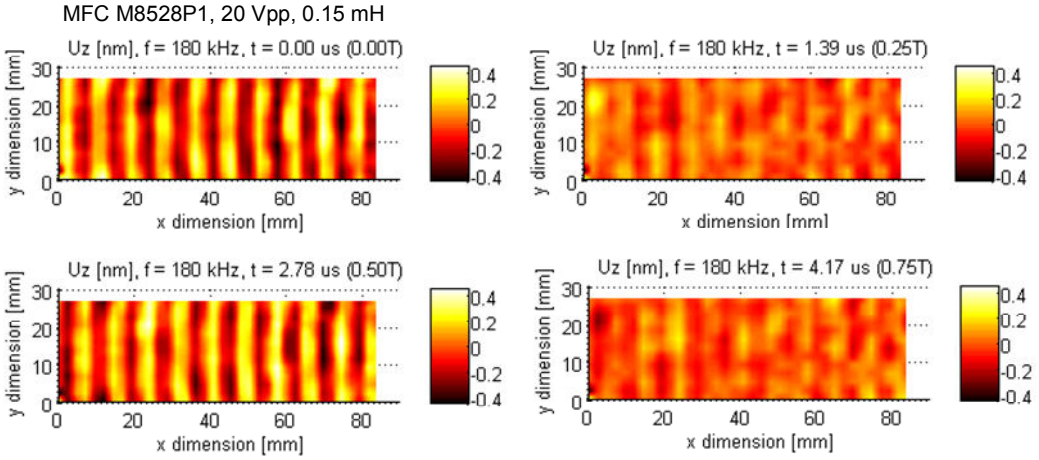

Figure 6.23. Four time domain snapshots of the out-of-plane displacement field experienced by the MFC M8528-P1 receive transducer. The transmit transducer operated at 180 kHz, driven by a 20 Vpp signal in a circuit with 0.15 mH inductive compensation.

Figure 6.24 shows a comparison between the open circuit output voltage amplitudes and the calculated average out-of-plane displacement amplitudes. Only five data points at frequencies in the range of 150 – 190 kHz were collected. This was due to the fact that the measurement and data processing was not automated and obtaining each data point required a significant amount of time. The building of an automated system (especially automating the data recording within the laser vibrometer software) would have exceeded the timeframe allocated for this work. The two characteristics presented in Figure 6.24 do not correlate within the investigated frequency range. The reason for the lack of correlation is believed to be

the fact that the calculation uses out-of-plane displacement rather than the in-plane-strain data. Another cause could be the fact that the Lamb wave wavelength is small in comparison to the transducer length. Because of this even a small inaccuracy in the definition of the scan area can significantly change the number of wavelengths fitting within its length. Such a change can in turn strongly affect the calculated average displacement value.

It can be argued that the number of data points (five) shown in Figure 6.24 is not sufficient to make a claim regarding the correlation of the two curves presented in the figure. However, knowing (from results shown in section 6.4.) that the bulk of the energy carried by the investigated Lamb wave signal is contained in the in-plane vibration of the S_0 mode, claiming that the lack of correlation shown in Figure 6.24 is due to the lack of in-plane motion measurements appears justified.

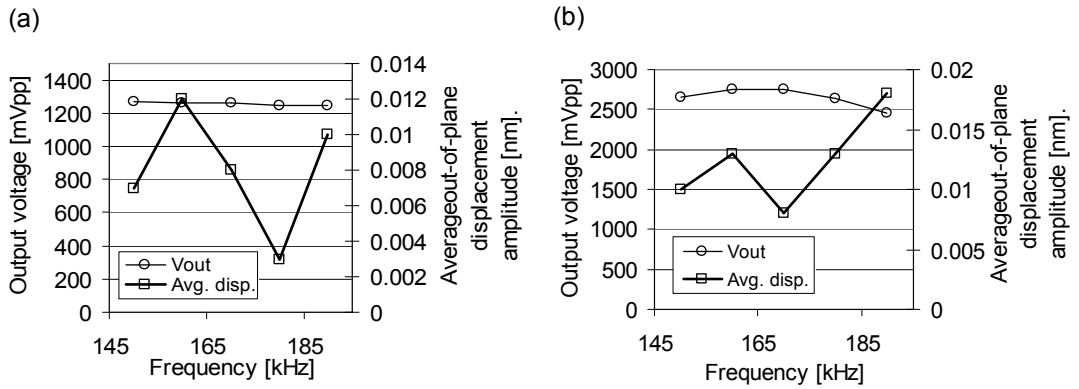

Figure 6.24. Average displacement amplitudes compared with the open circuit output voltage of the MFC M8528-P1 transducer. Drive voltage of the transmit transducer is 20 Vpp. (a) transmit circuit without inductive compensation. (b) transmit circuit with a 0.15 mH inductive compensation.

QP10n

The four time domain snapshots of the out-of-plane displacement field which form the basis of the incoming signal characterisation are shown in Figure 6.25. The operating frequency is 65 kHz. At all times during the vibration cycle the observed displacement pattern is two-dimensional, with periodic features present along both the longitudinal and the transverse axes of the transducer. Features with wavelengths near 15 mm and 7 mm can be distinguished, which correspond to the 14.6 mm A_0 mode wavelength.

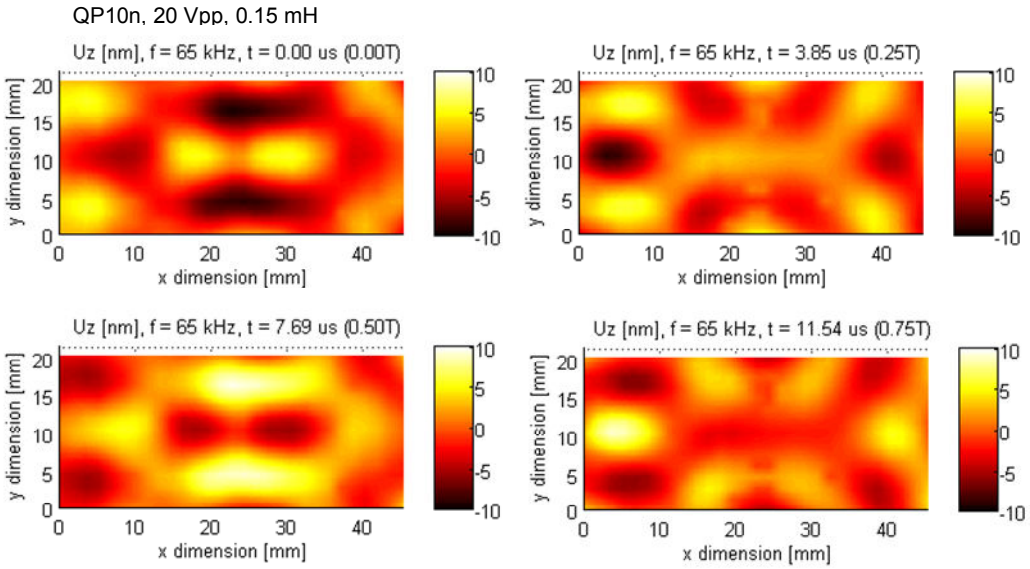

Figure 6.25. Four time domain snapshots of the out-of-plane displacement field experienced by the QP10n receive transducer. The transmit transducer operated at 65 kHz, driven by a 20 Vpp signal in a circuit with 0.15 mH inductive compensation.

Figure 6.26 shows a comparison between the calculated average out-of-plane displacement amplitudes and the open circuit output voltage amplitudes. Contrary to what was observed in the case of the MFC transducer, there is a high degree of correlation between the two characteristics. This is because there are larger ratios between the wavelengths and the transducer dimensions in the case of the QP10n operating at 65 kHz. This decreases the sensitivity of the measurement to the accuracy of the scan area definition. The in-plane strain field under the transducer is also expected to be significantly different than in the case of the MFC.

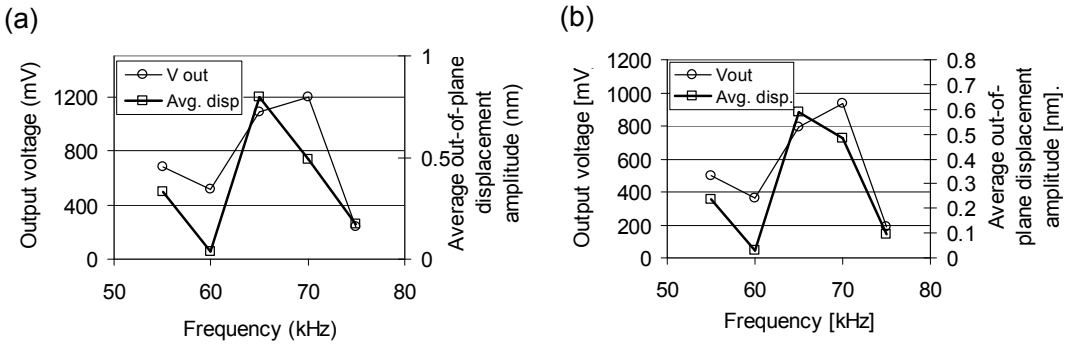

Figure 6.26. Average displacement amplitudes compared with the open circuit output voltage of the QP10n transducer. Drive voltage of the transmit transducer is 20 Vpp. (a) transmit circuit without inductive compensation. (b) transmit circuit with a 0.15 mH inductive compensation.

At this point it is worth re-emphasising that only the use of in-plane strain field data for the calculation presented here would be correct in the general case. The correlation between the average out-of-plane displacement and the output voltage amplitudes discussed here should be treated only as valid for the specific case of one type of transducer and only in the tested frequency range. Nevertheless, it is valuable as an engineering tool for optimising the location for a QP10n receive transducer.

6.7. Summary and discussion

In this chapter the behaviour of the experimental setup with two types of piezoelectric transducers was characterised in terms of Lamb wave generation, propagation and reception. The data was obtained from scanning laser vibrometer measurements.

The directional characteristics of the transmitting transducers were imaged and quantified.

- The MFC M8528-P1 transducer operating in the frequency range of 150 – 190 kHz was found to transmit a narrow beam of a Lamb wave signal along its longitudinal axis. At 180 kHz the out-of-plane amplitude of the signal was 0.45 nm and corresponded to the A_0 mode. The S_0 mode was transmitted with an out-of-plane amplitude of 0.06 nm.
- The Quick Pack QP10n transducer operating in the frequency range of 55 – 75 kHz was found to transmit along both the longitudinal and the transverse axes. At 65 kHz the A_0 mode signal transmitted in the transverse direction had a higher amplitude (11.8 nm) than the signal transmitted in the longitudinal direction (4.4 nm). This suggests that the optimum orientation for a Quick Pack transmitter would be with its longer edge facing the receive transducer. The S_0 signal was transmitted omnidirectionally with an amplitude of approximately 0.8 nm.

Subsequently the propagation of the continuously transmitted Lamb wave signal in the aluminium test plate was imaged.

- A partial standing wave pattern was found to appear in the plate. This pattern results from the interference of multiple direct and reflected signals propagating in the plate. The maximum amplitudes of the standing waves correlate well with the amplitudes of the pulsed signals transmitted by the corresponding Quick Pack and MFC transducers. In both cases, the standing wave amplitude is approximately double the pulsed signal amplitude.

- In the case of the MFC transducer the signal is mainly confined to a narrow beam along the longitudinal axis of the transducer. The observed standing wave pattern has the period of 4 mm, which is one half of the A_0 mode wavelength at the 181 kHz test frequency.
- The Quick Pack transducer generates a two-dimensional standing wave pattern with periodic features observed along both the longitudinal and the transverse dimensions. Such a pattern can be expected taking into account that the transducer was found to transmit along both of its axes. Within the pattern features with the period of 8 mm can be identified. This period is close to one half of the A_0 mode wavelength at the 65 kHz test frequency.

Finally, a method of quantifying the signal reaching the receive transducer was described. The method is based on the approach presented in (di Scalea 2007). In this method the strain field to which the transducer is subjected is recorded over the time of one oscillation cycle. For each time instant the strain is averaged over the transducer area. The amplitude of the averaged strain is then assumed to be directly proportional to the amplitude of the open circuit output voltage of the transducer.

- The availability of a one-dimensional laser vibrometer allowed the measurement of only the out-of-plane displacement associated with the Lamb wave signal passing under the receive transducer. A three-dimensional vibrometer setup would have been needed to map the in-plane strain field.
- Nevertheless an attempt was made to use the out-of-plane data with the method described above. The averaged out-of-plane displacement amplitude was found to correlate well with the output voltage amplitude for the Quick Pack QP10n transducer. The results for the MFC M8528-P1 transducer correlated less well.

The obtained results provide information useful in the design of the ultrasonic power transmission setup. The transducer directional Lamb wave transmission characteristics can be used to decide the optimum orientation of the transmission transducer, so that the most energy is sent in the direction of the reception transducer. The images of the standing wave appearing in the structure during a continuous transmission of Lamb wave signals provide important information regarding the location choice of the reception transducers and the influence of the structure's geometry on the Lamb wave propagation. The standing wave distribution differs significantly depending on the type of the transmission transducer used. This information can inform the choice of the transmission transducer.

6.8. Conclusion

The laser vibrometer scans presented in this chapter significantly expand the understanding of the operation of the prototype ultrasonic energy transmission system investigated in this project. In the next chapter an attempt to use this knowledge in order to improve the system's performance is reported. Based on the measured transmission characteristics of the Quick Pack transducers, which were found to transmit stronger signals from their longer edges, a modified setup is built and tested. In this setup the transmitting transducers are orientated to face the receiving transducer with their longer edges. Electrical performance measurements as well laser vibrometer scans of the modified setup are presented and compared with the configurations investigate previously.

Chapter 7. Optimisation of setup geometry

7.1. Introduction

In this Chapter modifications to the Quick Pack transducer location and orientation as well as of the plate geometry are investigated. These modifications are based on the findings in regard to Lamb wave generation and propagation described in Chapter 6. The energy transmission performance and laser vibrometer scans of Lamb wave propagation patterns are presented and discussed. The significant influence of small changes in the plate geometry is also reported.

7.2. Transducer location

The ultrasonic transmission characterisation of Quick Pack transducers reported in Chapter 6 showed that these transducers transmit stronger Lamb wave signals from their longer edge. Thus an optimisation experiment was planned in which additional Quick Pack transducers were mounted on the aluminium plate, this time with their longer edges facing the reception transducer. Figure 7.1 shows the locations of the transducers on the plate. Units no. 1 and 2 are the newly installed transmission transducers. The new location of the transmitting transducers required a new receiving transducer. A set of two units, orientated perpendicularly to each other, was installed. This allowed the evaluation of the influence of the orientation of the receiving transducer on the power throughput of the system. These reception transducers are units no. 3 and 4 on Figure 7.1. The location of these transducers was determined after laser vibrometer scans of the plate with transducers no. 1 and 2 operating were performed. This allowed the placement of the reception transducers within an area of high Lamb wave vibration amplitude.

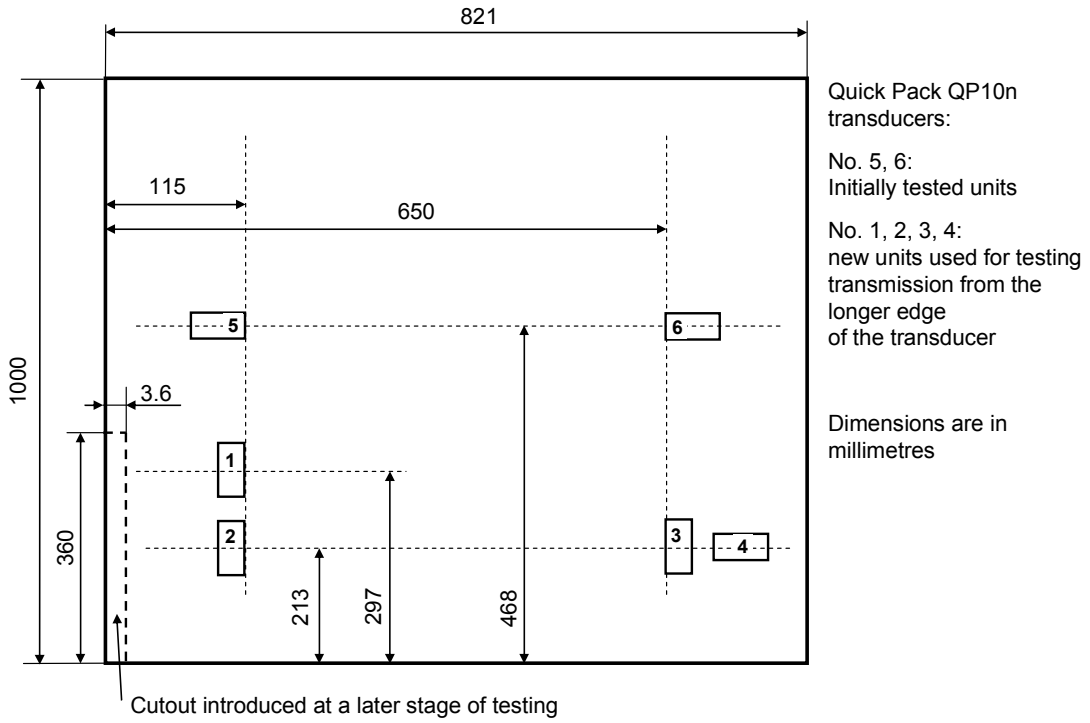

Figure 7.1. Locations of Quick Pack transducers on the experimental plate. Only the Quick Pack transducers relevant to work described in Chapter 7. are shown. In addition to these, two MFC transducers (as shown in Figure 4.3) were present on the plate during measurements described in this Chapter. McWade transducers were removed (it was possible since these were attached with silicone, rather than epoxy, and could have been peeled off without damage.)

7.3. Lamb wave propagation

Laser vibrometer FFT scans of a fragment of the experimental plate with transducer no. 1 and subsequently transducers no. 1 and 2 transmitting were made. The transducers were driven at 65 kHz and a 0.15 mH compensating inductor was used in the drive circuit. The scans, shown in Figure 7.2, revealed a previously not observed Lamb wave propagation pattern. As expected, a relatively strong beam of vibration was observed between the operating transducers and the nearest plate edge (bottom of Figure 7.2). In the direction of the receiving transducer, however, the beam did not appear. Only relatively weak, uniformly distributed areas of vibration were recorded in this part of the plate. This observation was different to what had been observed in earlier scans with transducer no. 6 operating as described in Chapter 6.

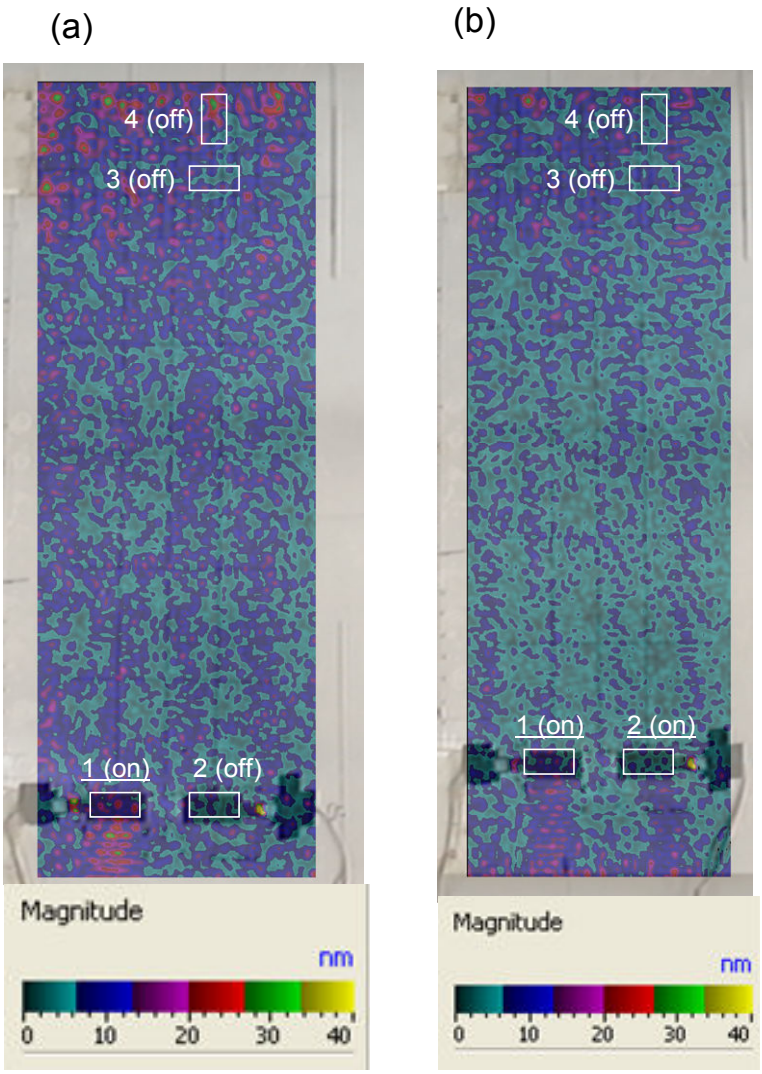

Figure 7.2. FTT laser vibrometer scans of a fragment of the experimental plate with (a) transducer no. 1. transmitting, (b) transducers no. 1 and 2 transmitting.

An analysis of the setup geometry was performed as illustrated in Figure 7.3 (a). It was revealed that the distance from the transducer edge facing the plate edge (Edge B on Figure 7.3), via the plate edge and back to the opposite transducer edge (Edge A) is approximately equal to an integer number of A_0 mode wavelengths. Since the wave phase is inverted on reflection from the plate edge, the reflected wave arrives at transducer Edge A in a phase opposite to the phase of the wave generated by this edge. Thus, destructive interference occurs between the wave transmitted from Edge A and the wave transmitted from Edge B and reflected from the plate edge. This causes the disappearance of the Lamb wave beam in the direction of the receiving transducer.

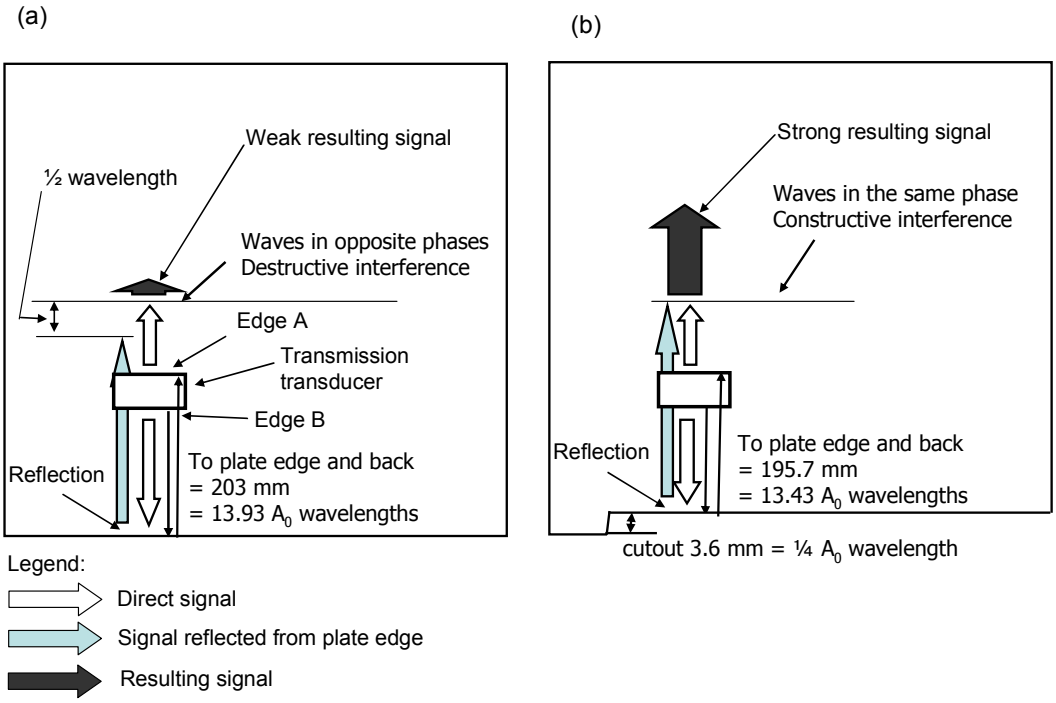

Figure 7.3. (a) Illustration of the geometric explanation of the beam disappearance due to destructive interference shown in Figure 7.2, (b) illustration of the plate geometry modification correcting the interference.

In order to prevent the destructive interference from taking place, a 3.6 mm-wide strip was cut from the reflecting plate edge, as shown in Figure 7.3 (b). This shortened the path of the reflected wave by one half of the wavelength, causing it to arrive at Edge A in phase with the wave generated by this edge. Subsequent laser vibrometer scans, shown in Figure 7.4, revealed a strong Lamb wave beam propagating in the direction of the reception transducers. This confirmed that the understanding of the phenomenon as well as the chosen solution were correct.

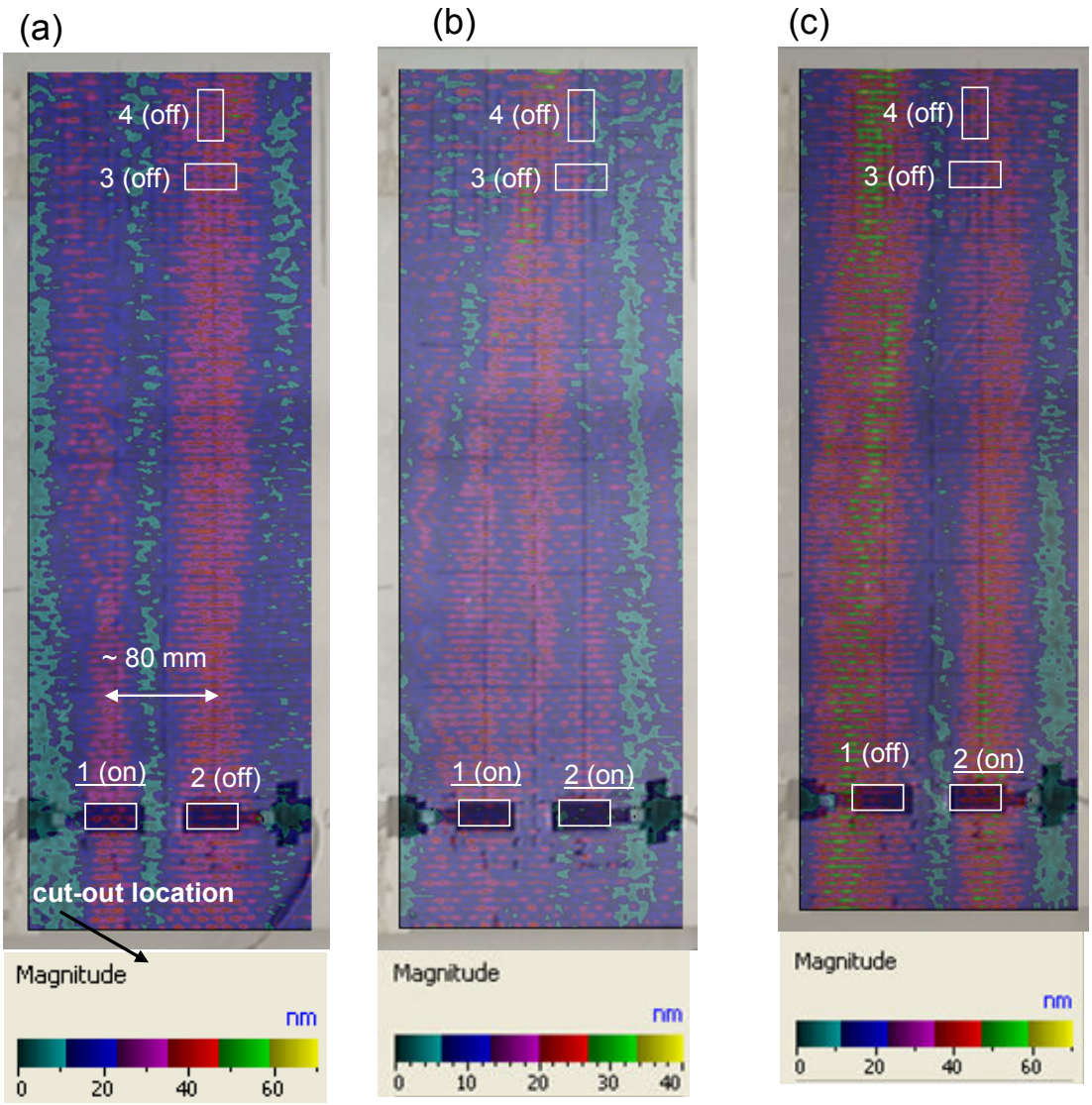

Figure 7.4. FTT laser vibrometer scans of a fragment of the experimental plate with a geometry modification – a 3.6 mm cut-out in the edge nearest to the transmission transducer. (a) transducer 1 is operating, (b) transducers 1 and 2 are operating, (c) transducer 2 is operating.

The scans shown in Figure 7.4 cover three transmission configurations. In Figure 7.4 (a) transducer no. 1 is transmitting and transducer no. 2 is turned off. The beam transmitted by the transducer has a maximum amplitude of approximately 35 nm. The beam repeats approximately 80 mm to the right, overlapping with transducer no. 2. It is expected that the beam repetition is a feature of the two-dimensional standing wave in this particular geometry of plate and transducer. In earlier tests (results shown in Figure 6.18), the repeating beams were offset by 120 mm and appeared over the entire plate area. In the measurement reported in this section, this offset is 80 mm. The author finds the geometry of the plate a likely cause of this difference. In particular, the length of plate edges in not equal (1000 mm in one direction and

821 in another). Thus, with transducers rotated by 90 ° in relation to the experiment shown in Figure 6.18), a different distance between the edges influenced the standing wave reported in the currently discussed experiment.

Since the scan does not cover a wider area, it is not possible to confirm whether the pattern repeats itself over the whole area of the plate. Based on the whole-plate scans shown in Chapter 6. , however, such a repetition appears likely. The maximum amplitude value is higher than that recorded in the earlier experiment with transducer no. 6 transmitting (22 nm). The reason for this difference was not identified. It can be speculated that it may be a feature of the standing wave in this particular geometry or that it is caused by an increase in the quality of the bond between the transducer and the plate.

Another effect which can be considered to explain the presence of the beam offset in relation to the operating transducer is the influence of the non-operating transducer. Quick Pack transducers were shown to exhibit multiple resonances appearing every several hundred Hz (see Figure 5.8). In the experiment reported here, the system was operating at one of such resonance frequencies in order to achieve optimum power transmission. Thus, it is possible that the non-driven transducer began resonating mechanically and contributed to the generation of the Lamb wave beam which passed through it. This possibility was not tested in the time allocated for this project.

In Figure 7.4 (b) both transducers no. 1 and 2 are transmitting. This arrangement results in a beam converging with distance from the transducer. Such behaviour is reminiscent of the beam steering and beam focusing capabilities of phased array transmitters. The maximum amplitude near the transducers is approximately 20 nm near the transmitting transducers and 30 nm in the vicinity of the reception transducers, where the two beams converge. The maximum amplitude is limited by the power rating of the signal generator, which is not sufficient to drive two transducers, each capable of drawing approximately 150 mW, concurrently at full power.

In Figure 7.4 (c) transducer no. 1 is turned off and transducer no. 2 is transmitting. The geometry of the standing wave pattern is similar to the situation in which transducer no. 1 was transmitting. The beam repeats itself approximately 80 mm to the left of the transmitting transducer. The maximum amplitude is approximately 50 nm.

7.4. Power transmission results

The power transmission measurement results for several combinations of Quick Pack transducers described in this Chapter are listed in Table 7.1. Contrary to what was expected the achieved power throughput values were not better than those recorded earlier with Quick Pack transducers facing the reception transducer with their shorter edge. With 0.15 mH inductive compensation only the 13.2 mW value achieved by the transducer no. 2 – transducer no. 3 pair exceeds the 11.9 mW recorded for the baseline pair of transducer no. 6 - transducer no. 5. With 0.69 mH inductive compensation only the transducer pair no. 1 – no. 4 achieved 11.6 mW power transmission, nearly matching the 12.7 mW result of the baseline configuration.

Table 7.1. Power transmission measurement results for various combinations of Quick Pack transducers. Transducer numbering as in Figure 7.1. Drive signal amplitude 20 Vpp.

Transmis-sion – reception transducers	0.15 mH			0.69 mH		
	Reception output power [mW]	Transmis-sion efficiency [%]	Frequency [kHz]	Reception output power [mW]	Transmis-sion efficiency [%]	Frequency [kHz]
1 – 3	5.1	4.2	72	5.3	5.2	35
1 – 4	6.5	5.6	72	11.6	14.3	35
2 – 3	13.2	11	95	2.7	3.3	30
2 – 4	3	2	73	5.6	10.3	35
2 – 3+4	10.4	8.4	95	n/d	n/d	n/d

7.5. Summary and discussion

A modified experimental setup using Quick Pack transmission transducers orientated to face the receiving transducer with their longer edge was tested. The chosen transducer orientation was based on the previously measured Lamb wave generation characteristics of these transducers. The transducers were found to emit stronger signals from their longer edges. This suggested that a higher power throughput could be achieved if the transmission transducers faced the reception transducer with their longer edge, thus emitting a stronger Lamb wave signal in the direction of the reception transducer.

Two transmission transducers located side by side were used. This allowed a comparison of the wave propagation patterns depending on the location of the transducer as well as of the concurrent operation of two transducers. Two reception transducers orientated perpendicularly to each other were also used. This allowed a comparison of the effect which the reception transducer orientation has on the power throughput of the system.

The Lamb wave standing wave pattern was imaged using a scanning laser vibrometer. The scan revealed that the particular location of the transducer caused destructive interference between Lamb waves emitted directly from one edge of the transducer and the reflected wave emitted by the opposite edge. This interference resulted in the disappearance of the wave beam in the direction of the reception

transducer. In order to remove this effect a 3.6 mm (quarter-A_0 wavelength) cut-out was made in the plate edge from which the reflection occurred. This shifted the phase of the reflected wave leading to constructive interference and resulting in a strong wave beam being propagated in the direction of the reception transducer.

The described phenomenon highlights an important difficulty in the design of the Lamb wave energy transmission system. The location of the transmission transducer must be precisely determined and realised in order to prevent a nearly complete cancellation of the transmitted wave due to destructive interference with reflected signals. Location inaccuracies on the order of millimetres can determine whether the system will operate or not due to an interference of the transmitted waves. This poses a significant difficulty in practical realisations of such a system. Manufacturing and assembly tolerances of structural parts as well as of the transducer positioning will have a significant effect on the system operability. Another effect that may need to be considered is the stress appearing in the aircraft structure due to it carrying operational loads. The author did not find relevant information in literature. In informal discussions however, the prevailing opinion was that the effect of operational stress will be negligible.

One way to mitigate this problem may be to use a transducer type with a sufficiently wide effective operation frequency range and an adaptive tuning system. Such a system could adjust the operating frequency and thus the Lamb wave wavelength until the destructive interference is removed in the particular structure. The Quick Pack transducer operates efficiently only within multiple narrow frequency ranges and therefore is not suited for such frequency tuning. The MFC transducer, on the other hand, has a relatively wide range of effective operation frequency and is suitable for tuning.

Subsequently, the concurrent operation of two transmission transducers positioned near each other was tested. The laser vibrometer scan of this test revealed an effect similar to that observed in phased array transducers. The two wave beams emitted by the transducers converged approximately 50 cm from the transducers. This indicates a beam focussing capability of such a two-transducer setup.

The power throughput of the setup was measured for several different combinations of the two transmission and two reception transducer units. In most configurations the power throughput was approximately 5 mW with 0.15 mH and 0.69 mH inductive compensation. This result was worse than in the previously tested

configuration with the transmission transducer facing the reception transducer with its shorter edge. Only in two configurations power throughputs of 13.2 and 11.7 mW, with 0.15 mH and 0.69 mH respectively, was recorded. Thus, the tested change in the transmission transducer orientation did not bring the expected improvement in the system's power throughput. This may be caused by the fact that the signal amplitude reaching the reception transducer was not, in fact, significantly higher than the amplitude of the received signal in the original configuration. In that configuration, while the transmission transducer faced the reception transducer with its longer edge, the latter was in fact positioned within one of the periodically repeating beams of high amplitude vibration which originated from the longer edge of the transmission transducer (see Figure 6.18). Thus, accidentally, the location of the reception transducer in the original configuration was optimal. These results emphasise the need to know the propagation pattern of the Lamb waves generated by the chosen transmission transducer before the location of the receiving transducer is chosen. Such knowledge can be obtained from a laser vibrometer scan. Further work with simulation methods may allow the prediction of the propagation pattern through computer simulation. Moreover, an adaptive frequency tuning system could enable the modification of the propagation pattern in such a way that the maximum amplitude signal would be directed at the location of the reception transducer.

7.6. Conclusion

The investigation of modifications of the ultrasonic energy transmission system described in this chapter indicated the high sensitivity of the system's performance to structure geometry changes. This observation highlights the need to individually assess the performance of such a system whenever it is applied to a new structure. A Lamb wave computer simulation tool allowing a time- and cost-efficient assessment of wave propagation in various structural geometries is therefore desirable. In the next chapter the LISA Lamb wave simulation software is evaluated. The code is used to model the simple plate geometry of the prototype energy transmission system described in this thesis. Several cases, previously investigated experimentally, are modelled. The comparison of experimental and simulation results is favourable, indicating the potential of the software in the development of Lamb wave-based systems.

Chapter 8. Lamb wave simulation with LISA software

8.1. Introduction

LISA (Local Interaction Simulation Approach) is a finite difference method software package developed for the simulation of acoustic wave propagation by Sheffield (UK) and AGH (Krakow, Poland) universities (Chetwynd 2008). The currently available version is capable of performing simulations of 3D geometries. It is designed to use a PC CUDA-type graphics processing unit (GPU) to perform calculations. In the author's experience using the GPU results in an approximately 60 times reduction of simulation run times in comparison to the same simulation performed using the PC's central processing unit (CPU). Characteristics of the software important to an engineering user are briefly described below.

Geometry

A geometric model of the simulated structure is discretised using cube elements. These elements have the same dimensions in each direction. The size as well as the shape of the elements is constant throughout the model. For Lamb wave simulation it is sufficient to define three layers of elements across the plate thickness. In the simulations described in this work elements with an edge length of 0.5 mm were used, which resulted in three layers in the 1.5 mm-thick plate model. Material properties – in this case of aluminium – were assigned to all elements forming the plate model. This structural model is automatically surrounded by at least one layer of elements with the material properties of air. In the software version used in this work the air interface is modelled as lossless, i.e. the acoustic vibration energy contained in the modelled structure is not dissipated. This characteristic becomes a problem in the simulation of continuous Lamb wave transmission, as it leads to a continuing increase of the simulated vibration amplitude. Such a result is in disagreement with experiment, where energy dissipation into the surrounding environment causes the vibration amplitude to stabilise at a constant level.

In the simulations described in this work the geometry input file was generated using a Matlab script. A separate programme allowing the user to import geometry from CAD software is available. It was not used due to the simplicity of the shape of the structure used.

Actuators

An actuator model can be assigned to each element of the geometry model. Two types of actuation are available:

- "Absolute" acts by forcing a displacement onto the element to which it is applied. It can therefore be used also to anchor the entire plate by specifying an actuator without motion.
- "Force" acts by adding the user specified actuating displacement to the motion of the element already taking place. The name "Force" is thus misleading, as the actuation also occurs through displacement. This type of actuator model most closely resembles the operation of a small piezoelectric actuator bonded to a large plate. It was therefore used in all simulations described in this text.

The actuating displacement can change in the time domain and is user specified. Commands exist allowing a straightforward definition of typical actuation functions (such as sine) and their envelopes (such as Hann window).

Simulation

Simulation is performed in constant time steps. The length of the time step and the duration of the simulation are set by the user. The time step used was 0.05 microseconds, which is a typically recommended value for the simulation of ultrasound in the investigated frequency range.

The material model and the simulation are linear. The actuating displacement is defined in arbitrary units of length and the simulated vibration response is returned in the same units. In simulations described in this work it was assumed that the arbitrary unit equalled one nanometre.

Data output

Two methods of data output exist:

- A "sensor" can be defined at any element of the model. This sensor will record the three displacement components in the time domain and save them in a file.
- A snapshot of the displacement field can be recorded at a specified time instant of the simulation. A post processing programme is available allowing the display of the recorded displacement field using a colour map. The size of the displacement field data files is large. In the case of the experimental plate model used (1000 x 821 x 1.5 mm) the data files were 500 MB in size. This limits the frequency at which such data snapshots can be collected.

8.2. Model description

Geometry

The models used in the simulation were made to resemble the experimental setup used throughout the project, as shown in Figure 8.1. The whole aluminium plate was modelled, with dimensions 1000 × 821 × 1.5 mm. The material properties of aluminium were taken from the LISA software materials library. Two versions of the model were built, one with the MFC M8528-P1 transducer and one with the Quick Pack QP10n transducer. The locations of these transducers were the same as of transducer units no. 8 and no. 6, respectively, in the experimental setup.

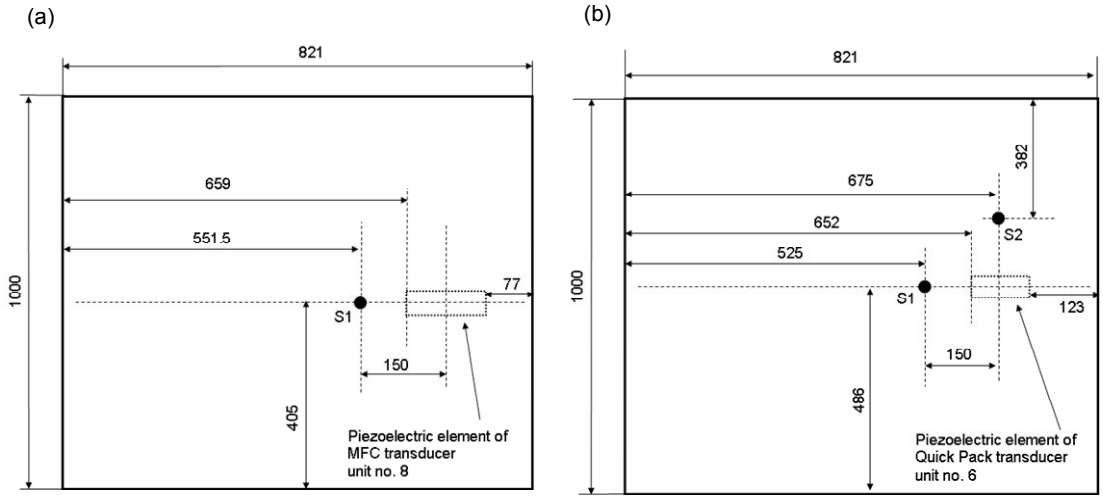

Figure 8.1. Geometries used in LISA models of a setup with (a) MFC M8528-P1 transducer, (b) Quick Pack QP10n transducer. S1 and S2 denote locations of simulated sensors at which time domain waveforms were recorded.

Sensors

Two locations of simulated displacement sensors were defined on the plate model. The locations were chosen to represent selected laser vibrometer measurement points used in the radial characterisation of the two transmitting transducers, as described in 6.4. (Figure 6.4). Sensor S1 represented the measurement point 1 from Figure 6.4. This point was located on the longitudinal axis of the transmitting transducer, in the direction of the reception transducer, 150 mm from the transducer centre. Sensor S1 was defined in both versions of the model, with both the MFC and the Quick Pack transducers. In addition, the model of the Quick Pack-based setup included sensor S2 representing measurement point 5 from Figure 6.4. This sensor location was chosen because the Quick Pack transducer

model was expected to transmit signals from both its shorter and longer edges. S2 was needed to measure the signal transmitted from the longer edge of the transducer.

Transducers

The patch transducers were modelled basing on the method described by Giurgiutiu (2005). This method, itself based on the work of Crawley (1990), comprises an analytical solution allowing the calculation of the distribution of the shear stress transferred from an operating patch transducer to the underlying structure surface. Giurgiutiu (2005) calculated stress distributions for several thicknesses of the epoxy bonding layer. The plot is reproduced in Figure 8.2. When a 100 μm-thick bonding layer is used, the stress is transferred over a large portion of the transducer surface, with magnitudes increasing gradually towards the edges of the transducer patch. In the case of thinner bonding layers – 10 μm or 1 μm – the shear transfer is confined only to narrow areas near the edges, with no shear transfer occurring over a majority of the transducer area.

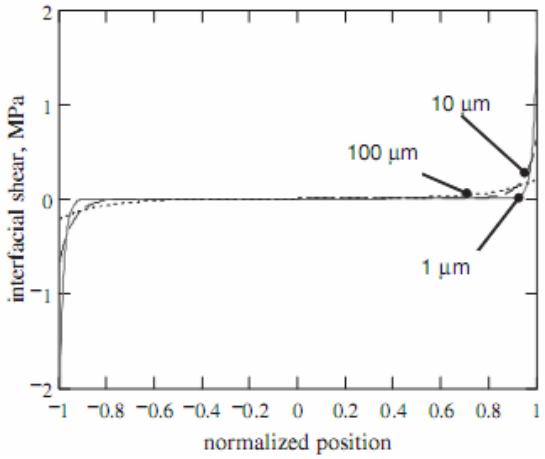

Figure 8.2. Distribution of shear stress transfer from patch transducer to 1 mm-thick aluminium plate. "Normalized position" refers to the transducer length. Graph reproduced from Giurgiutiu (2005).

The thicknesses of the transducer bonding layers in the experimental energy transmission setup were not known. For the purpose of the initial work with the LISA model it was assumed that the bonding layer was sufficiently thin to cause the concentration of the shear transfer near the transducer edges. This approach allowed the representation of patch transducers as oscillating lines representing transducer edges. In turn, the modelling task was significantly simplified. The simulation results, described in detail in subsequent section, matched the experimental

measurements well. In future work the measurement of the bonding layer may be undertaken in order to increase the simulation fidelity.

The model of the MFC M8528-P1 transducer is shown in Figure 8.3. Since this transducer deforms only along its longitudinal axis, it is modelled by two lines representing its shorter, oscillating edges. The lines are constructed of "Force"-type actuator points located at all elements within the length of the lines. When actuation is performed, the lines are made to oscillate in opposite phases.

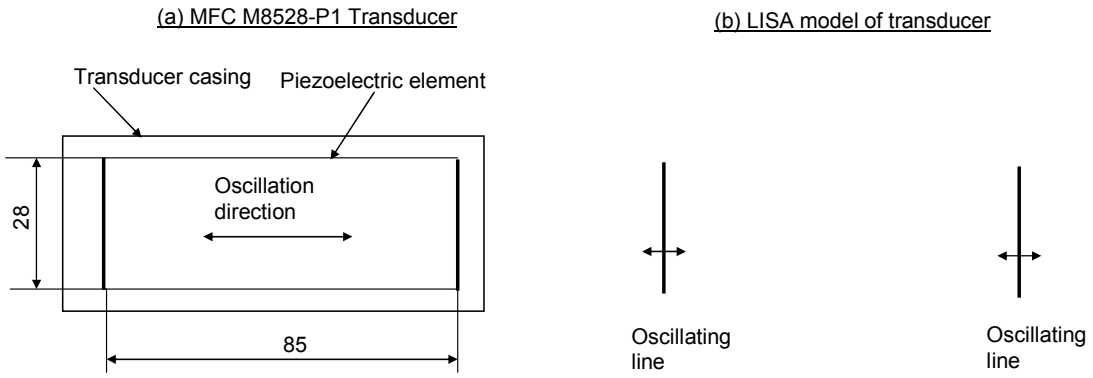

Figure 8.3. Sketch showing the way in which the LISA model of the MFC transducer (b) was derived from the transducer geometry (a).

The model of the Quick Pack QP10n transducer is shown in Figure 8.4. The quick pack transducer deforms both in the longitudinal and transverse directions. Therefore its LISA model is constructed from two pairs of lines representing all four edges of the transducer. The lines are built of "Force"-type actuator points. Opposing edges are made to oscillate in opposite phases.

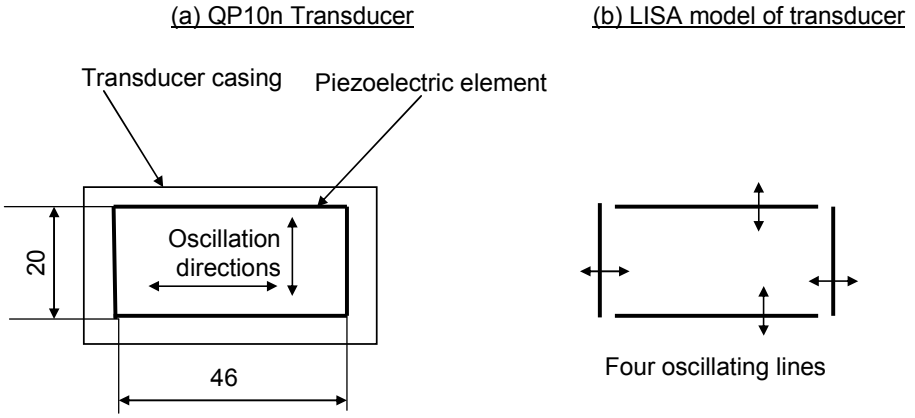

Figure 8.4. Sketch showing the way in which the LISA model of the QP10n transducer (b) was derived from the transducer geometry (a).

8.3. Results: Transmission transducer characteristics

A series of simulations modelling the operation of the transmission transducer driven by a signal pulse was performed. These simulations replicated the experiment described in Section 6.4, in which the directional transmission characteristics of the transducers were measured.

Sensor points defined on the plate model were used to record time domain waveforms of the out-of-plane displacement. The simulated waveforms were subsequently compared with waveforms recorded in the same locations experimentally. The actuator models were oscillated with a five-cycle signal pulse in a Hann window envelope, which modelled the signal used in the experiment. The amplitude of the simulated drive oscillation was set to 1 unit, assumed to be 1 nanometre. The resulting displacement was then assumed to be expressed in nanometres.

The experimental waveform used in the comparison was recorded while the transducer was placed in a circuit with 0.15 mH inductive compensation and driven with a signal with the maximum amplitude of 20 Vpp.

MFC M8528-P1

The simulation was performed using a five-cycle pulse at 180 kHz frequency in a Hann window as the transducer drive signal. This frequency was in the middle of the range investigated with laser vibrometry and was also the frequency of the highest power transmission recorded with 0.15 mH inductive compensation. It was, therefore, considered representative. The simulated waveforms were recorded at sensor location S1, as shown in Figure 8.5.

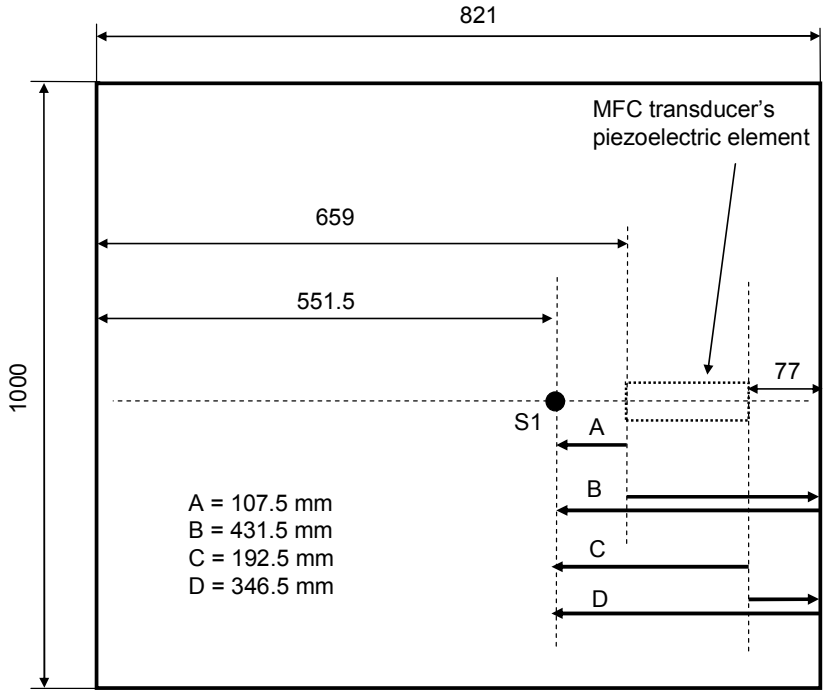

Figure 8.5. Signal paths considered in the analysis of the simulated and experimental Lamb wave waveform generated by the MFC M8528-P1 transducer. All dimensions and path lengths are in millimetres. Arrows illustrating the paths were shifted off the transducer centreline for clarity. Location of sensor S1 also shown.

In order to allow a detailed analysis of the simulated and experimental waveforms, several paths of direct and reflected signals were identified. Time-of-flight values along these paths were calculated for the A_0 and S_0 modes, as shown in Table 8.1.

Table 8.1. Times of flight of Lamb waves generated by MFC M8528-P1 transducer along paths shown in Figure 8.5

	path name ->		A	B	C	D
	path length [mm] ->		107.5	431.5	192.5	346.5
f (kHz)	mode	group velocity [m/s]	Time of flight [μs]			
180	A0	2533.42	42	170	76	137
180	S0	5420.96	20	80	36	64

The simulated and experimental out-of-plane displacement waveforms are shown in Figure 8.6. The amplitude of the simulated signal was scaled with a factor of 0.2822 in order to match the amplitude of the experimentally measured waveform.

The frequency of the signal is the same in experiment and simulation, indicating a correct choice of time step units and drive frequency in the simulation. The general shape of the simulated signal envelope also matches the experimental result. There are differences between the times of pulse arrival between simulation and experiment. These can be attributed to the following factors:

- A measurement error of the signal path length and other geometric inaccuracies between the model and the experimental setup
- Inaccuracy of the assumed transducer model
- A difference between the real and simulated material properties.

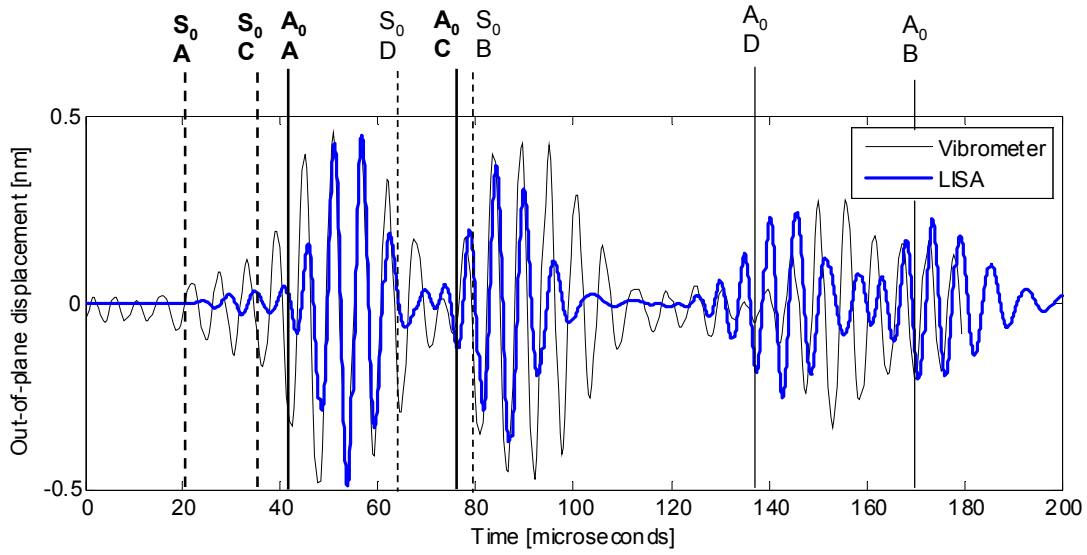

Figure 8.6. Simulated and experimental Lamb wave out-of-plane displacement waveforms generated by the MFC M8528-P1 transducer location and recorded at S1 sensor location. Pulse arrival times indicated. Arrival times of signals propagating via direct paths are marked in bold typeface. Simulated waveform amplitude scaled with a factor of 0.2822 to match experiment.

The two waveforms shown in Figure 8.6 were shifted in time in order to overlap the times of arrival of the A_0 signal along path A. This assumption was made in order to reference the two waveforms according to the strongest recorded signal. The required time shift was 15 μs. Before it was added, the simulated signal arrived before the experimental one. This shift was attributed to the influence of the arbitrarily chosen waveform recording trigger point set in the laser vibrometer measurement. It was therefore not considered an indicator of a fundamental error in the simulation or experiment.

In both waveforms the arrivals of the A_0 modes from both transducer edges, via the direct paths A and C, can be easily distinguished. This indicates that during the

short, five-cycle pulse the MFC transducer does not generate a Lamb wave as a whole. Instead, its two opposite edges act as individual wave generators. This observation confirms that the assumed method of modelling the transducer as two oscillating edges in which the entire stress transfer is concentrated is correct.

The S_0 waveform arriving via the shortest direct path A can be identified. The S_0 signal arriving via the longer direct path C (from the far edge of the transducer) overlaps with it. The overall shape of the simulated S_0 waveform is similar to the experimental one, although the simulated amplitude is smaller.

The reflected A_0 waveforms arrive approximately at the expected times, although the simulation-experiment difference is more pronounced due to the larger path length. The reflected S_0 waveforms are obscured by the stronger A_0 signals.

The assumed amplitude scaling factor of 0.2822 implies that simulated transducer oscillation amplitude of 0.2822 nm is required to generate a signal whose amplitude matches experiment. This suggests that the experimental transducer also oscillates with a similar amplitude. It should be noted that, since the simulation does not take the influence of the bonding layer and of the entire transducer area into consideration, the real oscillation amplitude may differ from that derived from simulation.

The simulated in-plane and out-of-plane displacement waveforms were plotted in Figure 8.7. The previously derived amplitude scaling factor of 0.2822 was used for both waveforms.

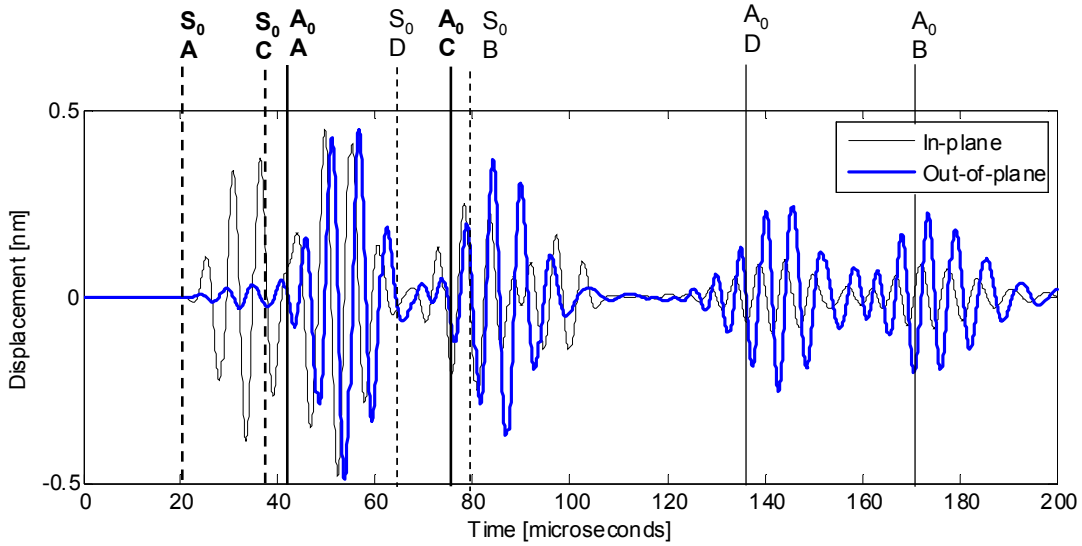

Figure 8.7. Simulated in-plane and out-of-plane displacement amplitudes of Lamb wave signal generated by MFC M8528-P1 transducer and recorded at sensor S1 location. Both signal amplitudes scaled with a factor of 0.2822, based on simulation-experiment comparison from Figure 8.6.

In Table 8.2 a comparison between in-plane and out-of-plane Lamb wave amplitudes, as calculated by the Disperse software and obtained from the LISA simulation is shown. The in-plane / out-of-plane amplitude ratio of the S_0 mode is comparable in both LISA and Disperse data. This further confirms that the LISA simulation produces correct results. In the case of the A_0 mode the LISA-predicted in-plane / out-of-plane proportion is nearly two times larger than the Disperse result. This can be explained by the fact that in the LISA result the A_0 mode waveform overlaps with a reflected S_0 mode waveform. This increases the in-plane vibration amplitude and, consequently, the measured in-plane / out-of-plane proportion.

Table 8.2. Comparison of proportions between in-plane and out-of-plane vibration amplitudes in A_0 and S_0 modes: generated by the LISA simulated MFC transducer and calculated by Disperse software

	MFC M8528-P1 180 kHz at sensor S1			
	A_0 mode		**S_0 mode**	
	Disperse	**LISA**	**Disperse**	**LISA**
in-plane amplitude [nm]	n/a	3.02	n/a	2.5
out-of-plane amplitude [nm]	n/a	3.34	n/a	0.24
in-plane / out-of-plane ratio	0.46	0.90	12.44	10.55

Figure 8.8 and Figure 8.9 show snapshots of the out-of-plane and in-plane displacement, respectively, over the area of the simulated plate. The in-plane image shows only the x-axis component of the displacement. The snapshot was taken at 60 μs into the simulation, approximately at the time of the A_0 mode passage through sensor S1. On both images the direct and reflected waves of both modes can be seen. The different proportions between the in-plane and the out-of-plane displacement amplitudes of both modes are also visible. Wavelengths of both modes were measured. The results were comparable with theoretical values, to the extent allowed by the accuracy of measurement allowed by the images:

- 38 mm for the S_0 mode, against 32 mm theoretical value
- 9 mm for the A_0 mode, against 8.3 mm theoretical value

These results further confirm the accuracy of the simulation.

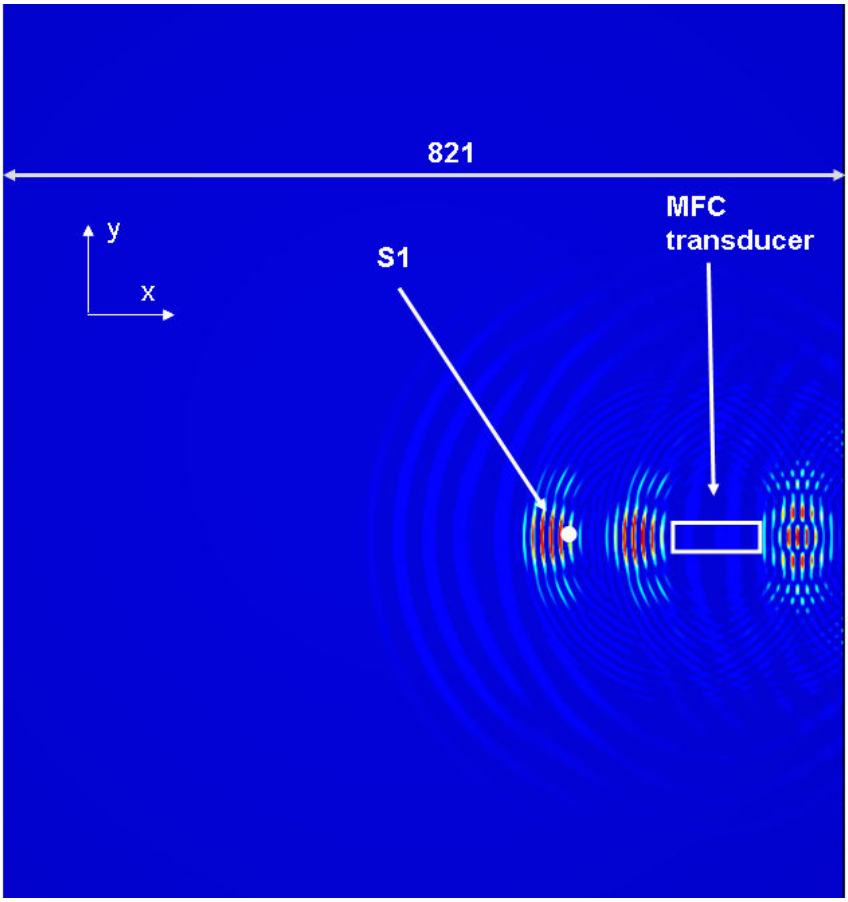

Figure 8.8. Out-of-plane displacement snapshot taken 60 μs into the simulation of the five-cycle pulse operation of the MFC M8528-P1 transducer. Both S_0 mode (longer wavelength) and A_0 mode (shorter wavelength) waves visible. Entire 821 mm width of the plate shown. Image cropped at top and bottom. Colour scale is not generated by the current version of software. The displacement units in which the results are presented are the same as those used in defining the actuators (in case of this work – nanometres).

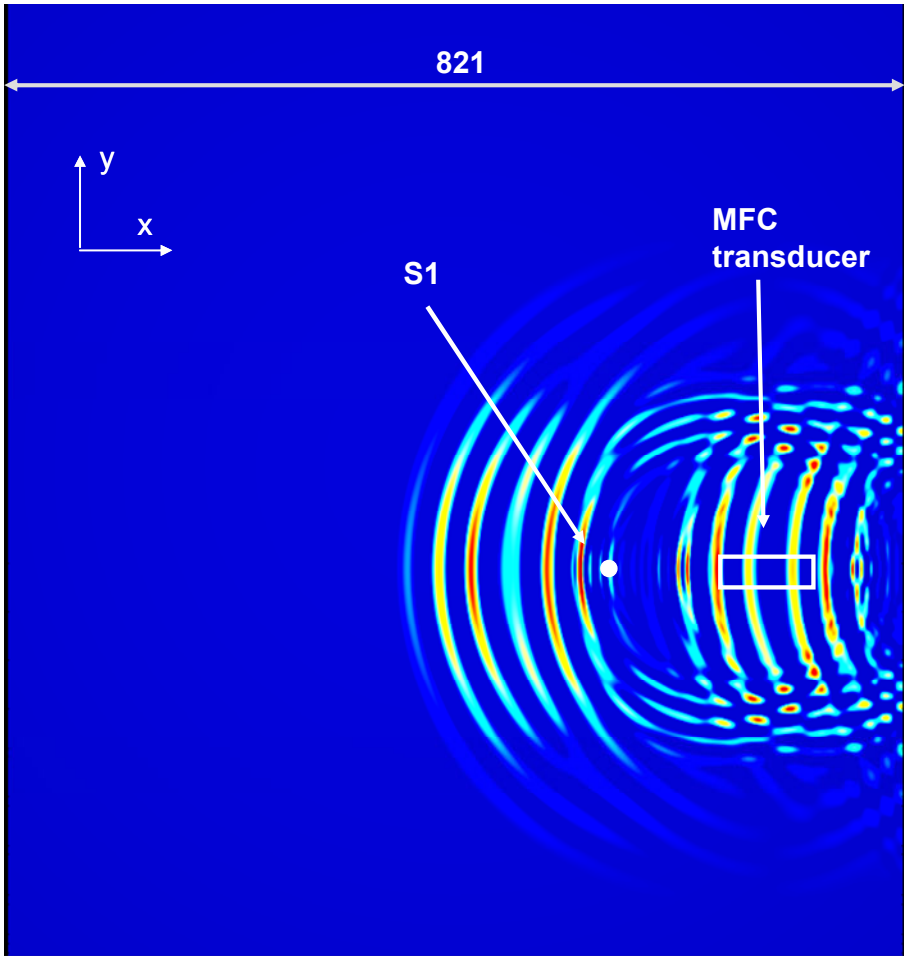

Figure 8.9. In-plane displacement x-axis component snapshot taken 60 μs into the simulation of the five-cycle pulse operation of the MFC M8528-P1 transducer. Both S0 mode (longer wavelength) waves are clearly visible. Shorter wavelength A_0 mode can be discerned in the vicinity of the S1 sensor. Entire 821 mm width of the plate shown. Image cropped at top and bottom. Colour scale is not generated by the current version of software. The displacement units in which the results are presented are the same as those used in defining the actuators (in case of this work – nanometres).

Quick Pack QP10n

The simulation was performed using a five-cycle signal pulse at 65 kHz frequency in a Hann window as the transducer drive signal. The frequency was in the middle of the range investigated with laser vibrometry and was also the frequency of the highest power transmission recorded with 0.15 mH inductive compensation. It was, therefore, considered representative. The simulated waveforms were recorded at sensor locations S1 and S2, as shown in Figure 8.10. The experimental waveform was recorded while the transducer was placed in a circuit with 0.15 mH inductive compensation and driven with a signal with the maximum amplitude of 20 Vpp. The signal consisted of five cycles in a Hann window.

Several paths of direct and reflected signals were identified. Time-of-flight values along these paths were calculated for the A_0 and S_0 modes, as shown in Table 8.3.

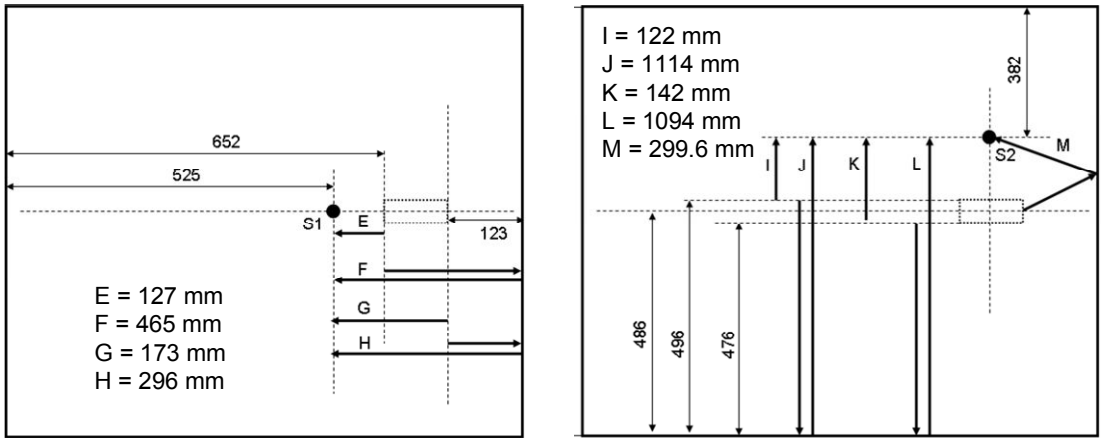

Figure 8.10. Signal paths considered in the analysis of the simulated and experimental Lamb wave waveform generated by the Quick Pack QP10n transducer. All dimensions and path lengths are in millimetres. Arrows illustrating the paths were shifted off the transducer centreline for clarity. Location of sensors S1 and S2 also shown.

Table 8.3. Times of flight of Lamb waves generated by Quick Pack transducer along paths shown in Figure 8.10

	path name ->		E	F	G	H	I	J	K	L	M
	path length [mm] >		127	465	173	296	122	1114	142	1094	299.6
f (kHz)	**mode**	**group velocity [m/s]**	**Time of flight [µs]**								
65	**A0**	**1772.51**	72	262	98	167	69	628	80	617	169
65	**S0**	**5436.02**	23	86	32	54	22	205	26	201	55

The simulated and experimental out-of-plane displacement waveforms recorded at sensor S1 are shown in Figure 8.11. These waveforms represent the signal generated by the shorter edges of the transducer. The amplitude of the simulated signal was scaled with a factor of 2.1035 in order to match the amplitude of the experimentally measured waveform. Figure 8.12 shows the waveforms recorded at sensor location S2 and corresponding to the signal generated by the longer transducer edge. The simulated waveform from sensor S2 was scaled using the same factor.

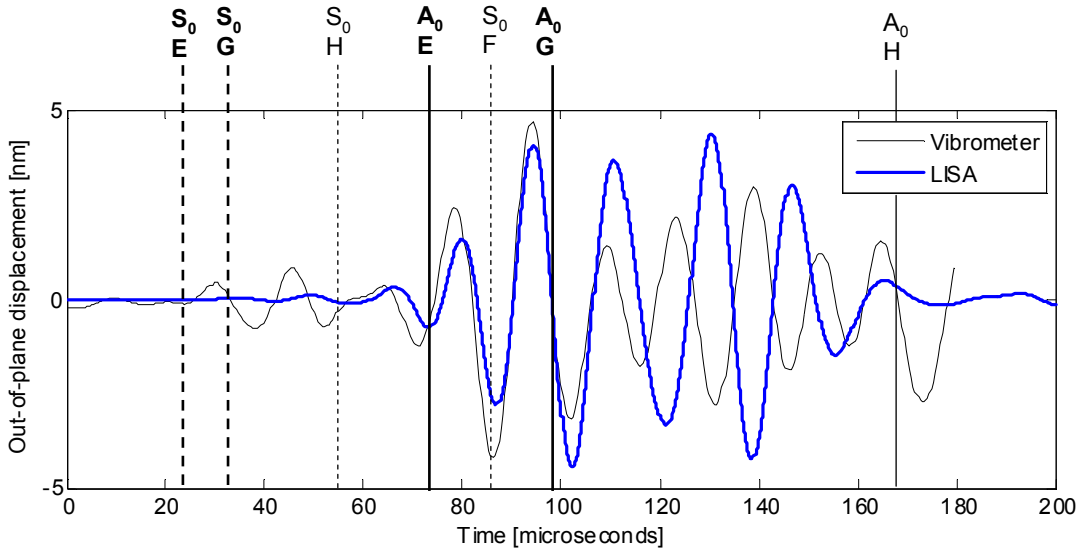

Figure 8.11. Simulated and experimental Lamb wave out-of-plane displacement waveforms generated by the Quick Pack QP10n transducer location and recorded at S1 sensor location. Arrival times indicated. Arrival times of signals propagating via direct paths are marked in bold typeface. Simulated waveform amplitude scaled with a factor of 2.1035 to match experiment.

Both simulated waveforms agree with the corresponding measured signals up to the point of arrival of the A_0 mode via the G path (sensor S1, Figure 8.11); and up to the end of the A_0 mode pulse (sensor S2, Figure 8.12). At and beyond these points multiple direct and reflected waves pass through the sensor location. Even small differences between the simulated and experimental characteristics of these individual waves can add and result in significantly different shapes of the resulting simulated and experimental waveforms.

The same amplitude scaling factor of 2.1035 was used for both simulated waveforms, recorded at sensor S1 and sensor S2. The amplitude of the simulated wave generated by the longer transducer edge was approximately three times larger than the amplitude of the simulated wave generated by the shorter edge. This shows that the assumed transducer model is accurate with respect to the amplitude of generated signals.

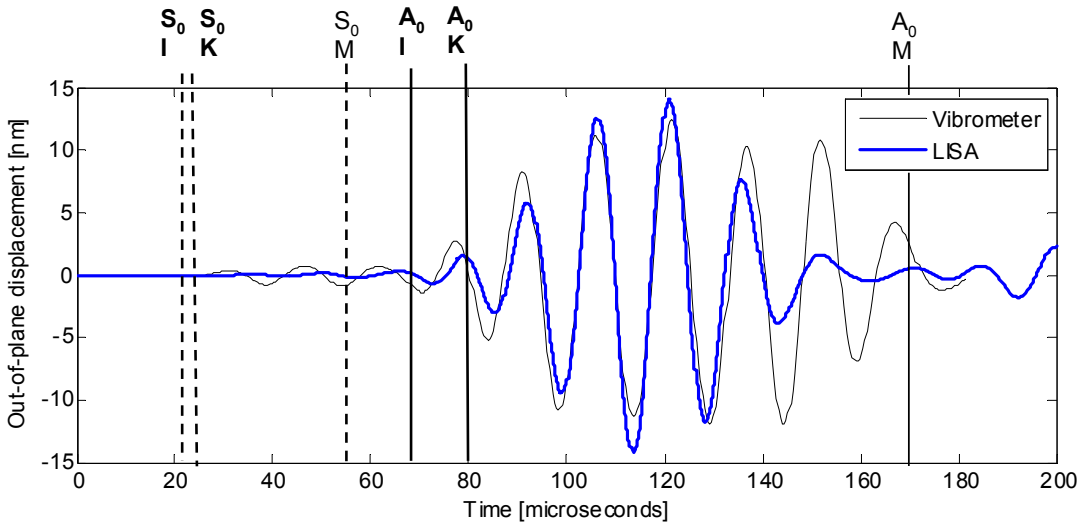

Figure 8.12. Simulated and experimental Lamb wave out-of-plane displacement waveforms generated by the Quick Pack QP10n transducer location and recorded at S2 sensor location. Arrival times indicated. Arrival times of signals propagating via direct paths are marked in bold typeface. Simulated waveform amplitude scaled with a factor of 2.1035 to match experiment.

Figure 8.13 and Figure 8.14 compare the simulated in-plane and out-of-plane waveforms recorded at sensor locations S1 and S2 respectively. The in-plane / out-of-plane amplitude proportion of the S_0 mode is comparable in both the LISA and the Disperse data (Table 8.4). A similar comparison for the A_0 mode is not possible due to an overlap of multiple modes at the point of the A_0 arrival.

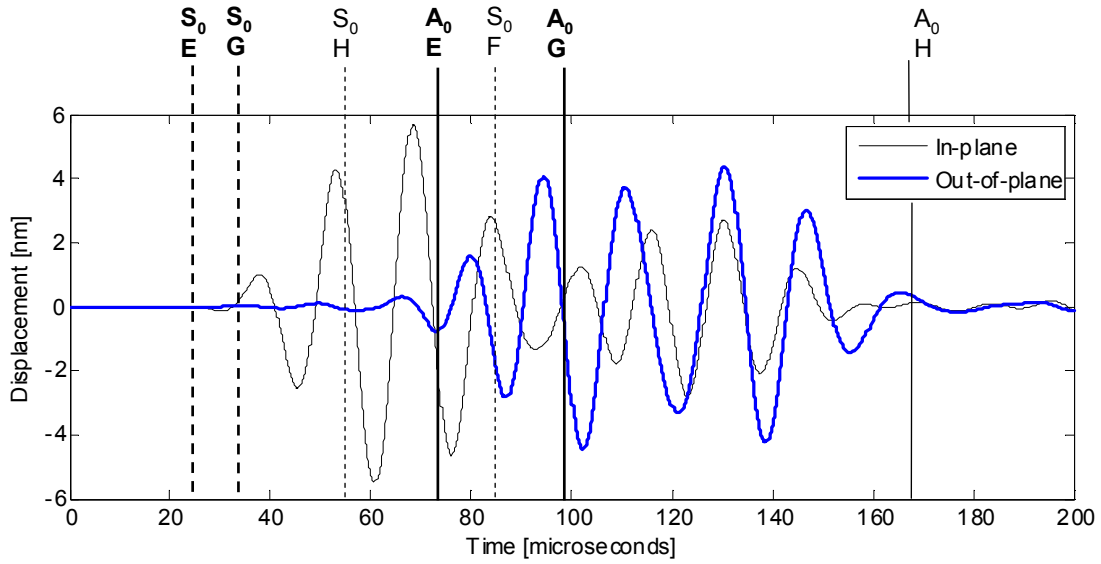

Figure 8.13. Simulated in-plane and out-of-plane displacement amplitudes of Lamb wave signal generated by Quick Pack QP10n transducer and recorded at sensor S1 location. Both signal amplitudes scaled with a factor of 2.1035.

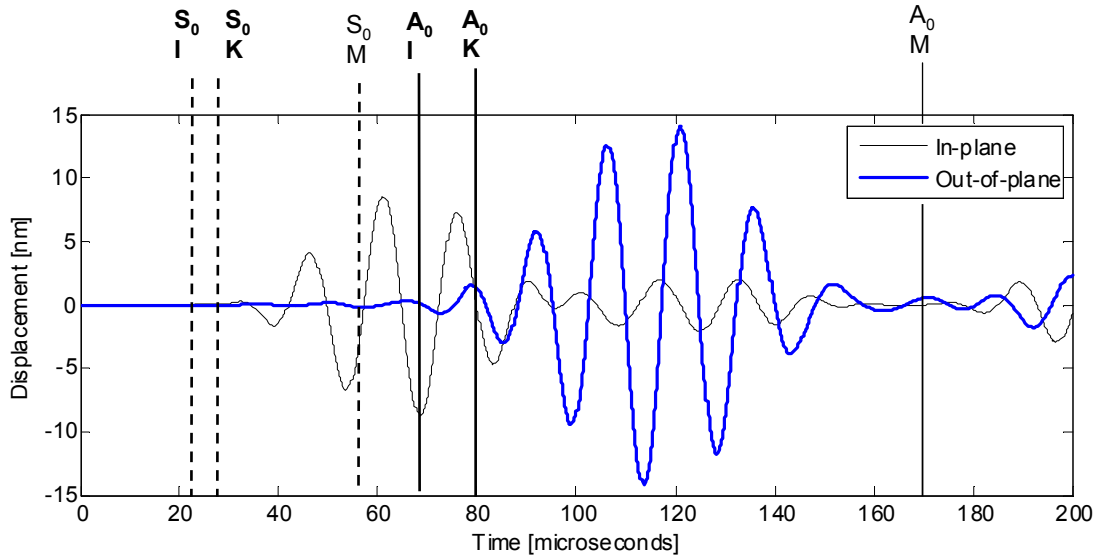

Figure 8.14. Simulated in-plane and out-of-plane displacement amplitudes of Lamb wave signal generated by Quick Pack QP10n transducer and recorded at sensor S2 location. Both signal amplitudes scaled with a factor of 2.1035.

Table 8.4. Comparison of proportions between in-plane and out-of-plane vibration amplitudes in A0 and S0 modes: generated by the LISA simulated Quick Pack QP10n transducer and calculated by Disperse software

	Quick Pack QP10n 65 kHz		
	S_0 mode at sensor S1		S_0 mode at sensor S2
	Disperse	LISA	LISA
in-plane amplitude [nm]		4.28	8.53
out-of-plane amplitude [nm]		0.12	0.23
in-plane / out-of-plane ratio	34.80	34.78	36.91

Figure 8.15 and Figure 8.16 show snapshots of the out-of-plane and in-plane displacement, respectively, over the area of the simulated plate. The in-plane image shows only the x-axis component of the displacement. The snapshot was taken at 80 μs into the simulation, approximately at the time of the A_0 mode passage through sensor S1. The transmission in both x and y directions, characteristic of the Quick Pack transducer, can be clearly seen. The interference of direct and reflected S_0 mode waves is visible in the in-plane displacement image. The different proportions between the in-plane and the out-of-plane displacement amplitudes of both modes are also visible. Wavelengths of both modes were measured. The results were comparable with theoretical values, to the extent allowed by the accuracy of measurement of the images:

- 73 mm for the S_0 mode, against a 83.7 mm theoretical value
- 16 mm for the A_0 mode, against a 14.6 mm theoretical value

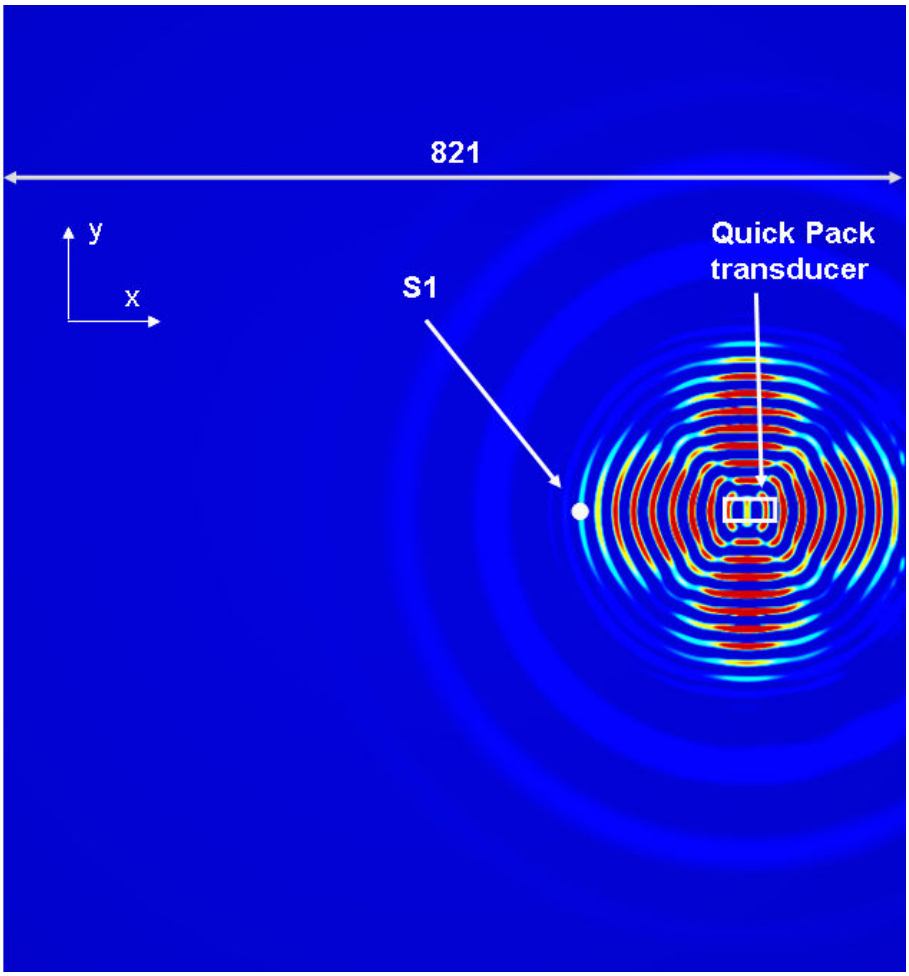

Figure 8.15. Out-of-plane displacement snapshot taken 80 µs into the simulation of the five-cycle pulse operation of the Quick Pack QP10n transducer. Both S0 mode (longer wavelength) and A0 mode (shorter wavelength) waves visible. Entire 821 mm width of the plate shown. Image cropped at top and bottom. Colour scale is not generated by the current version of software.

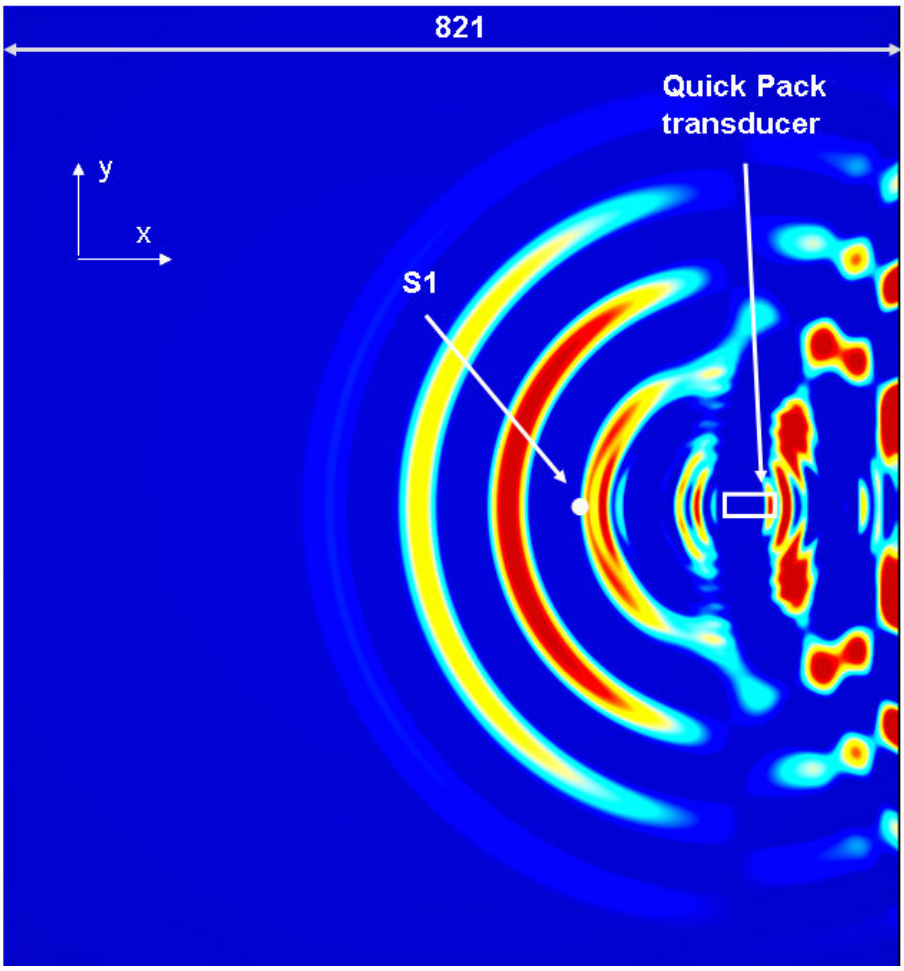

Figure 8.16. In-plane displacement x-axis component snapshot taken 80 μs into the simulation of the five-cycle pulse operation of the Quick Pack QP10n transducer. Both S0 mode (longer wavelength) waves are clearly visible. Shorter wavelength A0 mode can be discerned in the vicinity of the S1 sensor. Entire 821 mm width of the plate shown. Image cropped at top and bottom. Colour scale is not generated by the current version of software.

8.4. Results: propagation of continuous Lamb wave signal

Simulations of Lamb wave propagation generated by continuously driven transducers were performed. These simulations were designed to repeat the intended continuous operation of the ultrasonic energy transmission system. The geometry and actuator models used were the same as those described in the preceding section. One sensor point was placed at a 500 mm distance from the transmission transducer in the direction of the reception transducer. This sensor location corresponded to the location of a laser vibrometer measurement point used in an experiment in which continuously propagating waveforms were recorded.

MFC M8528-P1

In this experiment, the MFC transducer was driven with a 20 Vpp signal in a circuit with 0.15 mH inductive compensation at 181 kHz. In simulation the driving oscillation of the transducer model had an amplitude of 1 unit (assumed to be nm). The frequency was 180 kHz. Figure 8.17 shows a comparison of the experimental (a) and simulated (b) waveforms. The magnitude of the experimental waveform is expressed in terms of out-of-plane velocity. Velocity is the standard data format of laser vibrometer time domain measurements. In this case the conversion to out-of-plane displacement was not deemed necessary, as the main objective of the task was to compare the envelope shapes of the experimental and simulated waveforms. In the experimental waveform (Figure 8.17 (a)), a comparatively large amplitude is visible before the signal start and subsequently superimposed on the signal envelope.

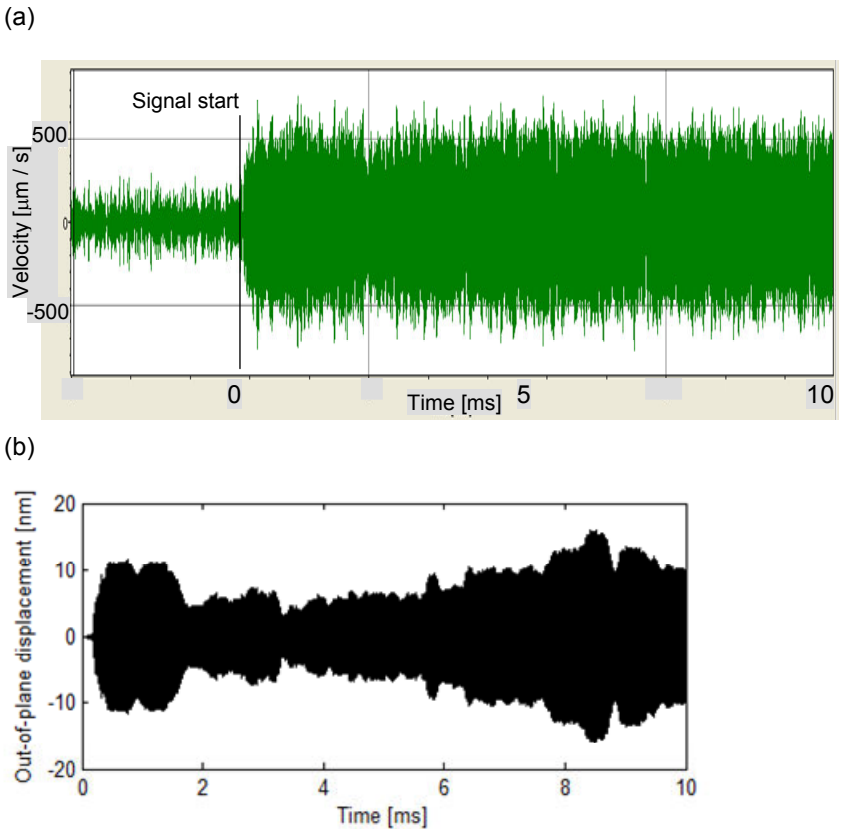

Figure 8.17. Comparison of out-of-plane vibration signals recorded during a continuous operation of an MFC M8528-P1 transducer at a point 500 mm from the transducer. (a) experimental out-of-plane velocity signal (large proportion of noise is visible before signal start and superimposed onto signal envelope) (b) simulated out-of-plane displacement signal. Time scales adjusted to match.

The experimental and simulated envelope shapes showed in Figure 8.17 do not match. In the experiment, the signal achieves a stable amplitude after approximately 3 ms. In the simulation, the signal amplitude varies throughout the 10 ms simulation time.

The oscillation is believed to be caused by two factors (Paćko 2013):

- The numerical dispersion of the simulation causes the wavelength of the simulated wave to change minutely as it propagates and reflects from plate edges. As interference occurs between multiple direct and reflected waves, the resulting small wavelength differences result in an occurrence of beat, seen as a variation of amplitude on time domain waveforms
- The simulation solver used does not model energy loss to the surrounding air. Thus a continuous excitation by a simulated transducer results in a continuing increase of the signal amplitude due to a build-up of energy in the plate model.

Figure 8.18 and Figure 8.19 show snapshots of the out-of-plane and in-plane (x-axis component) displacement taken 10 μs into the simulation. The exact vertical position of the transducer on the image could not be determined due to cropping. (It is deliberately not adjusted to lie on one of the vibration beams.) Both images show beams of vibration repeating along the vertical y axis. This pattern differs from experiment, where only one beam of vibration along the transducer axis was observed (Figure 6.14). The difference is believed to be caused by the fact that the simulation does not model signal losses on reflection and propagation.

The wavelength measured on Figure 8.18 is 9 mm, which corresponds to the A_0 mode wavelength at 180 kHz. The image should therefore be interpreted as a snapshot of moving A_0 mode waves passing under an envelope of a partial standing wave which, according to the FFT laser vibrometer image shown in Figure 6.15 has a wavelength of 4 mm. The in-plane displacement image shows a two-dimensional pattern. It should be noted that the image shows only the horizontal x-axis component of the in-plane motion. The addition of the y-axis component, not shown in Figure 8.19 will further complicate the pattern.

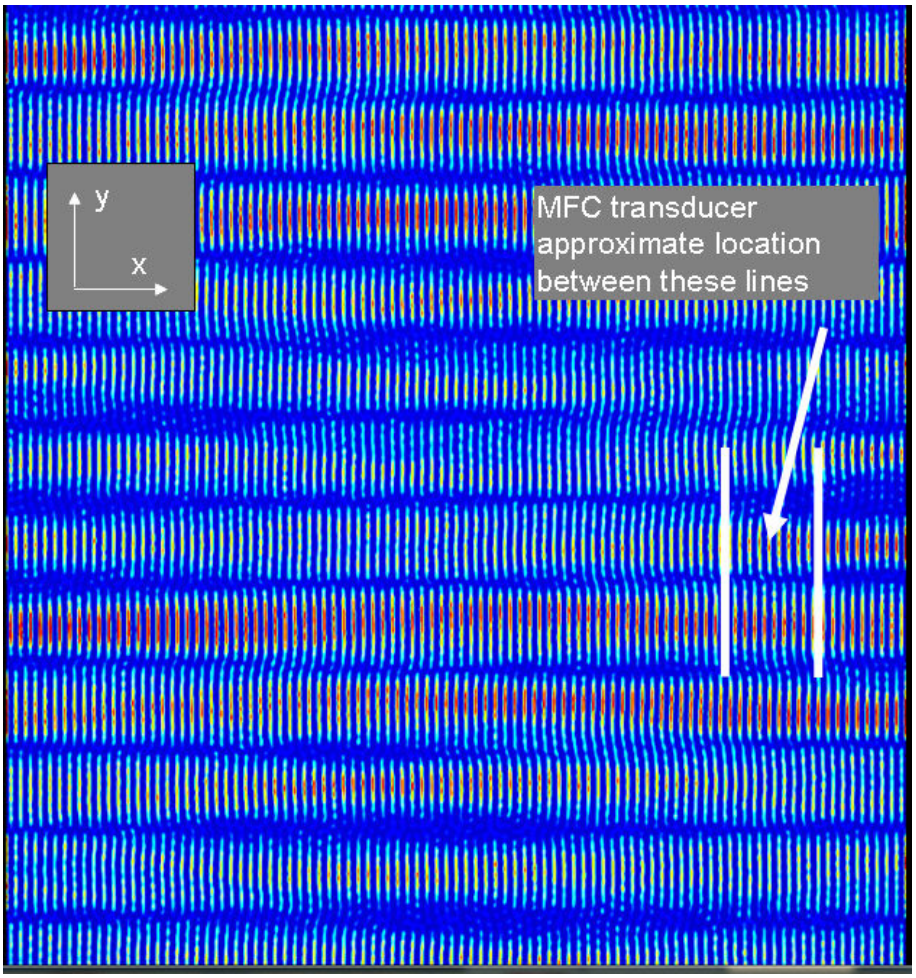

Figure 8.18. Snapshots of simulated out-of-plane displacement. Vibration is continuously transmitted by an MFC M8518-P1 transducer model. Snapshots taken 10 ms into simulation.

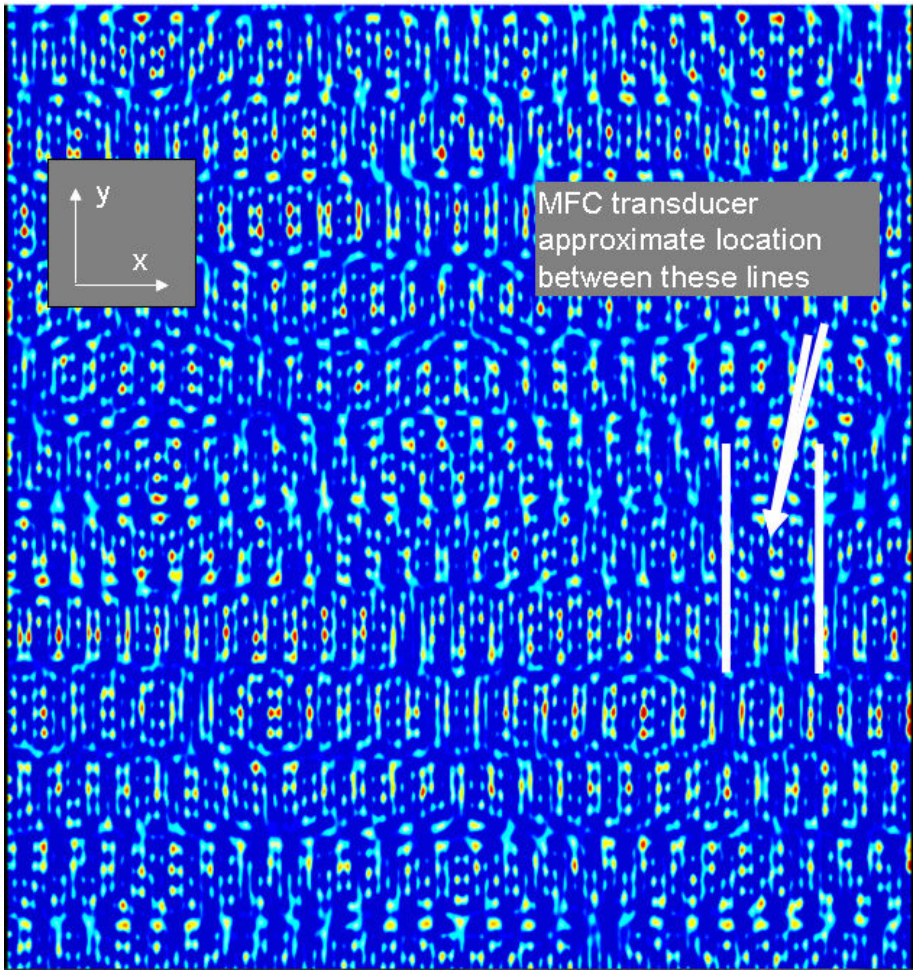

Figure 8.19. Snapshots of simulated in-plane x-axis component displacement. Vibration is continuously transmitted by an MFC M8518-P1 transducer model. Snapshots taken 10 ms into simulation.

Quick Pack QP10n

In this experiment, the QP10n transducer was driven with a 20 Vpp signal in a circuit with 0.15 mH inductive compensation at 65 kHz. In simulation the driving oscillation of the transducer model had an amplitude of 1 unit (assumed to be nm). The frequency was 65 kHz. Figure 8.20 shows a comparison of the experimental (a) and simulated (b) waveforms. As in the case of the MFC transducer, the simulated waveform contains amplitude oscillation not found in experiment. Similarly, this is thought to be a limitation of the simulation method used.

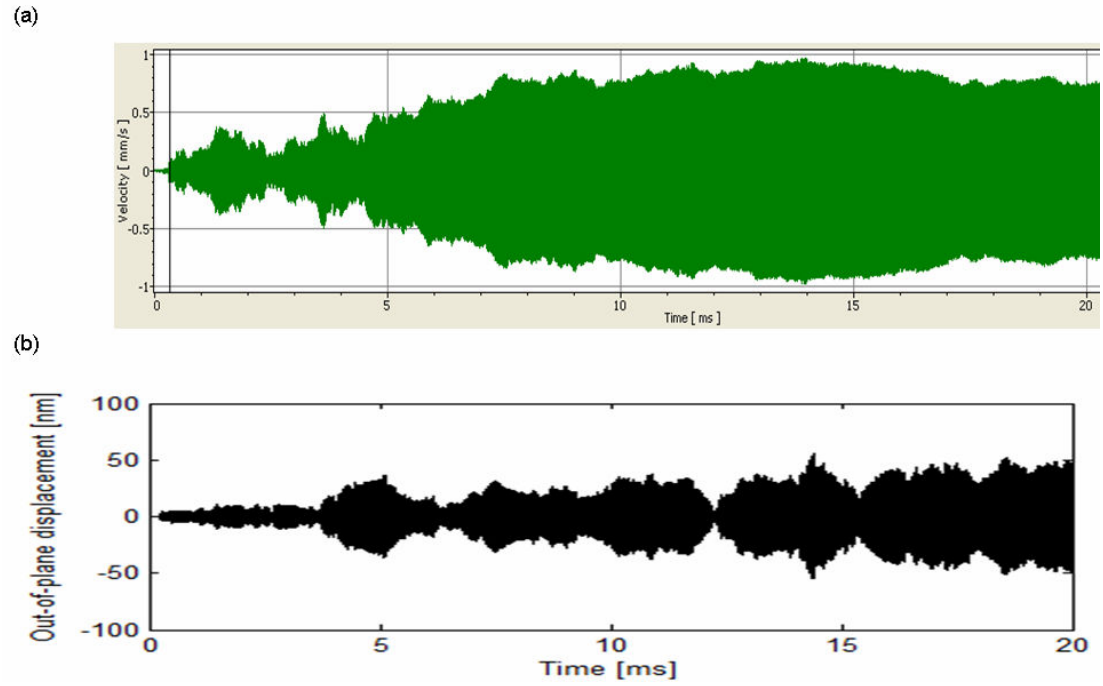

Figure 8.20. Comparison of out-of-plane vibration signals recorded during a continuous operation of an Quick Pack QP10n transducer at a point 500 mm from the transducer. (a) experimental out-of-plane velocity signal (b) simulated out-of-plane displacement signal. Time scales adjusted to match.

Figure 8.21 and Figure 8.22 show snapshots of the out-of-plane and in-plane (x-axis component) displacement taken 20 μs into the simulation. The exact vertical position of the transducer on the image could not be determined due to cropping. The out-of-plane image in Figure 8.21 shows a two-dimensional pattern with a period of 17 mm in both directions. This, within the accuracy of the measurement, can be interpreted to correspond to the theoretical A_0 mode wavelength of 14.6 mm. The image should, therefore, be interpreted as a snapshot of moving A_0 mode waves passing under an envelope of a partial standing wave which, according to FFT laser vibrometer image shown in Figure 6.19 has a wavelength of approximately 8 mm.

The in-plane image in Figure 8.22 shows a pattern of waves with a wavelength of 83 mm, which corresponds to the theoretical S_0 mode wavelength of 83.7 mm. Similarly, the image should be interpreted as a snapshot of a moving S_0 mode wave passing under an envelope of a partial standing wave.

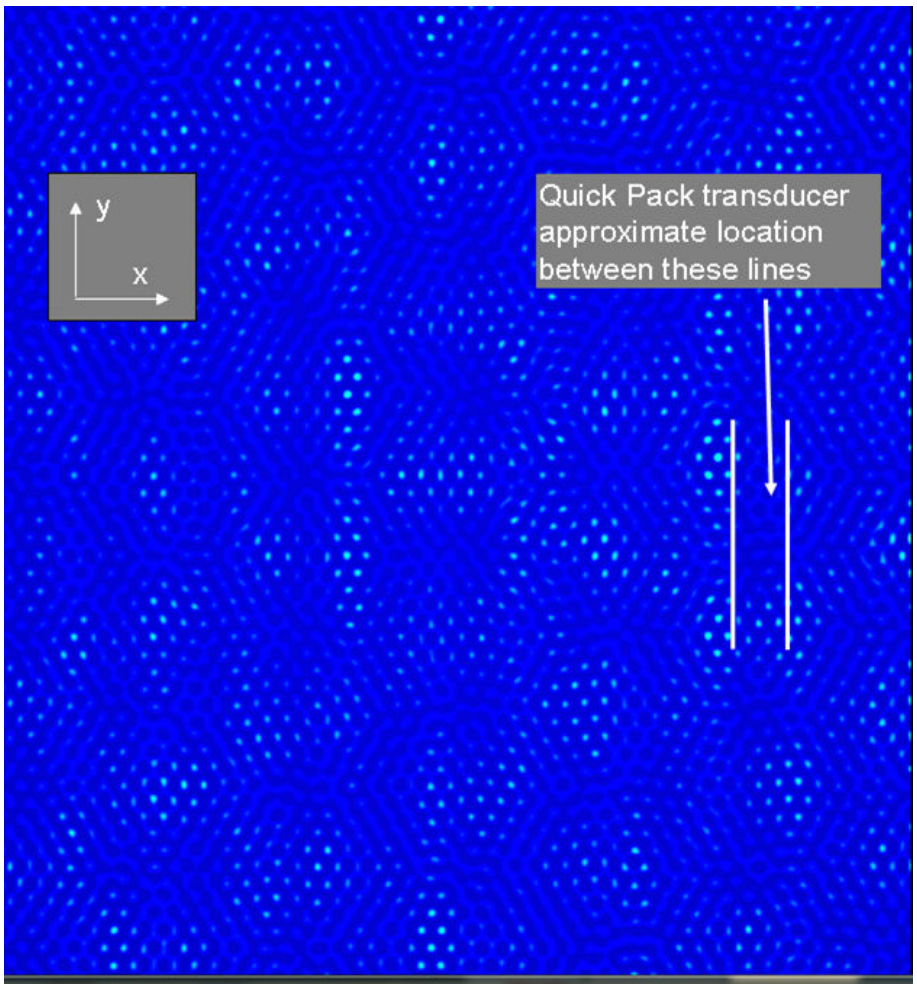

Figure 8.21. Snapshots of simulated out-of-plane displacement. Vibration is continuously transmitted by a Quick Pack QP10n transducer model. Snapshots taken 20 ms into simulation.

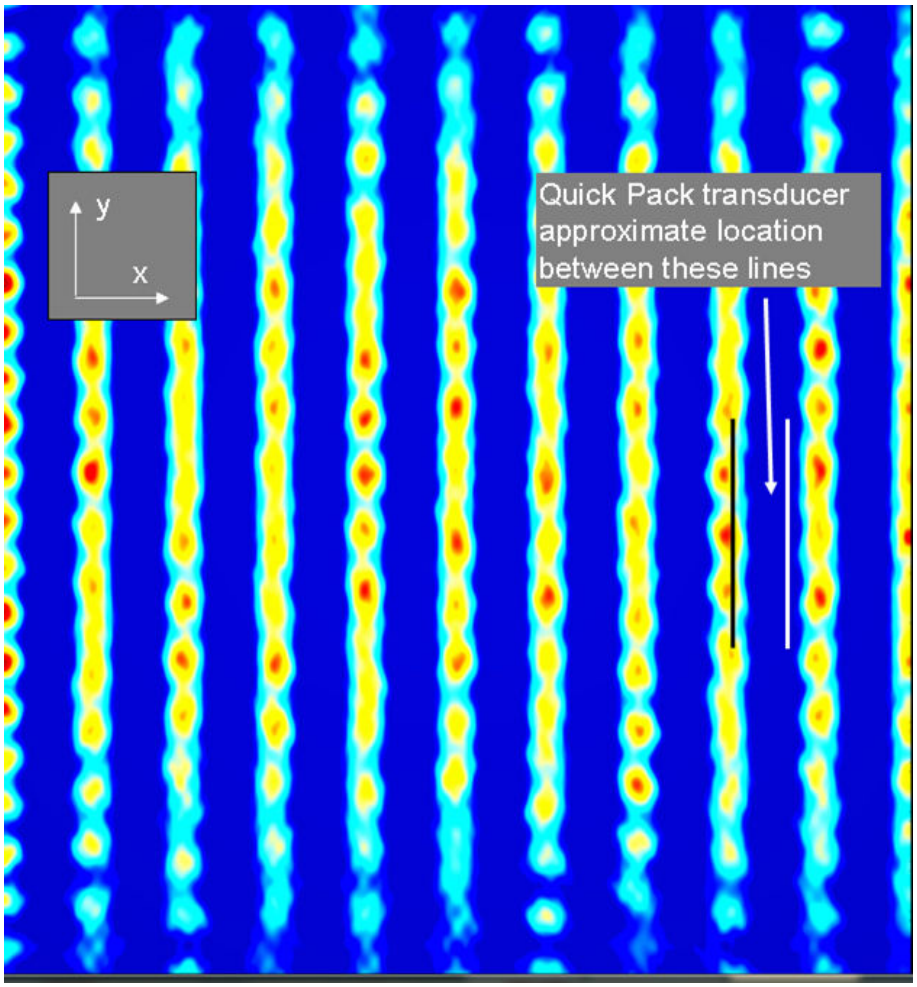

Figure 8.22. Snapshots of simulated in-plane x-axis component displacement. Vibration is continuously transmitted by a Quick Pack QP10n transducer model. Snapshots taken 20 ms into simulation.

8.5. Summary and discussion

The LISA software computer simulations of Lamb wave propagation presented in this chapter show the usefulness and accuracy of this simulation method. The results also confirm the correctness of the adopted patch transducer modelling method, in which the transducer is represented only by its oscillating edges.

Simulations of cases in which the transducers were driven by five-cycle pulses returned correct propagation velocities, wavelengths and proportions between the in-plane and out-of-plane displacement amplitudes. Simulated time domain waveforms closely matched the waveforms recorded with a laser vibrometer. Maps of vibration recorded in a single time instant over the area of a simulated plate displayed plausible propagation patterns, including reflections from plate edges.

Simulations of continuous signal transmission returned incorrect time domain waveform shapes due to the effects of numerical dispersion and the lack of energy loss modelling. Nevertheless, the wavelengths measured on plate snapshots were correct and the patterns were plausible. Work is being carried out by the software development team on the correction of the numerical dispersion error. A solver modelling energy loss already exists, although its use results in an approximately eight-fold increase in the duration of calculation (Paćko 2013). In the case of entire-plate simulations reported here, this would mean an increase from approximately two hours to sixteen hours for each case. Furthermore, the solver was not available to the author at the time the simulation work was being performed.

Further development of simulation data analysis tools is likely to significantly increase the usefulness of the software in the development of the ultrasonic Lamb wave energy transmission system. Tools which the author would find useful include:

- A tool generating a map of maximum amplitudes of vibration over the area of the simulated plate. This tool will allow a direct comparison with FFT images recorded with a laser vibrometer to be made.
- A tool calculating the average in-plane strain amplitude over the area of a reception transducer. This tool will allow the application of the reception transducer modelling method, as described in Chapter 6.

Suggestions for further development were passed to the software development team.

8.6. Conclusion

This chapter concludes the investigation of the prototype Lamb wave energy transmission system carried out during the project reported in this thesis. In the following chapter all results obtained during the project are summarised and their significance is discussed.

Chapter 9. Conclusion and discussion

9.1. Summary of findings and discussion

9.1.1. Assessment of achievable performance

An experimental example of an ultrasonic energy transmission system was built. The setup utilised a 1.5 mm-thick aluminium plate to model a fragment of aircraft skin with structural elements, such as stringers, omitted for simplicity as required at the initial development stage. Pairs of three commercially available transducers types were bonded to the plate in order to act as transmitters and receivers of ultrasonic Lamb waves. The distance between transducers in each pair was 54 cm. Electric circuits required to optimise the power transfer to and from the transducers as well as to measure the input and output electrical power were also built. The setup was extensively used throughout the project. Multiple configurations of transducers, electric circuit elements and operating parameters were tested and compared.

Two configurations using Quick Pack QP10n and MFC M8528-P1 transducers were identified as the best performing. It was found that using inductors placed in series with transducer in order to compensate for the capacitive characteristics of the latter was a step necessary to achieve a maximum power throughput. The Quick Pack setup utilised 0.69 mH compensating inductors and transmitted 12.7 mW of power with 11.2 % efficiency, while being driven by a 20 Vpp, 35 kHz sinusoidal AC signal. The MFC setup utilised 0.1 mH compensating inductors and transmitted 17 mW of power with 64 % efficiency, while being driven by a 20 Vpp, 224 kHz sinusoidal AC signal. A third transducer type, McWade NS3303 150 kHz was also tested. A pair of these transducers was found to transmit only 0.001 mW with 0.0007 % and was not considered for further investigation.

The power supplied to the experimental system was limited by the maximum voltage and power output of the laboratory signal generator used. Both transducer types can be safely driven with voltages of up to 1200 V. Therefore the use of a more capable power supply is an easy route to significantly increasing the power throughput, which increases with the square of the drive voltage.

The demonstrated energy transmission distance was 54 cm in a plate 82 cm wide and 100 cm long. Mapping of the vibration amplitudes in the plate, performed using a laser vibrometer, showed that there was no visible decrease of these amplitudes

along the entire length of the plate. This indicates that the transmission distance can be significantly increased without a considerable decrease of the power throughput.

9.1.2. Frequency characteristics of the system

The energy transmission system was tested in the range of frequencies from 20 kHz to 230 kHz. The McWade transducers were found to exhibit a sharp resonance at 117 kHz. This was reflected in the behaviour of the energy transmission setup using these transducers, which transmitted measurable amounts of power only within approximately ± 1 kHz of the 115 kHz optimum frequency. (The minor frequency difference may have been caused by impedances of other circuit components as well as a measurement error).

The Quick Pack-based system achieved optimum performance of 12.7 mW with a 0.69 mH inductor. The optimum operating frequency decreased to 35 kHz. A second power transmission peak occurred with a 0.1 mH inductor at 65 kHz. A significant disadvantage of the compensating inductance use was the narrowing of the power transmission peak frequency ranges. The power throughput peaks were less than 1 kHz wide, resulting in a need for a precise tuning in order to operate within one of these peaks.

The MFC-based system achieved optimum performance of 17 mW with a 0.1 mH inductor at 224 kHz. A further increase of the compensating inductance up to 0.22 mH caused a slow power throughput decrease down to 13.6 mW and an optimum operating frequency decrease to 152 kHz. This indicated that with the MFC transducer the inductive compensation can be used to adjust the operating frequency without a significant loss of performance. Such a characteristic can be useful to account for other design considerations in a practical system. The maximum power transmission peaks observed with inductive compensation were also relatively wide. At 0.1 mH a 50 % decrease of the power throughput occurred 20 kHz away from the optimum frequency. This indicates an ease of tuning even with the use of inductive compensation.

9.1.3. Characterisation and comparison of commercially available transducers

Three commercially available types of piezoelectric transducers were characterised and compared: the McWade NS3303 150 kHz, the Mide Technology Corporation Quick Pack QP10n, and the Smart Material Corporation MFC 8528-P1.

The electrical impedance-frequency characteristics of the transducers were measured. These characteristics were not available from any of the manufacturers. Therefore the measurement significantly increased the knowledge of the transducers' performance. The measured impedance characteristics were used to model the transducers in a MATLAB circuit simulation tool. The results of the transmission circuit simulations matched the measurements with good accuracy. The influence of the inductive compensation was also accurately modelled.

It was found that the frequency at which the optimum electrical performance of a transducer is achieved typically is not the same as the frequency at which the efficiency of Lamb wave generation is the best (i.e. the dimensions of the transducer are correctly matched to the Lamb wave wavelength). The optimum performance frequencies identified during the project should be regarded as those at which the best compromise between the electrical and the acoustical efficiency is achieved.

9.1.4. Lamb wave propagation

A scanning laser vibrometer was used to measure the Lamb wave-related vibration in the experimental aluminium plate.

The transmission characteristics of the two selected transducer types were measured. The MFC M8528-P1 transducer operating in its optimum frequency range of 150 – 190 kHz was found to transmit a narrow beam of a Lamb wave signal along its longitudinal axis. At 180 kHz the out-of-plane amplitude of the wave was 0.45 nm and corresponded to the A_0 mode. The S_0 mode was transmitted with an out-of-plane amplitude of 0.06 nm.

The Quick Pack QP10n transducer operating in its optimum frequency range of 55 – 75 kHz was found to transmit along both the longitudinal and the transverse axes. At 65 kHz the A_0 mode the Lamb wave transmitted in the longitudinal direction had an out-of-plane amplitude of 4.4 nm and the wave transmitted the transverse direction had an amplitude of 11.8 nm. The S_0 signal was transmitted omnidirectionally with an amplitude of approximately 0.8 nm.

The propagation of a continuously transmitted Lamb wave signal in the aluminium test plate was also imaged. A partial standing wave pattern was found to appear in the plate. The wave pattern differed depending on the transducer type. It was also shown to change significantly with the change of transducer position and orientation as well as with the plate geometry. In some geometries a destructive

interference of direct and reflected waves occurred, resulting in a disappearance of vibration at the reception transducer location. These phenomena pose a significant difficulty in the practical application of the investigated ultrasonic energy transmission system. At the same time, the appearance of the standing wave was beneficial to the power transmission capacity. The standing wave amplitude (in areas of constructive interference) was two to three times higher than the amplitude of the Lamb wave signal transmitted by the transducer. This significantly increased the amount of power that was available to the receiving transducer. In practical applications a reduction of the standing wave effect can be expected. This will be due to the leakage of vibration further into the aircraft structure.

The Lamb wave propagation was also simulated using the LISA finite difference method software. A limited number of cases were investigated, however the results matched experiment very well, which shows the potential of the simulation method in further work.

9.2. Comparison to previously published results

Previously published work on ultrasonic energy transmission was summarised in Table 2.2 on page 19.

In comparison to these, the author achieved a significant increase of the transmission distance. The longest previously reported transmission distance was 15 cm (Shoudy 2007). In this work, a distance of 54 cm was demonstrated, with results indicating a potential to increase this distance without significant power throughput loss.

The power transmission efficiency achieved in this work was on par with previously reported results. Efficiencies reported in literature were in the range between 34 % (Moss 2010) and 88 % (Bao 2008). The highest result achieved by the author was 64 %.

The power throughput is directly related to the drive voltage used and therefore comparing published results with those achieved by the author is of little value, as both can be readily increased by using a higher voltage drive signal.

A significant qualitative difference was also achieved during the reported project. All previously reported cases of ultrasonic energy transmission used acoustic bulk waves and transmitted through the thickness of a material. The system reported here used guided plate waves (Lamb waves) and transmits along the surface of a plate.

Another unique result was the imaging of continuously transmitted Lamb waves and of the formation of various forms of standing waves in a relatively large plate, carried out with the use of a scanning laser vibrometer. While straightforward technically and conceptually, results of such work were not published by others. Once carried out, however, the scans revealed a wealth of information regarding the propagation, reflection and interference of Lamb waves in a practical engineering application.

9.3. Conclusion

In this thesis the development and testing of a prototype metre-range ultrasonic Lamb wave-based energy transmission system was described. To the author's knowledge, this is the first time such a system was investigated. While a number of ultrasonic energy transmission systems have been reported in previously published literature, none of these systems utilised guided plate waves and achieved a transmission distance greater than 15 centimetres.

The system described in this work was designed specifically to transmit energy in aviation structures over distances of the order of metres. The design takes advantage of the fact that most aviation structures are built from plates and can therefore serve as guides for acoustic guided plate waves, also referred to as Lamb waves. This type of acoustic wave is characterised by particularly low energy losses, allowing the achievement of a significant extension of the energy transmission distance.

An optimised laboratory system transmitted 17 mW of power with 64% efficiency across a distance of 54 cm while being driven by a 20 V peak-to-peak, 224 kHz AC signal (see Table 5.6 on page 81). This power throughput figure can be easily increased by using a higher drive voltage, as the electric power increases with the square of the drive voltage and the maximum safe operating voltage of the transducers used is 1200 V.

The demonstrated energy transmission distance of 54 cm is over three times larger than in systems previously reported in literature. The power transmission efficiency is on par with the best of those systems. Furthermore, no Lamb wave amplitude loss across the investigated transmission distance was detected. This suggests that larger transmission distances are possible.

The demonstrated performance shows that the method is capable of supplying sufficient power to wireless acoustic emission SHM sensor nodes which currently

have a maximum power requirement of approximately 200 mW. It is also able to transmit energy across distances encountered in aviation structures. Thus, the requirement set forth in the project specification has been met.

9.4. Further work

The following directions of further work were identified during course of the project:

Measurement of the in-plane vibration of the plate using a 3D laser vibrometer setup
The patch transducers, identified as an optimum choice for the energy transmission application, couple to the in-plane strain field of the Lamb wave. The characterisation of this field using a 3D vibrometer will allow the operation of the transmission and reception transducers to be quantitatively characterised. Furthermore, using the in-plane data the reception transducer modelling code developed in this project can be fully utilised to identify optimum locations for reception transducer. This ability will be highly beneficial when the energy transmission system application on more complex structures is investigated.

Improvement of the LISA simulation model

Further work is required on the LISA software-based simulation techniques. The limited number of simulations performed during the project indicated the benefits of the use of this software. Directions of further development should include:

- Development of more accurate transmission transducer models
- Development of a routine calculating the amplitudes of the standing wave pattern
- Development or a routine calculating the average in-plane strain amplitude at the location of the receiving transducer, similarly to the method developed for the use with laser vibrometer data
- Further validation of simulation results against out-of-plane and in-plane laser vibrometer data

Development of a complete simulation model of the system

A complete simulation model of the energy transmission system will be highly beneficial in the further development work, especially for practical applications. During this project tools for the simulation of the electric circuits, the reception transducer (in a limited capacity) and the Lamb wave generation and propagation

were developed. Still required are the development of a complete transducer model and the integration of all simulation components into a complete working model.

Investigation of adaptive frequency tuning

Based on the findings of this project it is expected that an adaptive frequency tuning method may be able to compensate for the geometric and environmental variation encountered in practical applications. The experimental and simulation techniques listed above will be essential in the development of such a tuning method as they will allow the designer to efficiently map the Lamb wave propagation at multiple frequencies and thus assess the impact of frequency tuning.

Transducer optimisation

Off-the-shelf transducer types were used in the project. It was found that the optimum electrical and acoustical efficiencies of such transducers do not occur at the same frequencies. It is therefore worthwhile to investigate transducer designs which could allow both these efficiencies to maximised at one frequency.

Interference with damage detection

The ultrasonic energy transmission signal may interfere with the acoustic damage detection operation of the SHM system. This interference and ways to mitigate it require investigation.

Development and testing of the system on real structural components

The Lamb wave ultrasonic energy transmission system has so far been investigated on a significantly simplified structure model. Bringing the system towards practical application requires design and testing on samples of real aviation structures. This work may have to include the development of a method allowing the ultrasonic signal to bypass aircraft structural elements located under skin panels, to which vibration energy is likely to leak.

Development of dedicated drive and reception electronics

The application of the system in practice will require dedicated electronics, compliant with aviation regulations, to be developed.

Investigation of interference with other aircraft systems

The compatibility with other aircraft systems will have to be assessed if the application of the system is to proceed. In particular, the interference with ultrasonic damage detection systems should be investigated.

Investigation of environmental effects of the system operation

The influence of prolonged exposure to sound of the frequency used in the system (regardless of it being above the audible range) on humans should be investigated. Furthermore, the influence on animals, especially those which can hear above 20 kHz, may need to be investigated, as possible negative effects may concern both animals transported on the aircraft and those living in the vicinity of the airport. Another area of concern requiring investigation would be interference with the operation of hearing aids.

References

[1] Advanced Cerametrics website, *Harvestor Power Module*, http://www.advancedcerametrics.com/pages/harvestor_power_module [retrieved 18/02/2013]

[2] Agilent. (2004). *Agilent Network Analyzer Basics*. Agilent

[3] Agilent. (2009). *Agilent Impedance Measurement Handbook*. *Measurement*. Agilent

[4] Arnold, M. *et al.*, 2012. Energy Management Systems for Energy Harvesting in Structural Health Monitoring Applications. *Key Engineering Materials*, 518, pp.137–153.

[5] Avdelidis, N.P., Hawtin, B.C. & Almond, D.P., 2003. Transient thermography in the assessment of defects of aircraft composites. *NDT & E International*, 36(6), pp.433–439.

[6] Bao, X. *et al.*, 2008. High-power piezoelectric acoustic-electric power feedthru for metal walls. In *Proceedings of SPIE*. SPIE, p. 69300Z–69300Z–8.

[7] Bitar, N. and Gunnarsson, L. 2010. Assembly Analysis – Fixed Leading Edge for Airbus A320. Thesis, Linkopings Universitet.

[8] Boeing Commercial Airplanes, 2001. Statistical Summary of Commercial Jet Airplane Accidents

[9] Boeing Commercial Airplanes, 2006. Statistical Summary of Commercial Jet Airplane Accidents

[10] Boeing Commercial Airplanes, 2011. Statistical Summary of Commercial Jet Airplane Accidents

[11] Bogue, R., 2010. The role of robotics in non-destructive testing. *Industrial Robot: An International Journal*, 37(5), pp.421–426.

[12] Carazo, A.V., 2004. 50 Years of Piezoelectric Transformers. Trends In The Technology. In *Proc. Mater. Res. Soc. Symp.* vol. 785, pp.D1.7.1 –D1.7.12 2004.

[13] Cawley, P. 1990. Low frequency NDT techniques for the detection of disbonds and delaminations. *British Journal of Non-Destructive Testing* 32(9), pp. 454–461.

[14] Cawley, P., 2001. Non-destructive testing--current capabilities and future directions. *Proceedings of the Institution of Mechanical Engineers, Part L: Journal of Materials Design and Applications*, 215(4), pp.213–223.

[15] Chetwynd, D. *et al.*, 2008. The Effects of Uncertainties within Acoustic Emission Modelling. In *Conference: 2008 IMAC-XXVI: Conference & Exposition on Structural Dynamics*.

[16] Crawley, E., and Anderson, E., 1990, "Detailed models of piezoceramic actuation of beams." *Journal of Intelligent Material Systems and Structures* 1.1: 4-25.

[17] Dalton, R.P., 2000. *The Propagation of Lamb Waves Through Metallic Aircraft Fuselage Structure*. Imperial College London.

[18] Denisov, A. & Yeatman, E., 2010. Ultrasonic vs. Inductive Power Delivery for Miniature Biomedical Implants. *2010 International Conference on Body Sensor Networks*, pp.84–89.

[19] Di Scalea, F.L., Matt, H. & Bartoli, I., 2007. The response of rectangular piezoelectric sensors to Rayleigh and Lamb ultrasonic waves. *The Journal of the Acoustical Society of America*, 121(1), p.175.

[20] Disperse software web site, n.d., http://www3.imperial.ac.uk/nde/products%20and%20services/disperse, [accessed 2013-03-08]

[21] Dover, W.D., Collins, R. and Michael, D.H. 1991. Review of developments in ACPD and ACFM. *British Journal of Non-Destructive Testing* 33(3), pp. 121–127.

[22] Eaton, M.J., Pullin, R. and Holford, K.M. 2012. Towards improved damage location using acoustic emission. *Proceedings of the Institution of Mechanical Engineers, Part C: Journal of Mechanical Engineering Science* 226(9), pp. 2141–2153.

[23] EVG, n.d., SAW Devices, *EVG Website,* http://www.evgroup.com/en/solutions/saw_devices/introduction, retrieved 2013-06-26

[24] Ferro Solutions, *Products,* http://ferrosi.com/products.htm, [retrieved 18/02/2013]

[25] Finlayson, R.D., Friesel, M., Carlos, M., Cole, P. and Lenain, J.C. 2001. Health monitoring of aerospace structures with acoustic emission and acousto-ultrasonics. *Insight, Non-Destructive Testing and Condition Monitoring* 43(3), pp. 1–4.

[26] Giurgiutiu, V. & Bao, J., 2004. Embedded-ultrasonics Structural Radar for In Situ Structural Health Monitoring of Thin-wall Structures. *Structural Health Monitoring*, 3(2), pp.121–140.

[27] Giurgiutiu, V., 2005. Tuned Lamb Wave Excitation and Detection with Piezoelectric Wafer Active Sensors for Structural Health Monitoring. *Journal of Intelligent Material Systems and Structures*, 16(4), pp.291–305.

[28] Giurgiutiu, V., 2005. Tuned Lamb Wave Excitation and Detection with Piezoelectric Wafer Active Sensors for Structural Health Monitoring. *Journal of Intelligent Material Systems and Structures*, 16(4), pp.291–305.

[29] Goranson, U.G., 2007. Damage Tolerance Facts and Fiction. *Keynote presentation, International Conference on Damage Tolerance of Aircraft Structures, Delft, 2007*

[30] Graham, D.J., Neasham, J.A. & Sharif, B.S., 2011. Investigation of Methods for Data Communication and Power Delivery Through Metals. *Industrial Electronics, IEEE Transactions on*, 58(99), pp.1–1.

[31] Greaves, B.J. 2008. A feasibility study into piezoelectric power harvesting of vibrations in aircraft to power structural health monitoring systems. Cardiff University.

[32] Greaves, B.J., 2008. *A feasibility study into piezoelectric power harvesting of vibrations in aircraft to power structural health monitoring systems*. Cardiff University.

[33] Grigg, S. and Paget, C. (Airbus) 2013. Private correspondence.

[34] Grondel, S. *et al.*, 2002. Design of optimal configuration for generating A[sub 0] Lamb mode in a composite plate using piezoceramic transducers. *The Journal of the Acoustical Society of America*, 112(1), p.84.

[35] Haig, A., 2010. MFC Presentation. SHeMS Project Meeting Jul 2010.

[36] Hexcel – HexTow® Continuous Carbon Fiber Products, http://www.hexcel.com/Resources/Cont-Carbon-Fiber-Data-Sheets, accessed 2013-05-24

[37] Hoskins, P.R. 2012. Principles of ultrasound elastography. *Ultrasound* 20 (1), pp. 8–15.

[38] Hung, Y.Y., 1982 "Shearography: A new optical method for strain measurement and nondestructive testing". *Optical Engineering 21* (May/June 1982), pp.391–395

[39] Kahandawa, G.C. *et al.*, 2012. Use of FBG sensors for SHM in aerospace structures. *Photonic Sensors*, 2(3), pp.203–214.

[40] Kim, E. 2001. *From Reflection Coefficient to Load Impedance (Smith Chart)*. University of San Diego. Retrieved from http://home.sandiego.edu/~ekim/e194rfs01/lec08ek.pdf

[41] Kim, H. *et al.*, 2007. Consideration of impedance matching techniques for efficient piezoelectric energy harvesting. *IEEE transactions on ultrasonics, ferroelectrics, and frequency control*, 54(9), pp.1851–9.

[42] Kim, H., Priya, S., Stephanou, H. and Uchino, K. 2007. Consideration of impedance matching techniques for efficient piezoelectric energy harvesting. *IEEE transactions on ultrasonics, ferroelectrics, and frequency control* 54(9), pp. 1851–9.

[43] Kinsley-Jones, M., 2012. The Qantas A380 drama - QF32 a year on. *Flightglobal.com Aviation Business blog,* http://www.flightglobal.com/blogs/airline-business/2011/11/qf32---a-year-onthis.html [accessed 2013-02-19]

[44] Kluge, M. *et al.*, 2008. Remote acoustic powering and data transmission for sensors inside of conductive envelopes. *2008 IEEE Sensors*.

[45] Krautkramer, J., 1983. *Ultrasonic Testing of Materials* 3rd ed., Springer-Verlag.

[46] Kuphaldt, T.R., 2007. *Lessons in Electric Circuits - Volume II - AC*, Retrieved from http://www.openbookproject.net/electricCircuits/AC/ [retrieved on 2013-04-15]

[47] Lamb, H., 1917, "On waves in an elastic plate", in *Conference of the Royal Society , London*, vol. XCIII, pp. 114-128

[48] Larson, P. & Towe, B., 2011. Miniature ultrasonically powered wireless nerve cuff stimulator. *Neural Engineering (NER), 2011 5th*, pp.265–268.

[49] Lawry, T.J. *et al.*, 2010. Electrical optimization of power delivery through thick steel barriers using piezoelectric transducers. In *SPIE Defense, Security, and Sensing*. pp. 768314–768314–12.

[50] Lawry, T.J., Wilt, K.R., Roa-Prada, S., Ashdown, J.D., Saulnier, G.J., Scarton, H.A., Das, P.K. and Pinezich, J.D. 2010. Electrical optimization of power delivery through thick steel barriers using piezoelectric transducers. In: *SPIE Defense, Security, and Sensing*. pp. 768314–768314–12.

[51] Lin, C., 1997. *Design and Analysis of Piezoelectric Transformer Converters*.

[52] Lin, R.-L., 2001. *Piezoelectric Transformer Characterization and Application of Electronic Ballast*. Virgfinia Polytechnic Institute.

[53] Løkberg, O.J. and Malmo, J.T. 1988. Detection of defects in composite materials by TV holography. *NDT International* 21(4), pp. 223–228.

[54] Luangvilai, K., 2007. *Attenuation of Ultrasonic Lamb Waves with Applications to Material Characterization and Condition Monitoring*. PhD thesis at Georgia Institute of Technology

[55] Maleki, T. *et al.*, 2011. An ultrasonically powered implantable micro-oxygen generator (IMOG). *IEEE transactions on bio-medical engineering*, 58(11), pp.3104–11.

[56] McWade, n.d, *Acoustic Emission Solutions,* http://www.mcwademonitoring.co.uk/acoustic-emissions-solutions.php, [retrieved 2013-03-22]

[57] Microstrain, 2013, http://www.microstrain.com/applications/aerospace, retrieved 04/02/2013

[58] Mide, n.d., *Quick Pack Piezoelectric Transducers Online Catalog,* http://www.mide.com/products/qp/qp_catalog.php#sensor, [retrieved 2013-03-22]

[59] Mide, *Vibration Energy Harvesting Products - Online catalog,* http://www.mide.com/products/volture/volture_catalog.php, [retrieved 18/02/2013]

[60] Mineo, C., Herbert, D. & Morozov, M., 2012. Robotic Non-Destructive Inspection. *British Institute of Nondestructive Testing, http://www.bindt.org/downloads/NDT2012_4C2.pdf*

[61] Moss, S. *et al.*, 2010. Detachable acoustic electric feedthrough. In *Proceedings of SPIE*. pp. 764745–764745–12.

[62] Neasham, J., 2010. Wireless data and power transfer through metals. *Newcastle University Extreme Technologies Programme publication*.

[63] Ngo, L, Kluge, M, Sabater, J, Schalk, J, Seidel, H & Schmid, U 2008, 'Long-Term Performance of Ultrasonic Transducers Used for Energy and Data Transmission', in *Integration Issues of Miniaturized Systems-MOMS, MOEMS, ICS and Electronic Components (SSI), 2008 2nd European Conference & Exhibition on*, VDE, Barcelona, pp. 1–6.

[64] Paćko, P. 2013. Private discussion with a LISA software development team member.

[65] Paget C. (Airbus), 2010. Private correspondence with the project sponsor.

[66] Paget C. (Airbus), 2011. Private correspondence with the project sponsor.

[67] Perpetuum, *Products,* http://www.perpetuum.com/products.asp [retrieved 18/02/2013]

[68] Pfeiffer, H. & Wevers, M., 2007. Aircraft Integrated Structural Health Assessment – Structural Health Monitoring and its implementation within the European project AISHA. In *EU Project Meeting on Aircraft Integrated Structural Health Assessment (AISHA), Leuven, Belgium, June 2007*. pp. 1–9.

[69] Pretorius, J., Hugo, M. & Spangler, R., 2004. A Comparison of Packaged Piezoactuators for Industrial Applications substrate piezo substrate. *Mide Technology Corporation Publication*, pp.1–12.

[70] Rayleigh, Lord 1885. On Waves Propagated along the Plane Surface of an Elastic Solid. *Proceedings of the London Mathematical Society* s1-17 (1), pp. 4–11. Available at: http://plms.oxfordjournals.org/content/s1-17/1/4.short.

[71] Rosen, C.A., Fish, K.A. and Rothenberg, H.C. 1958. Electromechanical Transducer. US Patent 2830274.

[72] Roundy, S., Wright, P.K. & Pister, K.S.J., 2002. Micro-electrostatic vibration-to-electricity converters. , pp.1–10.

[73] Roundy, S., Wright, P.K. and Rabaey, J. 2003. A study of low level vibrations as a power source for wireless sensor nodes. *Computer Communications* 26(11), pp. 1131–1144.

[74] Rowe, D.M. & Min, G., 1998. Evaluation of thermoelectric modules for power generation. *Journal of Power Sources*, (November 1997).

[75] Samson, D. *et al.*, 2011. Wireless sensor node powered by aircraft specific thermoelectric energy harvesting. *Sensors and Actuators A: Physical*, 172(1), pp.240–244.

[76] Shang, J. *et al.*, 2007. Design of a climbing robot for inspecting aircraft wings and fuselage. *Industrial Robot: An International Journal*, 34(6), pp.495–502.

[77] SHeMS, 2012. Private communication with members of the SHeMS (Lightweight Structural Health Monitoring System) team, *Cardiff University*

[78] Shoudy, D.A. *et al.*, 2007. An Ultrasonic Through-Wall Communication System with Power Harvesting. *2007 IEEE Ultrasonics Symposium Proceedings*, pp.1848–1853.

[79] Sinocera, Product website. http://www.sinocera.net/en/piezo_material.asp Retrieved 2013-12-28

[80] Smart Material, n.d., *MFC*, http://www.smart-material.com/MFC-product-main.html, [retrieved 2013-03-22]

[81] Sodano, H.A., 2003. *Macro-Fiber Composites for Sensing , Actuation and Power Generation*. Virgina Polytechnic Institute.

[82] Speckmann, H. & Roesner, H., 2006. Structural Health Monitoring : A Contribution to the Intelligent Aircraft Structure. In *Proceedings ECNDT 2006*. pp. 1–7.

[83] Speckmann, H., 2007. Structural Health Monitoring (SHM). In *EASA IMRBPB Meeting Cologne, April 22, 2007*.

[84] Toh, M., 2012. Qantas grounds A380 after finding 36 cracks on wings. *Flightglobal.com*, http://www.flightglobal.com/news/articles/qantas-grounds-a380-after-finding-36-cracks-on-wings-367923/ [accessed 2013-02-19]

[85] USGS, n.d., Earthquake Glossary - Rayleigh wave, *USGS Website,* http://earthquake.usgs.gov/learn/glossary/?term=Rayleigh%20wave, retrieved 2013-06-26

[86] Viktorov, I.A., 1967. *Raleigh and Lamb Waves: Physical Theory and Applications* Plenum Press,

[87] Wanhill, R.J.H., 2002. Milestone Case Histories in Aircraft Structural integrity. In *Milne, I.; Ritchie, R.O.; Karihaloo, B. (2003). Comprehensive Structural Integrity, Volumes 1-10.. Elsevier.*

[88] WITNESSS project website, TSB (Technology Strategy Board), n.d., https://connect.innovateuk.org/web/witnesss, accessed 2013-06-26